Comet Hitchhiker

NIAC Phase I Final Report

June 30, 2015

Masahiro Ono, Marco Quadrelli, Gregory Lantoine, Paul Backes,
Alejandro Lopez Ortega, Håvard Grip, Chen-Wan Yen

Jet Propulsion Laboratory, California Institute of Technology

David Jewitt

University of California, Los Angeles

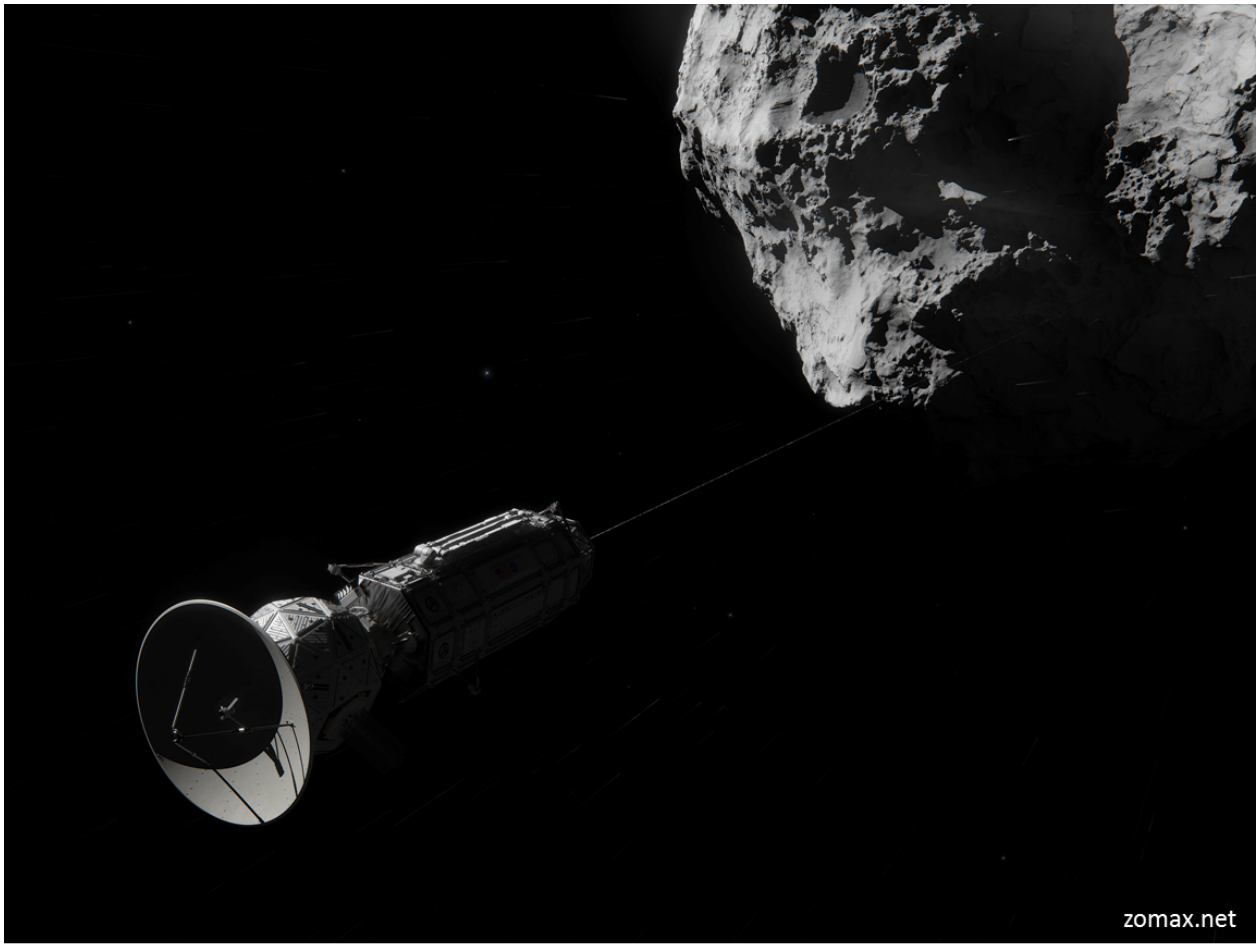

This research was carried out in part at the Jet Propulsion Laboratory, California Institute of Technology, under a contract with the National Aeronautics and Space Administration, and in part at University of California, Los Angeles.

Preface

Yes, of course *the Hitchhiker's Guide to the Galaxy* was in my mind when I came up with a concept of a tethered spacecraft hitching rides on small bodies, which I named *Comet Hitchhiker*. Well, this NASA-funded study is not exactly about traveling through the Galaxy; it is rather about exploring our own Solar System, which may sound a bit less exciting than visiting extraterrestrial civilizations, building a hyperspace bypass, or dining in the Restaurant at the End of the Universe. However, for the "primitive ape-descended life forms that have just begun exploring the universe merely a half century or so ago, our Solar System is still full of intellectually inspiring mysteries.

So far the majority of manned and unmanned Solar System travelers solely depend on a fire breathing device called rocket, which is known to have terrible fuel efficiency. You might think there is no way other than using the gas-guzzler to accelerate or decelerate in an empty vacuum space. However, if you stop and look around, you would notice that the Solar System is actually like a heavily-trafficked intersection; more than 670,000 asteroids and 3,800 comets have been discovered thus far in variety of orbits; in the outer rim of the Solar System, it is estimated that about 100,000 Kuiper belt objects (KBOs) exist with diameters of 100 kilometers or larger. Then wouldn't it be a good idea to hitch a ride on one of those vehicles instead of driving on your own?

If you are a hitchhiker, you must know that arriving at a destination is just a fraction of the reason why you hitchhike. The best part of a hitchhiking trip is the conversations with drivers. They would tell you a local's favorite restaurant that is not on your tourist book; they would sing a song or read a poem for you; they would tell you all the stories from local industry and history to a scandalous love affair between two young villagers. By when you say "thank you" and get off the car, you would be more familiar with the locals than any other tourists. It is the same in Solar System hitchhiking. Small bodies are too scientifically interesting to be used just as vehicles. They are like old villagers, who preserve the story of the origin and evolution of the Solar System for 4.6 billion years. The story is so extensive that you need to spend years with him to hear all of it. That is why a Comet Hitchhiker wants to get a hitch, instead of just flying by.

As expected, hitchhiking a celestial body is not as simple as sticking out your thumb or knowing where your towel is, because it flies at an astronomical speed and it won't stop to pick you up. Instead of a thumb, our idea is to use a harpoon and a tether. First, you harpoon a target as you make a close fly-by and attach a tether. Then, as the target moves away, you reel out the tether while applying regenerative braking to accelerate yourself. Once your velocity is matched to that of the target, you are ready to jump on it! But you might wonder if it is really possible to build such a spacecraft. Can a harpoon tolerate a hypervelocity impact? Can we engineer a tether strong enough to support the highly dynamic maneuver? Those are exactly the questions our team studied for a year using supercomputer simulations and finite element analyses.

At the conclusion of this study, we were unfortunately unable to provide an answer to the Ultimate Question of Life, the Universe, and Everything. However, our study did provide in-depth understanding of the utility and feasibility of the innovative concept of Solar System hitchhiking, which is presented in this report. I believe hitchhikers will one day enable us to go to the remotest corners of the Solar System to hear the stories of the old men, which will make the ape-descended spices a little bit wiser.

I would like to thank all the talented and knowledgeable scientists and engineers on the team. I would also like to deeply appreciate the NASA Innovative Advanced Concept Program for providing generous funding to such a seemingly crazy idea and making this study happen.

Masahiro Ono
Principal Investigator

Summary of Activities

- Developed the Comet Hitchhiker concept, which is to hitch rides on small bodies (asteroids and comets) using a tethered spacecraft. (Section 2)
- Identified five scientifically important missions that would be enabled or significantly benefited by the Comet Hitchhiker concept. The five mission concepts are: KBO rendezvous, Centaur rendezvous, Trojan rendezvous, Damocloid rendezvous, and Main asteroid belt tour to rendezvous with multiple ($\sim$10) objects. (Section 3)
- Derived the *Space Hitchhike Equation*, or "the rocket equation for hitchhiker", which relates the specific strength of tether, mass ratio, and ΔV. (Section 4.1)
- Performed in-depth feasibility analysis of the critical components of the concept through:
  - Finite-element simulations of tether and spacecraft dynamics, as shown in Figure 1 (Section 4.4)
  - Supercomputer simulations of the hypervelocity impact of harpoon on a small body, as shown in Figure 2. (Section 6)
- Performed public outreach activities including the collaboration with a concept artist of the Museum of Science Fiction, exposure to media, and public presentations. (Section 8)

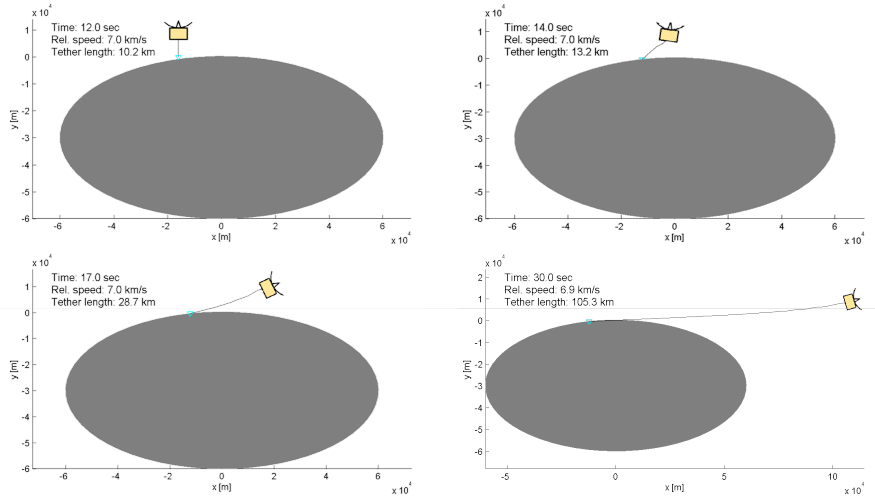

Figure 1: Finite-element simulation of tether and spacecraft dynamics. The size of spacecraft is exaggerated for visualization purposes.

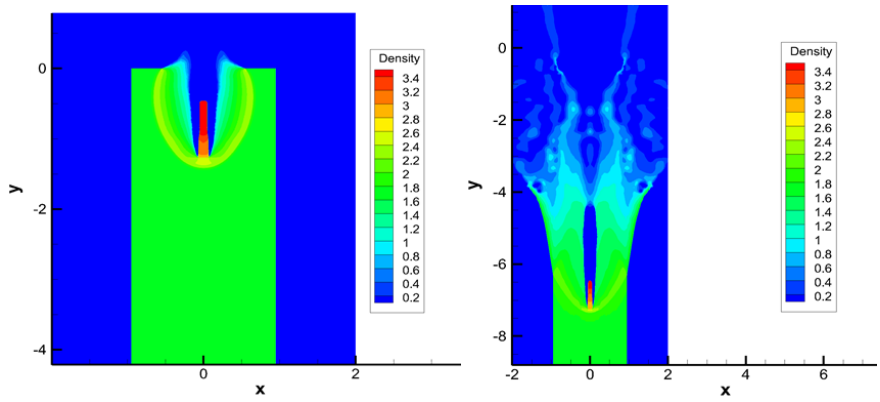

Figure 2: Supercomputer simulation of the hypervelocity impact of a harpoon on a small body.

Summary of Findings

- **Rendezvous/landing missions to small bodies in the outer Solar System** is essential to achieve a NASA's strategic goals to "ascertain the content, origin and evolution of the Solar System." (Sections 1.1, 1.2)
- Such missions are not practical with existing deep space propulsion technologies - too great of an orbit insertion ΔV requirement for chemical propulsion, while too distant from Sun for Solar electric propulsion (SEP). (Section 1.3)
- The greatest benefit of the Comet Hitchhiker concept would be to enable them. This is achieved by using a hitchhike maneuver to "stop" a spacecraft at a target for orbit insertion. (Section 3)
- Flight trajectories are available for various targets in the outer Solar System (e.g., KBOs, Centaurs, Jovian Trojans) with the orbit insertion ΔV ranging from $\sim$**1 km/s to** $>$**10 km/s.** Importantly, **the orbit insertion** ΔV **is negatively correlated with flight time.** (Section 3)
  - Example 1: a Pluto rendezvous mission via Jupiter fly-by can be performed by $\Delta V_{OI} = 1.7$ km/s with $\sim$60 year flight time, or $\Delta V_{OI} = 10$ km/s with $\sim$16 year flight time. (Section 3.2)
  - Example 2: a Centaur rendezvous mission to 2060 Chiron can be performed by $\Delta V_{OI} = 1$ km/s with $\sim$23 year flight time, or $\Delta V_{OI} = 7.3$ km/s with $\sim$4.5 year flight time. (Section 3.3)
  - The benefit of a hitchhiker would be maximized by **rendezvousing with multiple targets in a single mission,** which we call a multi-hitchhike mission (MHM). This is because, unlike propellant, a tether can be used multiple times. In particular, a multi-rendezvous tour can be performed with relatively small ($<$2 km/s) hitchhike maneuvers in the main asteroid belt, Trojans, and the Kuiper belt. (Section 3.6)
- The achievable hitchhike ΔV is determined by the tether's specific strength and the mass ratio between spacecraft and tether. This relationship is described the **Space Hitchhike Equation (SHE)**. (Section 4.1)
- 1 km/s hitchhike maneuver is feasible with existing technologies.
  - Harpoon strength: a tungsten projectile at 1.5 km/s impact speed does not experience plastic deformation (Section 6.4)
  - Harpoon penetration: the penetration depth of a tungsten projectile at 1.5 km/s impact speed is 8.8 times of the projectile length for both hard rock and soft soil targets (**only negligible correlation between penetration depth and target strength was observed in this case**). (Section 6.4)
  - Cratering: The maximum diameter of the crater produced by the impact along the final axial location of the projectile is small enough to deploy a latching mechanism: 1.2 times of the projectile diameter for a hard rock target, or 2.2 times of the projectile diameter for a soft soil target. (Section 6.5.1)
  - Tether strength: a Zylon tether (flight-proven on the Mars Exploration Rovers mission) has a tensile strength that can support up to 1.9 km/s of hitchhike maneuver. (Sections 4.1.3, 4.3, 4.4.3)
  - Heat dissipation: in a 1 km/s hitchhike maneuver, the greatest possible temperature increase of a Zylon tether is $\sim$420 K (assuming that 100% of heat goes to tether, distributed uniformly over the length), which is within a tolerable range of the material. (Section 5.2)
- 10 km/s hitchhike maneuver is possible, but would require future advancements in tether material and heat dissipation technologies.
  - Harpoon strength: a diamond projectile at 10 km/s impact speed does experience plastic deformation, but 70% and 83% of the projectile will remain uneroded for hard rock and soft soil targets, respectively. (Section 6.4.2)
  - Harpoon penetration: the penetration depths of a diamond projectile after a 10 km/s impact to hard rock and soft soil targets are 3.36 and 7.29 times of the projectile length, respectively. (Section 6.4.2)
  - Cratering: The maximum diameter of the crater produced by the impact along the final axial location of the projectile is sufficiently small to deploy a latching mechanism: 1.57 times of the projectile diameter for a hard rock target, or 2.0 times of the projectile diameter for a soft soil target, assuming a perpendicular impact. (Section 6.5.1)

  - Tether strength: a carbon nanotube (CNT) tether has a tensile strength that can support up to 10.4 km/s of hitchhike maneuver. However, the technology to produce sufficiently long CNT fiber currently does not exist; the technology to manufacture CNT yarn does exist but it has not reached the tensile strength of CNT fiber. (Sections 4.1.3, 4.3, 4.4.3)
  - Tether deployment is feasible below the velocity limit specified by the Space Hitchhike Equation (SHE) in terms of tension and stability. (Section 4.2)
  - Heat dissipation is a major challenge. The kinetic energy with 10 km/s velocity must be either dissipated, stored, absorbed, or used, in a few minutes. The heat produced in the hitchhike maneuver is comparable to Mars EDL (killed $\sim$6 km/s in 7 minutes). A potential mitigation would be to use a regenerative brake and store the energy or consume it immediately. (Section 5.2)

- Key insights obtained from tether/harpoon simulations include:
  - The crater width after impact is sensitive to the angle of attack (i.e., discrepancy between the harpoon's longitudinal axis and the relative velocity), particularly at a high impact speed. The attitude of harpoon must be controlled in order to reliably attach harpoon to the target. (Section 6.5.1)
  - The maximum tension a tether experiences during a hitchhike maneuver is sensitive to the damping of tether. (Section 4.4.3)
  - The extendable tether can absorb jerks and maintain tension and spacecraft acceleration within acceptable ranges (Section 4.4.3)
  - Counterintuitively, **the penetration depth and remaining length of harpoon after impact has low sensitivity to the strength of the target material**. For example, our simulation results suggest that the penetration depths of a diamond harpoon at 10km/s impact to hard rock (31.7 GPa bulk modulus) and soft soil (0.066 GPa bulk modulus) differ only by 2.17 times. (Section 6.4.2)

Concept art of a Comet Hitchhiker by Cornelius Dämmrich.

Contents

1 Introduction

1.1 New Realization of Small Bodies

The solar system is home to vast populations of small-bodies of which exploration has only just begun. Included are the asteroids and the comets from the Kuiper belt and Oort cloud reservoirs. We now understand that the Kuiper belt feeds a rain of small-bodies into the inner solar system, from the Centaurs (short-lived objects interacting strongly with the giant planets), to the Jupiter family comets (Centaurs trapped by Jupiter) to the dead remnants in the near-Earth population. In addition, N-body modelers suggest that some apparently stable populations long believed to have formed in-situ may in fact have been formed elsewhere and scattered into their present orbital locations. Included are the outer belt asteroids, the irregular satellite populations and the Trojan "asteroids", some or all of which might have been captured from the Kuiper belt.

The new realization, then, is that numerous small-body populations that were previously thought to be unconnected are now seen to be closely related. Essentially, we now possess, for the first time, a broad context from which the nature and evolution of the small-body populations can in principle be understood. Discovery and exploration of the Kuiper belt has, in particular, triggered a dramatic burst of new understanding concerning the origin and evolution of the solar system. Notably, the discovery of heavily-populated Kuiper belt mean-motion resonances requires planetary migration, which in turn implies a solar system dynamical history much more complex and less predictable than previously assumed.

The small-body populations are enormous (there are about a million asteroids, about a billion Kuiper belt objects and 100 billion Oort cloud comet nuclei bigger than a kilometer) but, because they are small, carry very little mass. Although the small bodies contain a negligible fraction of the total mass of the solar system, they carry a disproportionately large fraction of the science content. (The small bodies are thus analogous to radioactive atomic nuclei - although the latter are rare they tell us much more about nuclear physics than could ever be guessed from the study of stable atoms.). Many of the questions regarding small bodies could only be addressed in-situ by spacecraft. Unfortunately, studies of the richness and diversity of the small body populations are hampered by the limited number of rendezvous opportunities with these bodies, itself an artifact of established propulsion techniques.

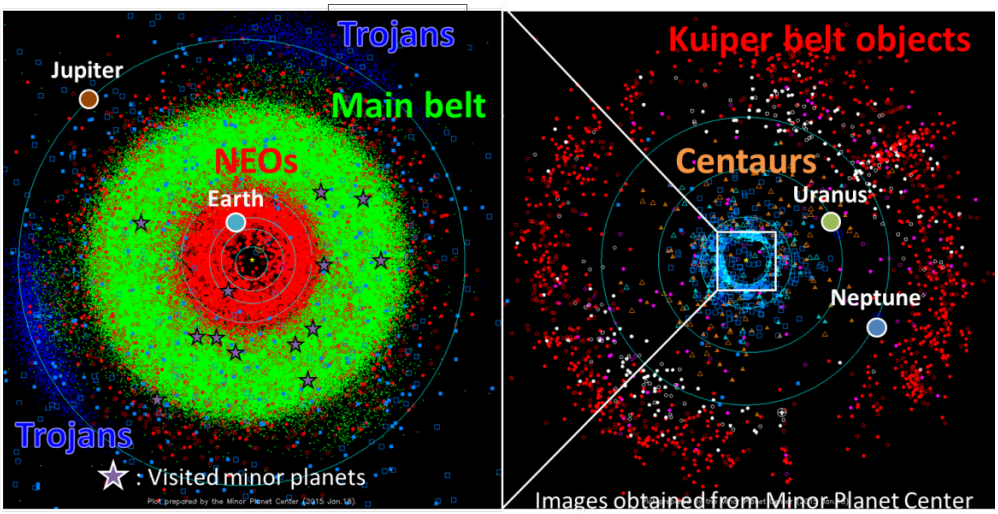

Figure 3: Distribution of known small bodies in the Solar System. The stars are the small bodies that have been visited by spacecraft. Note that all visited small bodies are either NEOs, main belt objects, or short-period comets.

1.2 Significance of Rendezvous Missions to Small Bodies

The importance of rendezvous over fly-by missions cannot be overstated. Compare ESAs Giotto fly-by mission to comet Halley with their rendezvous mission to 67P/Churyumov-Gerasimenko. The former was able only to establish the approximate size and shape of the nucleus and provided limited compositional data from mass-spectrometers

Table 1: Number of Solar System objects by category that have been found, visited, and rendezvoused/landed. While all the eight planets in the Solar System have been visited by spacecraft, a very small fraction of small bodies have been subject to detailed exploration. Despite of their sizes, they holds significant information about the content, origin, and evolution of the Solar System. Note that, as we discussed in Section 1.1, the boundary between asteroids and comets has become fuzzy due to recent discoveries.

	Found	Visited	Rendezvoused/landed
Planets	8	8	6
Asteroids	670,444	13	4
Comets	3,830	8	1

on-board. The latter is revealing the entire surface of 67P at meter-scale resolution, opening up new avenues in planetary geology, providing detailed compositional information and allowing the temporal variation of the activity to be measured as the comet sweeps through perihelion. There is even the prospect of an internal structure map from long wavelength radio penetration. Likewise, the NASA New Horizons mission to Pluto, which is exciting because it is the first such encounter with a Kuiper belt object, cannot possibly provide rich detail and context of the type offered by the NASA DAWN mission to large asteroids Vesta and Ceres. In addition to providing high-resolution, multi-wavelength mapping of the entire surface of a body, invaluable for understanding its surface processes, rendezvous missions offer the possibility to determine masses and densities, to determine internal structure by gravitational anomalies and the use of long-wavelength radio waves, and to measure the time-evolution of mass loss processes from active objects. None of these quantities can be addressed from a fly-by.

1.3 Challenges in Small Body Rendezvous

Although Cassini arrived at $V_\infty \sim 6$ km/s in relative to Saturn, only 0.62 km/s of ΔV (meaning the change in velocity) was required for orbit insertion. If Saturn were a small body, it would require $\sim$6 km/s of orbit insertion ΔV. As shown in this example, small body rendezvous is particularly challenging because it requires significantly greater orbit insertion ΔV than planet orbit insertion. Due to the negligible gravity of small bodies, the relative velocity between spacecraft and a target must be almost entirely killed in order to be trapped by the gravity of the target.

Achieving a greater ΔV requires a greater mass ratio between propellant and the spacecraft. According to the Tsiolkovsky rocket equation, the ratio grows exponentially with ΔV. For example, inserting New Horizons into a circular orbit around Pluto would require $\sim$12.5 km/s of orbit insertion ΔV in addition to the $\sim$16 km/s ΔV for the departure from Earth. In order to perform the orbit insertion maneuver with a chemical engine (assuming ISP = 312 sec, same as Cassinis main engine), 98.3% of the mass of the spacecraft must be propellant. In other words, in order to put a spacecraft with 0.5 metric tons of dry mass (approximately the same as New Horizons) around a Pluto orbit, a spacecraft with $\sim$30 tons of wet mass must be injected to a trans-Pluto orbit.

In contrast, orbit insertion to a planet is significantly easier in terms of ΔV. For example, as we mentioned, the Saturn orbit insertion (SOI) of Cassini only required 0.62 km/s of ΔV, or just 18.3% of the propellant mass in relative to the spacecraft mass. There are two reasons for the relatively small ΔV for planetary orbit insertion. First, a stronger gravity increases the escape velocity. Second, a greater reduction in orbital energy can be achieved if ΔV is given at a higher relative velocity. Therefore spacecraft can save ΔV significantly by performing the orbit insertion burn when it is significantly accelerated by the gravity of the planet (i.e., at the closest approach to the planet.

For these reasons, the small bodies feasible for rendezvous/landing have been limited to near-earth objects (NEOs) or short-period comets, which accounts for only a fraction of the entire population of the small bodies. NEOs account for $\sim$1.7% of the asteroids[1]; short period comets account for 19% of all known comets. (Note that there is an observation bias since asteroids and long period comets in the outer Solar System are much harder to find.) As we discussed previously, there are scientifically interesting small bodies in the outer Solar System, such as Jovian Trojans, Centaurs, and KBOs, which must be visited and investigated in detail in order to ascertain the content, origin, and evolution of the Solar System.

[1]As of Jan 18, 2015, there are 670,444 identified asteroids whose orbit has been determined. Among them, 11,600 are identified as NEOs, as of November, 2014. Data source: NASAs Near Earth Object Program (http://neo.jpl.nasa.gov/stats/) and the IAU Minor Planet Center (http://www.minorplanetcenter.net/iau/mpc.html).

Figure 4 shows the orbit insertion ΔV for various targets in the Solar System and the approximate domains covered by existing deep space propulsion methods i.e., chemical propulsion and SEP[2]. Although chemical propulsion can be used at any distance from Sun, the realistic level of orbit insertion ΔV that it can provide is a few km/s at most. While Solar electric propulsion (SEP) can provide significantly greater ΔV, it is not a realistic option in the outer Solar System due to insufficient Solar flex. An alternative deep space propulsion method is solar sail, which has been flight validated by the IKAROS mission [34]. However, like SEP, solar sail can provide ΔV only in the inner Solar System.

As a result, many scientifically significant targets, particularly the small bodies in the outer Solar System, are left uncovered by existing propulsion methods for rendezvous. As we discuss in detail in the rest of this report, the benefit of the Comet Hitchhiker concept is to push the boundaries and enable rendezvous missions to small bodies in the outer Solar System.

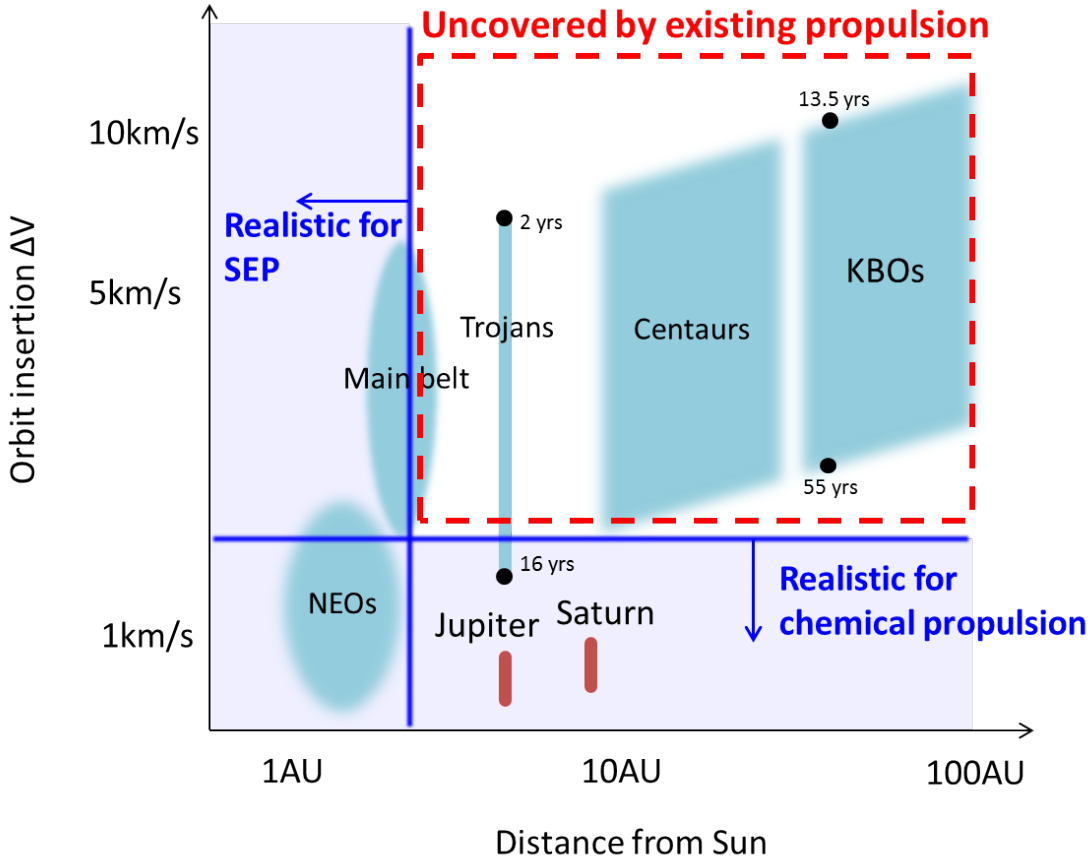

Figure 4: Orbit insertion ΔV for various targets in the Solar System and the approximate domains covered by existing deep space propulsion methods (chemical propulsion and SEP). Chemical propulsion can be used at any distance from Sun but the achievable ΔV is limited. SEP can achieve significantly A higher ΔV but its use is limited in the inner Solar System. A hitchhiker has potential to push these boundaries.

1.4 Composition of the Report

The objective of this Phase I study is to 1) establish basic feasibility and 2) clear potential benefit of of the Comet Hitchhiker concept. The rest of this report is organized accordingly. First, Section 2 introduces the concept. Then, Section 3 discusses the benefit of the concept. Sections 4-7 present the results of feasibility analysis.

[2]Note that, as we analyze in detail in Section 3, there are diverse options of trajectory to get to a target. In general, a trajectory with a lower orbit insertion ΔV requires a longer flight time. For example, in case of Pluto, a trajectory with 13.5 year transfer time requires 10 km of orbit insertion ΔV, while one with 55 year transfer time requires 2.5 km/s of ΔV. (See Section 3.2 for details.)

2 Concept

2.1 Concept Overview

The Comet Hitchhiker concept is essentially to perform momentum exchange with a target body using an extendable/retrievable tether. The momentum exchange is performed in two ways: i) to kill the relative velocity with the target, and ii) to accelerate the spacecraft in relative to the target. We call the former a *space hitchhike maneuver*, while the latter is called an *inverse space hitchhike maneuver*. The most unique aspect of the concept is to use extendable/retrievable tether, which enables: 1) to control the spacecraft acceleration within a tolerable level, 2) to absorb jerks, 3) to harvest the kinetic energy of the target body, and most importantly, 4) to change or completely kill the relative velocity with the target, hence enabling rendezvous and landing.

Space Hitchhike Maneuver As illustrated in Figure 5, first, the spacecraft would harpoon a target as it makes a close fly-by in order to attach a tether to the target. Then, as the target moves away, it would reel out the tether while applying regenerative braking to give itself a moderate (<5g) acceleration. If there is a sufficient length of tether, the spacecraft can eventually make the relative velocity sufficiently small so that it is captured by the weak gravity of the target. At the end of the hitchhike maneuver, the spacecraft would be at a significant distance from the target - typically 10-1000 km, depending on the initial relative velocity. Closing in on the target is easy because the relative velocity has already been killed. The spacecraft can simply retrieve the tether slowly to come closer to the target, and possibly land on it. Figure 6 shows a sample sequence of a hitchhike maneuver.

This idea can be intuitively understood by the analogy of fishing. Imagine a fisherman on a small boat trying to catch a big fish that swims at a high relative speed. Once the fish is on a hook, the experienced fisherman would let the line go while applying a moderate tension on it, instead of holding it tightly. If the line has a sufficient length, the boat can eventually catch up with the fish with moderate acceleration.

In addition, by applying regenerative braking, a Comet Hitchhiker could harvest energy from the target body. Assuming 25% efficiency of a regenerative brake, a 2-ton comet hitchhiker can produce ∼25 GJ of energy, which is sufficient to drive an instrument with 1 kW power consumption over 290 days. If future storage devices can achieve the energy density of gasoline, 25 GJ can be stored in 500 kg of mass, making it a potential energy source in the outer Solar System.

Our concept brings important advantages over a related concept of tether-based fly-by [26], which would use a fixed length of tether in order to change the direction of the relative velocity like a gravity assist. This concept could not be used for landing and orbit insertion because it does not reduce the relative speed. The comet hitchhiker concept is distinct in that it reels out a tether while applying regenerative brake force to accelerate itself. This approach allows the spacecraft to match its velocity with that of the target, and as a result, enables soft landings and orbit insertion.

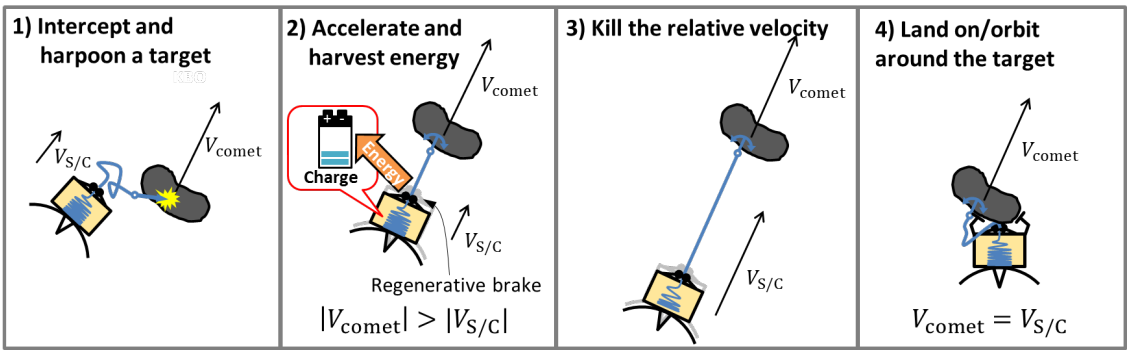

Figure 5: Space hitchhike maneuver for small body rendezvous/landing

Figure 6: A sample sequence of a space hitchhike maneuver, simulated by the finite element simulator introduced in Section 4. The size of spacecraft is exaggerated for visualization purposes

.

Inverse Space Hitchhike Maneuver In order to rendezvous with multiple targets in a single mission, a hitchhiker also needs to be able to depart from a target. A hitchhiker would make a fuel-less acceleration by performing an inverse hitchhiker maneuver, as shown in Figure 7. First, when the hitchhiker is on the surface or in orbit, it would attach a tether to the target. Next, it would slowly move away from the target while deploying the tether. Then, it would accelerate itself by pulling in the tether. The energy harvested from the previous hitchhike maneuver could be used to pull in the tether. Finally, once the desired velocity is achieved, the spacecraft would detach the harpoon and fly away to the next target.

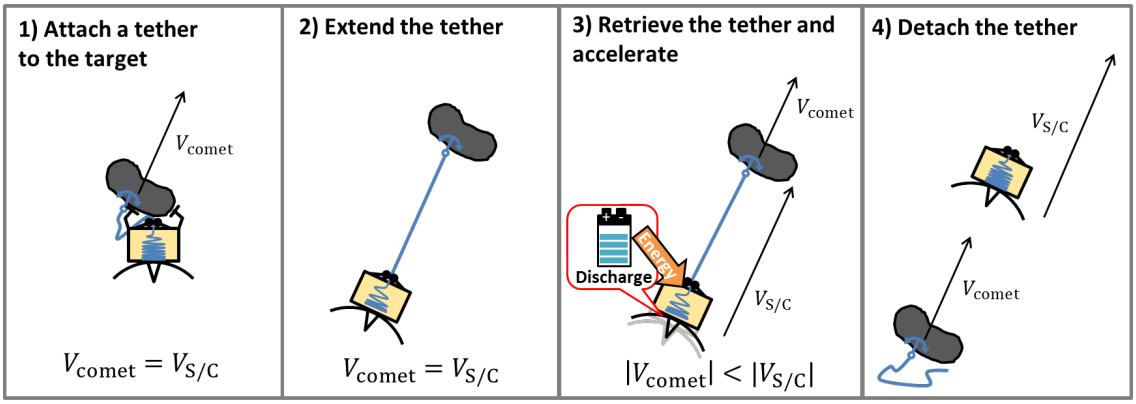

Figure 7: Inverse hitchhike maneuver to depart from a small body

2.2 Overview of capability

As we will discuss in Section 4, the main limiting factor in the achievable ΔV by a hitchhike maneuver is the specific strength of the tether (i.e., tensile strength divided by density). With flight-proven tether materials such as Kevlar and Zylon, a hitchhiker can perform up to $\sim$2 km/s deep space maneuver, which is sufficient to conduct a multi-hitchhike tour in Main Belt as discussed in Section 3.6, or to perform Pluto rendezvous mission with $\sim$ 60 year flight time. With the strongest existing material, carbon nanotubes, a hitchhiker can perform a $\sim$10 km/s maneuver, which would enable fast rendezvous/landing missions to a diverse type of small bodies, such KBOs, long period comets, Centaurs, and Jupiter Trojans (e.g., 16 year flight time for a Pluto rendezvous mission). However, an issue is that the longest fiber to date is only $\sim$50 cm long [38]. Technologies exist to manufacture a long tether made of multitudes of short CNT fibers called CNT yarn[4, 25], but its strength is still far behind the strength of CNT fibers.

Therefore, the hitchhiking capability will be developed incrementally. The first hitchhiker will use a Zylon/Kevlar tether and perform missions that requires up to $1-2$km/s maneuvers. As we analyze in Sections 6, with this level of relative velocity, harpoon with a regular metal material such as tungsten is feasible; heat produced by applying brake on the tether is within a tolerable level. Unlike propellant, a tether can be used multiple times. Hence, a greater total ΔV can be obtained by repeating hitchhike maneuvers in a single mission. We call such a mission a *multi-hitchhike mission* or MHM, which will be discussed in detail in Section 3.6. For example, visiting multiple objects in the main asteroid belt will be a scientifically significant applications of MHM.

In mid- to long-term, when a tether material with greater specific strength becomes available, a hitchhiker will be able to perform more radical maneuver. A hitchhiker capable of $\sim$10 km/s hitchhiker maneuver would enable fast rendezvous/landing missions to small bodies in the outer Solar system.

2.3 Overview of major risks

A hitchhiker performs a very radical maneuver that involves 1-10 km/s velocity change just in few minutes, which is comparable to entry, descent, and landing (EDL). For example, Mars EDL kills $\sim$6 km/s of relative velocity just in 7 minutes. Performing such a radical maneuver with harpoon and tether would involve various risks.

Risks investigated in depth in Phase I The greatest risks of the hitchhiker concept resides in three mechanical subsystems: tether, harpoon, and brake. The feasibility of the concept rests upon the feasibility of these critical subsystems. Therefore, a major focus of the project is given to the feasibility study of the three mechanical components. More specifically, the followings are major risks concerning tether, harpoon, and brake:

1. Tether (Section 4)
   (a) Strength: Can a tether tolerate the tension required to perform the radical maneuver?
   (b) Line dynamics: Can a tether tolerate the jerk after the impact?
   (c) Deployment: Can a spacecraft reliably deploy a tether at the required rate of deployment (1-10 km/s)?
2. Harpoon (Sections 6 and 7)
   (a) Strength: Can a harpoon tolerate a hypervelocity impact?
   (b) Penetration: Can a harpoon penetrate into the target instead of creating a crater?
   (c) Attachment: Can a harpoon reliably stay in the target after impact and support the tension of the tether?
   (d) Uncertainty in target characteristics - Can a harpoon be robust to the uncertainty in the characteristics (e.g., composition, strength) of target bodies?
3. Brake (Section 5)
   (a) Control: Can a brake system reliably control the tether tension at hypervelocity?
   (b) Heat: Can a brake system tolerate the heat produced from braking?

Our main approach to answer these questions is simulation. We developed a finite-element tether simulation model, as well as a numerical simulation of the hypervelocity impact of harpoon. The harpoon impact simulation was performed on a supercomputer cluster in order to achieve sufficient spacial and temporal resolution. As for brake, we employ a bounding approach where the bounds on available brake force and heat are analytically obtained.

Risks with existing mitigation technologies Technologies exist to mitigate several apparent risks to the Comet Hitchhiker concept.

- Targeting accuracy - the risk that a harpoon misses the target
  - There has already been a matured GN&C technology to achieve necessary shooting accuracy by the fact that Deep Impact successfully impacted the comet 9P/Tempel at the relative speed of 10.3 km/s [19]. The size of the comets nucleus is 7.6 x 4.9 km, which is a typical size among the comets whose nucleus size has been precisely determined.
- Spin - the risk that the spin of a target makes the hitchhiking maneuver impossible
  - The measured rotation periods of cometary nuclei are in the 4 to 40 hour range, while the hitchhiking maneuver would take up to $\sim$3 minutes, assuming $\sim$5g acceleration and 10 km/s ΔV.
- Comet activity - the risk that the activity of comet damages the spacecraft
  - A European spacecraft Giotto successfully performed a close flyby of very active Halley's Comet at 596 km distance in 1986 and returned data afterwards, despite partial damages.
  - There is a class of comets called Damocloids that are known to be inactive even near the Sun [14]. They are considered to be dead or dormant comets, which themselves are very interesting science targets. As of July 2013, there are 53 known Damocloids. Damocloid rendezvous mission is analyzed in detail in Section 3.4.

Risks newly identified in Phase I As we will discuss in Section 6.5.2, we found in our Phase I analysis that harpoon penetration is sensitive to the angle of attack. This means that the attitude of the harpoon needs to be accurately controlled before the impact, otherwise it may end up with creating a crater instead of penetrating. Attitude control of harpoon will be investigated in detail in a proposed Phase II study.

3 Mission Analysis

3.1 Summary of Analysis

There would be two types of hitchhiking missions: *single hitchhike mission (SHM)* and *multi hitchhike mission (MHM)*. SHM is comparable to *Galileo* and *Cassini* missions, where a spacecraft performs a single hitchhike maneuver to rendezvous with a target and observe it for a relatively long duration. MHM is comparable to *Dawn*, where a spacecraft rendezvouses with multiple targets by repeating hitchhike and inverse hitchhike maneuvers. We performed mission utility analysis for both SHM and MHM.

3.1.1 Single Hitchhike Mission

Our major findings include followings:

- Orbit insertion ΔV is negatively correlated to the flight time from Earth to the target (See, for example, Figures 8 and 11.)
- The minimum ΔV requirement for orbit insertion around small bodies in the outer Solar System (KBOs, Centaurs, Jupiter Trojans) is $\sim$1-2 km/s. This is not impossible but is an unprecedented level of deep space maneuver for chemical propulsion.
- A hitchhiker can provide ΔV that is well beyond the minimum requirement. It is an enabler of the rendezvous missions to small bodies in the outer Solar System. Future advancement in tether materials will further increase available ΔV, which in turn shortens flight time.
- Jupiter flyby is useful to reduce the orbit insertion ΔV by increasing perihelion, but with a cost of a longer flight time. (Intuitively, in this case, we reduce the orbital velocity through fly-by instead of increasing it.)

We performed analysis for four types of targets: KBOs, Centaurs, Jupiter Trojans, and Damocloids, which will be described in detail in Sections 3.2-3.5. The analysis results are summarized in Table 2. Note that, for each target, the table shows two extreme design points of a mission (one with the minimum flight time with a 10 km/s upper bound on ΔV, while the other being the minimum ΔV and a long flight time.) The point is , again, there is a trade-off between ΔV and flight time. **A hitchhiker mission can be flexibly designed between the two extrema**.

Table 2: Summary of the single hitchhike mission analyses. Shown in the table are two extreme point designs of each mission. The results in in the "Min. flight time" columns are obtained by minimizing the flight time with a 10 km/s upper bound on the orbit insertion delta-V. The results in the "Min. ΔV_{OI}" columns are obtained by minimizing the orbit insertion delta-V.

Mission Concept	Target	Min. flight time s.t. $\Delta V_{OI} \leq 10$ km/s		Min. ΔV_{OI}	
		ΔV_{OI}	Flight time	ΔV_{OI}	Flight time
KBO rendezvous	Pluto (direct)*	10 km/s	13.5 yrs	2.6 km/s	40 yrs
	Pluto (Jupiter fly-by)	10 km/s	16 yrs	1.7 km/s	60 yrs
	Makemake	10 km/s	21.5 yrs	-	-
Centaurs rendezvous	2060 Chiron	7.3 km/s	4.5 yrs	1 km/s	23 yrs
Damocloid rendezvous	1999 RG33	9.6 km/s	1 yrs	-	-
Trojan rendezvous	L4 (659 Nestor)	6.9 km/s	1.9 yrs	2.7 km/s	10 yrs
	L5	-	-	1.5 km/s	16 yrs

*In addition to the orbit insertion maneuver, direct trajectory to Pluto requires a large deep space maneuver ($\sim$2.1 km) for plane change due to the high orbital inclination of Pluto.

3.1.2 Multi Hitchhike Mission

Propellant is gone once it is used. However, a tether can be retrieved after a hitchhiker maneuver for repeated use[3]. MHM reinforces the benefit of the Comet Hitchhiker concept as it would enable achievement of greater total ΔV without increasing significantly increasing spacecraft mass. MHM would also make a hitchhiker useful in a relatively short time since, even with a relatively small ΔV achievable by existing tether materials, a hitchhiker could gain a significant advantage over conventional propulsion for a mission that requires rendezvous with multiple targets.

An ideal near-term destination for MHM is the main asteroid belt. In fact, as we will discuss in Section 3.6.1, our study found that rendezvous with multiple targets in the main belt will bring new insights about asteroid families and active asteroids. To demonstrate the feasibility of MHM, we computed a trajectory that sequentially rendezvouses with the eight major member of the Themis family. The required ΔV for each hitchhike/inverse hitchhike maneuver is at most 1.6 km/s, which can be achieved by a Kevlar or Zylon tether[4].

3.2 KBO rendezvous mission

3.2.1 Science Objective

Kuiper belt objects are primordial relics from the protoplanetary disk. Science Objectives would include: 1) Orbit to study the complete surface using optical/IR/gamma ray spectrometry, measure crater counts, dust release through micrometeorite impact, interior structure from orbit perturbations. 2) Use Hitchhiker to circularize the outward trajectory and enable long-term presence in the Belt, e.g. to move from object to object or to measure the micrometeorite and interstellar dust fluxes over a solar cycle.

3.2.2 Trajectory Analysis

We performed a detailed trajectory analysis for orbit insertion around Pluto and Makemake, two of the greatest KBOs.

Pluto Although New Horizons has flown by Pluto and might potentially fly by other KBOs, it is only allowed a few days for observation. As we found in Section 1.2, orbiting around a KBO is essential for thorough understanding of the subject. KBO Hitchhiker would be to New Horizons what Galileo and Cassini are to Voyager.

Orbit insertion around KBO is significantly more challenging than around gas giants because of small gravity. For example, the Saturn orbit insertion maneuver of Cassini only required 0.62 km/s of ΔV, even though the spacecraft arrived at the ringed planet at $V_\infty = \sim 6$ km/s in relative to Saturn. For a small planetary body like Pluto, the ΔV required for orbit insertion is almost identical to V_∞. For example, inserting New Horizons into an orbit around Pluto requires $\sim$12.5 km/s of ΔV. Trajectory with smaller arrival V_∞ are available but result in significantly longer flight time. Pluto Hitchhiker could be a solution; instead of hitching a comet, we use the hitchhike maneuver at Pluto to slow the spacecraft down. We performed trajectory optimization with a constraint V_∞. Figure 8 shows the result of the optimization, where the vertical axis is the flight time while the horizontal axis is V_∞ at arrival.

With 10 km/s orbit insertion ΔV, the following two trajectory options are available :

- Direct flight to Pluto (13.5 years). This option is fastest but requires large deep space maneuver ($\sim$900 m/s) and highest C3 ($\sim 200\text{km}^2/\text{s}^2$). See Figure 8.
- Jupiter flyby (16 years) to slow down the trajectory. This option takes longer flight times but much lower C3 ($\sim 90\text{km}^2/\text{s}^2$) and requires no DSM. Launch opportunities are available in 2015-2017 and 2027-2029.

As shown in Figure 8, the flight time and orbit insertion ΔV is negative correlated. Therefore, if a hitchhiker maneuver greater than 10 km/s is made feasible by future advancement in tether material, the flight time of Pluto Hitchhiker could be shorter. Performing a 10km/s maneuver in deep space by chemical propulsion is practically impossible since, with ISP = 312 sec (same as Cassinis main engine), 96% of the spacecraft mass must be occupied by propellant.

With a longer flight time, the orbit insertion ΔV can be smaller, but there is a lower bound, as shown in 8. We cut off the analysis at 40 years for direct flight and at 60 years for Jupiter flyby and Jupiter-Saturn flyby. The direct flight option has disadvantage in that it requires deep space maneuver, which cannot be performed by hitchhiking. The Jupiter fly-by option with 60 year flight time requires a 1.7 km/s orbit insertion $\Delta - V$.

[3]However, harpoon is not reuseable. Therefore a hitchhiker for MHM would need to carry multiple harpoons.

[4]However, the orbit insertion maneuver with the first target would require greater ΔV than the feasible range with Kevlar/Zylon. Hence the first rendezvous would require a combination of hitchhike and conventional propulsion.

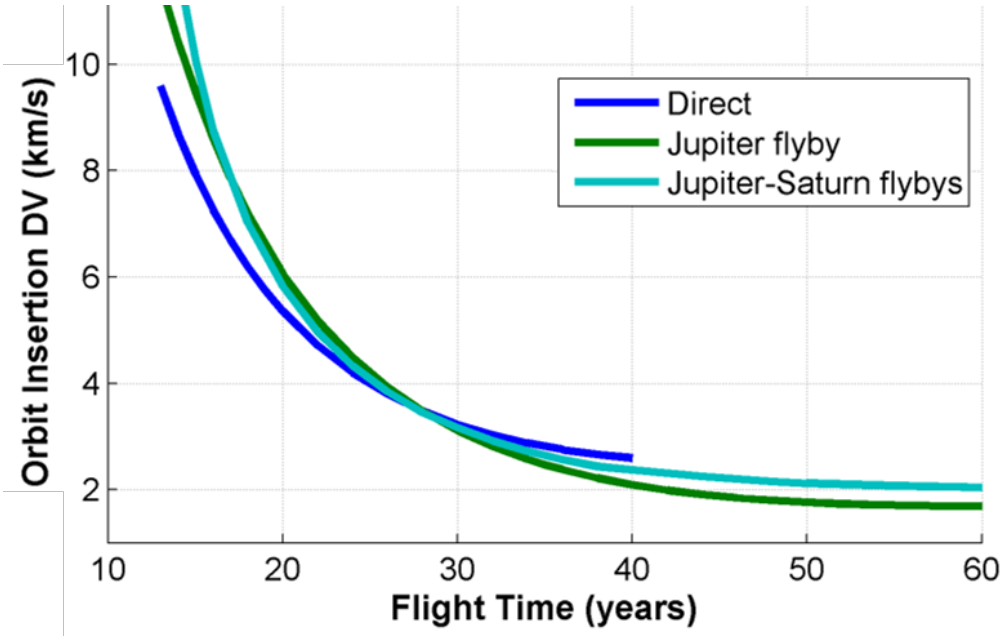

Figure 8: The orbit insertion ΔV to Pluto for trajectories with specified fight time[5]. A wide range of trajectory options are available, but a faster flight time can only be achieved with a cost of greater orbit insertion ΔV.

As we discuss in Section 4, 1.7 km/s hitchhike can be performed by existing tether materials, such as Zylon. On the other hand, 10 km/s hitchhike would require a carbon nanotube tether. This poses an interesting trade-off between mission duration and technology development time. The two extreme ways to design a Pluto rendezvous mission are:

1. Use existing technologies to build a hitchhiker that can perform 1.7 km/s maneuver, launch it in near-term, and wait for 60 years until the rendezvous, or
2. Wait until CNT technologies mature, build a hitchhiker that can perform 10 km/s maneuver, and arrive at Pluto within 15 years from launch.

A realistic option should lie between the two extremums. A Pluto hitchhike mission should be designed to balance science return, required technology development, mission cost, and risk.

Makemake We also performed preliminary mission design analysis to Makemake, the largest known classical KBO. It has no known satellite, so it is unlikely that it has suffered a giant impact, contrary to Pluto.

The primary focus of this analysis was to determine flight time and ΔV requirements for trajectories from Earth to Makemake with arrival V_∞ values below 10 km/s. Gravity assists of Jupiter and Saturn are not considered in this analysis. Trajectories from Earth to Makemake were computed using MIDAS, an interplanetary trajectory optimization tool that is able to add or delete deep space maneuvers [28]. For a given flight time, MIDAS was run to find the optimal trajectory (minimizing total ΔV) without constraining the arrival V_∞. Figure 1 shows the sensitivity of arrival V_∞ and total ΔV with respect to flight time for a 2019 launch. A flight time longer than 21.5 years is required to ensure that the arrival V_∞ is below the 10 km/s threshold, yielding a total mission ΔV below 15 km/s. Note that a mission to Makemake will necessarily have a long flight time because Makemake is near aphelion (53 AU from the Sun, reached in 2033) during the next 50 years. Since New Horizon is targeting Pluto near perihelion, targeting Makemake at aphelion can be scientifically attractive, as it would offer some insights into the seasonal cycles of KBOs.

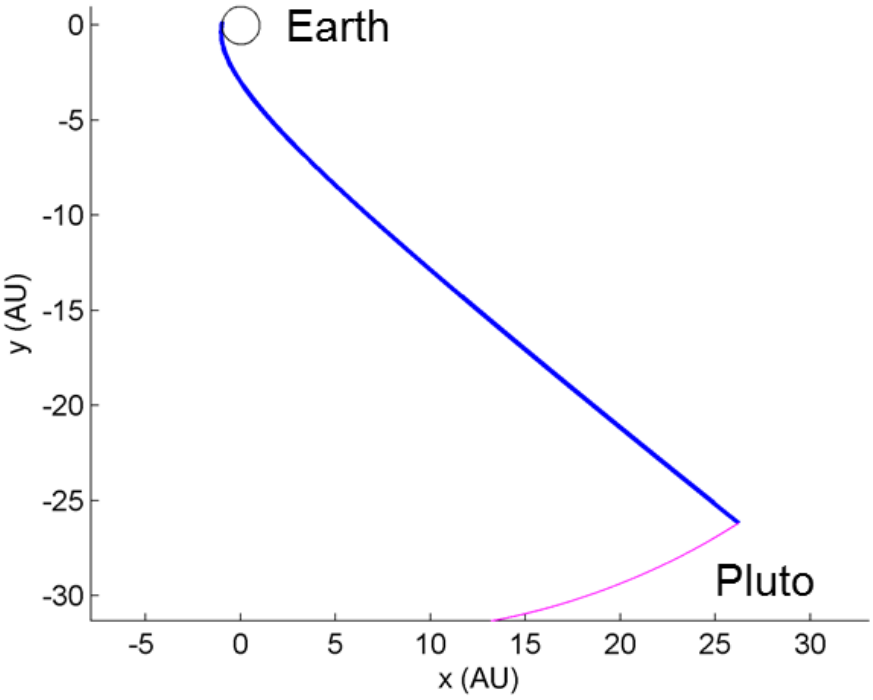

Figure 9: Example of direct Earth-to-Pluto trajectory (2020 launch)

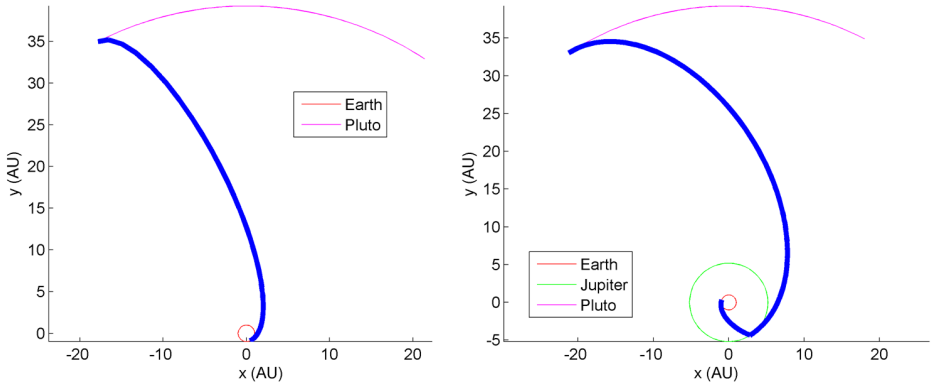

Figure 10: Trajectories to minimize ΔV for orbit insertion around Pluto. Left: direct (45 years), right: Jupiter fly-by (55 years)

3.3 Centaur Rendezvous Mission

3.3.1 Science Objective

Centaurs are thought to be escaped Kuiper belt objects on a 10 Myr journey to the inner solar system and death as a short-period comet. The science objective would be to assess driver of activity beyond Jupiter (where water is frozen solid), find evidence for amorphous ice, measure outgas species (esp. noble gases). Study from orbit would permit time-evolution of activity to be studied and allows difficult low gas flux measurements (with mass spectrometer).

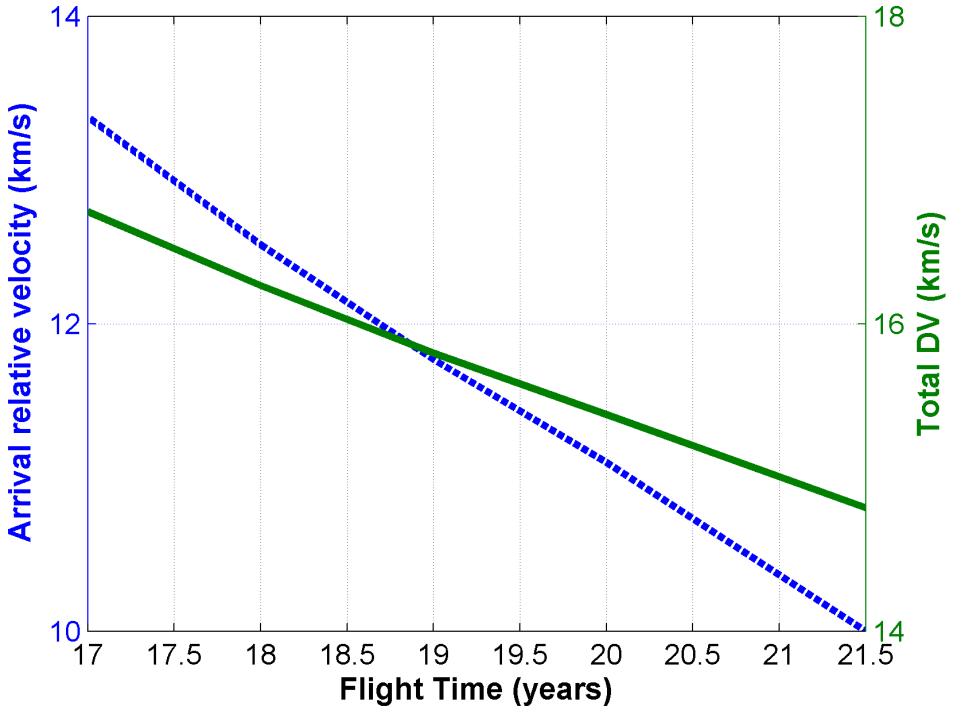

Figure 11: Trajectory optimization result for an orbiter mission around Makemake

3.3.2 Trajectory Analysis

We chose 2060 Chiron, the first-known member of centaurs, as the target of our analysis.

As presented in Figure 12, a Centaur Hitchhiker can fly to Chiron in 4.5 years with a direct orbit and arrive at 7.3 km/s relative velocity, which is killed by the hitchhike maneuver. However, this level of maneuver is impractical for chemical propulsions. Chiron is well beyond Jupiters orbit, meaning that SEP is also not a practical option. A realistic trajectory for Chiron orbit insertion would be to use Jupiter flyby to increase the perihelion and hence decrease the arrival relative velocity to $\sim$1 km/s. This flight trajectory requires 23 years to complete.

3.4 Damocloid Rendezvous Mission

3.4.1 Science Objective

Damocloids are defined as minor solar system bodies which have small Tisserand invariants (TJ < 2), like comets, but which show no evidence for cometary activity. They are widely believed to be the dormant or dead nuclei of comets. The orbital element distribution of the Damocloids, of which 107 are known as of 2015 March 10, is similar to that of the Halley-family comets. The latter are objects (famous comet 1P/Halley is the prototype) that most likely derive from the Oort cloud, although the dynamical details of their origin are unclear. The Halley-family comets show a range of inclinations much larger than that of Jupiter-family comets, including a fraction of objects which are retrograde, but with a bias toward prograde orbits that is distinct from the isotropic distribution of the Oort cloud comets.

Scientifically, the Damocloids offer the opportunity to study the nuclei of objects that have been stored for almost the entire 4.5 Gyr history of the solar system in an essentially interstellar medium environment (the Oort cloud source extends to $\sim$50,000 AU where the Sun is little more than a background source of radiation and particles, and equilbrium temperatures are $\sim$10 K, only slightly higher than that of the cosmic microwave background). Their surfaces are presumed to consist of refractory materials left behind after the loss of volatiles by sublimation on past orbits. Unlike the Jupiter-family comets, the Damocloids have in general experienced much less thermal evolution and mass loss, so that their properties may be more pristine. The nucleus of 67P/Churyumov-Gerasimenko recently visited by the ESA

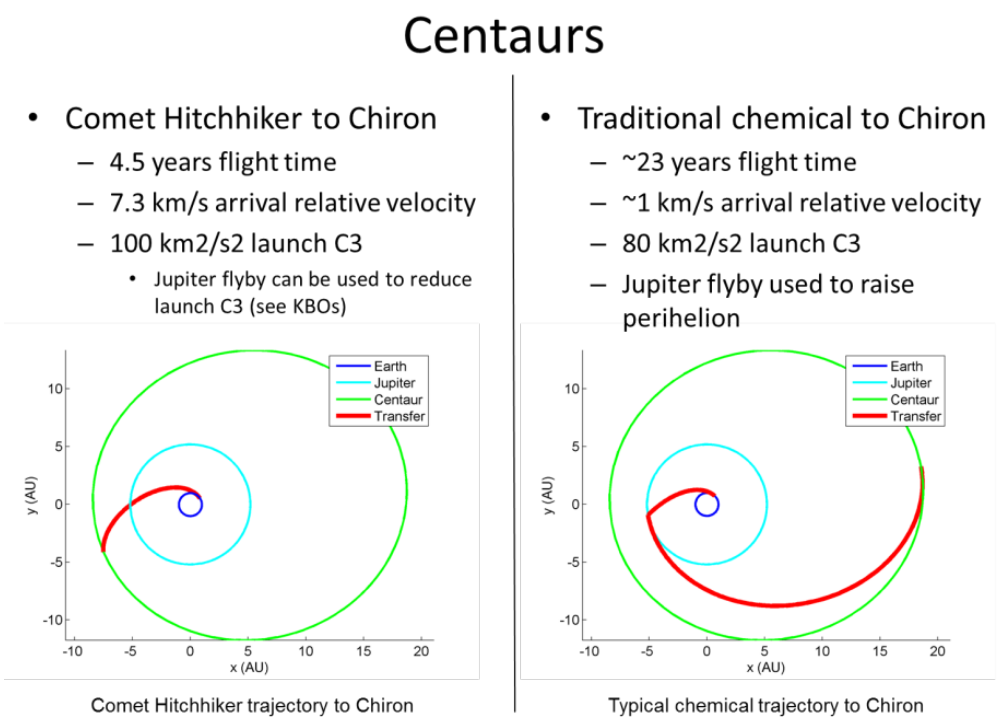

Figure 12: Trajectories to 2060 Chiron, the first-known member of Centaurs

Rosetta mission, for example, has been entirely shaped by protracted mass-loss when near the Sun, probably losing in the past more mass than currently remains in the nucleus. Neither the shape nor the spin nor the surface of this body can be expected to be primordial. On the other hand, the surface of a Damocloid might well preserve a record of interstellar cratering, from debris that has been scattered out of protoplanetary systems across the galaxy. Imaging of the surface of a Damocloid would give the integrated flux and the size distribution of the impactors, two numbers that are essential to an understanding of the solid mass-balance of the interstellar medium. Measurements of the surface mantle of a Damocloid would reveal the influence of long-term irradiation in the interstellar environment.

3.4.2 Trajectory Analysis

Like long period comets, Damocloids have diverse inclination. Only low-inclined Damocloids would be accessible by either hitchhiking or conventional propulsion. Figure 13 shows a trajectory for orbit insertion around a Damocloid, 1999 RG33. Upon arrival, orbit insertion is achieved by a hitchhike maneuver with 9.6 km/s delta-V. The flight time is approximately a year.

Since the perihelion of Damocloids is typically small, SEP can be used to perform orbiting mission to them, as shown in Figure 14. However, in the case of 1999 RG33, the flight time is extended to 5.1 years, and a high power level (46kW; ARRM level) is required.

3.5 Jovian Trojan Rendezvous

3.5.1 Science Objective

Jovian Trojans objects co-move in Jupiters orbit, separated from it by ± 60 degrees of longitude. Their origin is unknown, with two main ideas; 1) they were captured locally from the disk or 2) they were captured long ago from the outer solar system, maybe the Kuiper belt. Rendezvous would enable the first detailed study from orbit. Crater counts, surface morphology would give history. Composition from lander would give origin.

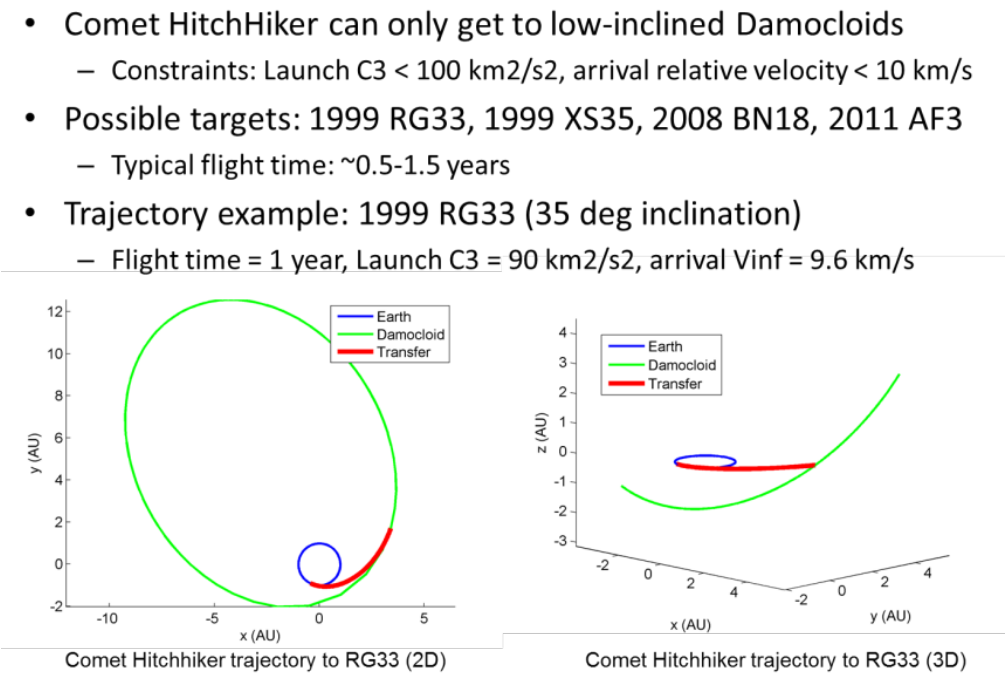

Figure 13: Hichhikers Trajectory to 1999 RG33, a low-inclined Damocloid

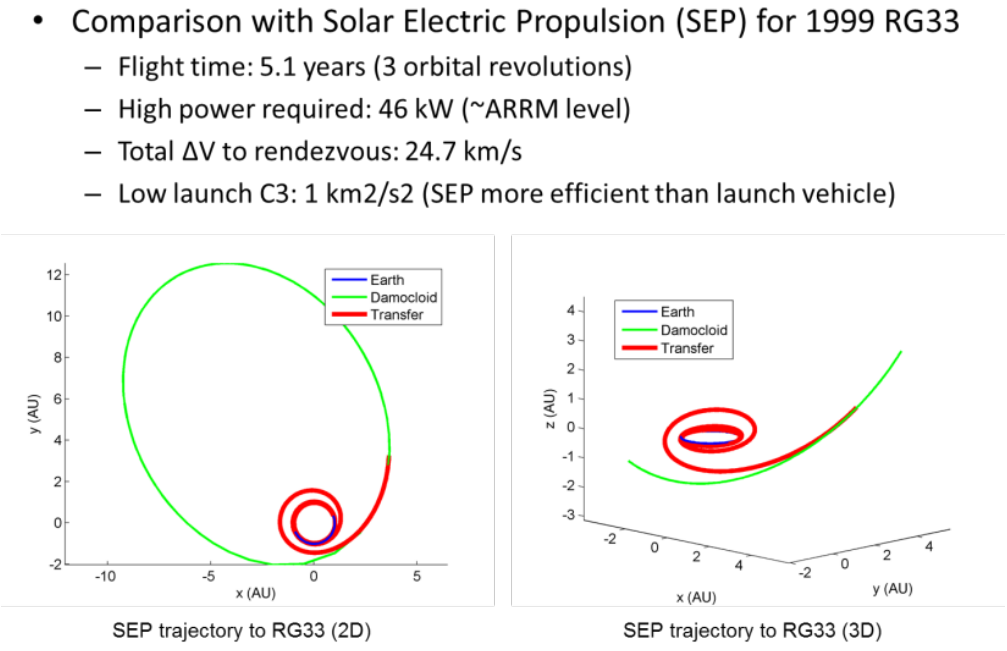

Figure 14: Trajectory to 1999 RG33 using SEP

3.5.2 Trajectory Analysis

There are two groups of Trojans, located at L4 and L5 of Jupiter. For both groups, a Trojan Hitchhiker can get there in $\sim$2 years and kill the $\sim$7 km/s relative velocity with hitchhike maneuver to do rendezvous. Furthermore, once capturing

one of the Trojans, it can visit other Trojans in the same group with a trivial ΔV since they have similar orbits. Figure 15 shows an example for an L4 Trojan, 659 Nestor.

A realistic way to achieve Trojan rendezvous with existing technologies would be to use Jupiter gravity assist (JGA) or Earth-Jupiter gravity assist (EJGA), as shown in Figure 16. It takes approximately 10 years to L4 Trojans, with 2.7 km/s ΔV required for rendezvous. To the best of our knowledge, this level of maneuver has not been carried out in deep space using chemical propulsion, although it is not impossible. Rendezvous with L5 Trojans requires relatively small $\sim$1.5 km/s ΔV, but with a longer flight time ($\sim$16 years)

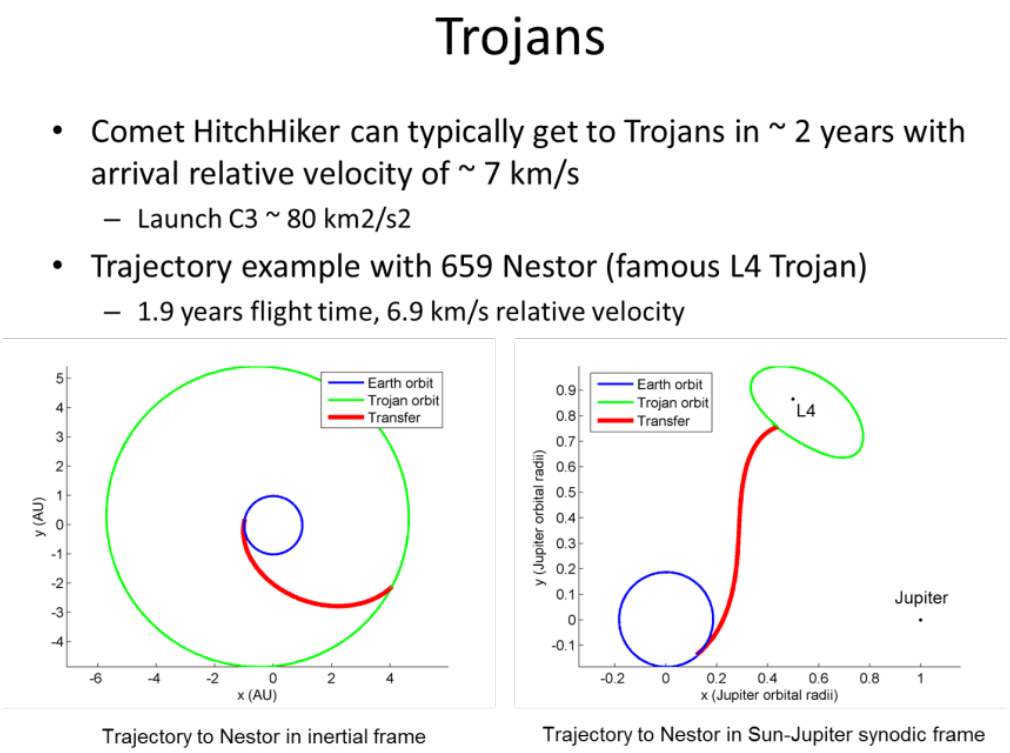

Figure 15: Hitchhiker's trajectory to Jovian Trojans

3.6 Multi-hitchhike tour in the main belt

3.6.1 Science Objective

Asteroid Family Asteroid families are dynamically associated groups of asteroids thought to have been produced by hypervelocity impact destruction of parent bodies [23]. Families are identified by backwards integration of the orbits, showing convergence at some time in the past (which defines the time of breakup). Ages of families range from $<$1Myr to $>$Gyr. Hitchhiker would enable visits to a number of components of a collisionally disrupted asteroid. The science would lie in using the fragments to piece together the original. For example, in a young family, one could use optical and near IR imaging to map structure and composition of the fragments. One aim would be to distinguish pieces of the core from pieces of the mantle of the precursor, to test models of the asteroid disruption process. Gravitational deflection of each fragment (i.e., before or after tether attachment) would give the mass (for big objects, anyway). Images would give the volume. Together, the density is revealed and the density couples with the composition to further characterize the asteroid fragments and the precursor. Asteroid breakup models are very sophisticated. They deserve stronger confrontation with data than has so far been possible.

- Classical chemical propulsion can be used to RDV with Trojans*
  - Gravity assist of Jupiter (and possibly Earth to reduce launch C3)
  - Flight time ~10 years (L4 Trojans), ~16 years (L5 Trojans)
  - DV ~2.7 km/s (L4 Trojans), ~1.5 km/s (L5 Trojans)

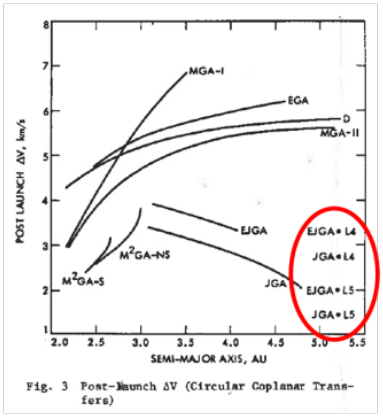

Fig. 3 Post-Launch ΔV (Circular Coplanar Transfers)

* From Chen-wan L. Yen, "Main-Belt Asteroid Exploration: Mission Options for the 1990s", AIAA-82-1463, AIAA/AAS Astrodynamics Conference, San Diego, CA, 1982

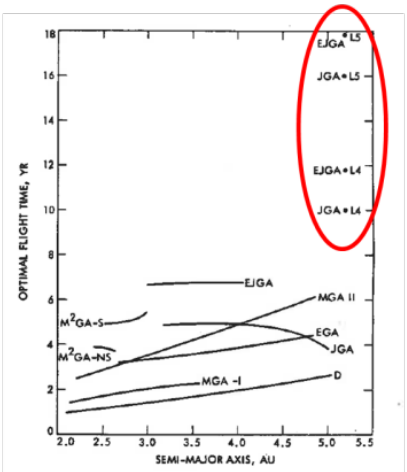

Fig. 4 Optimal Transfer Times (Circular Coplanar Transfers)

Figure 16: Trajectory to Jovian Trojans using chemical propulsion

Active Asteroids Several interesting groups of asteroids have been identified based on their physical (as opposed to dynamical) properties. Notably, the Active Asteroids (=Main-Belt Comets) are objects in the main asteroid belt which share the dynamical character of asteroids with the physical appearances of comet [15, 16]. They eject dust like comets, some of them because they unexpectedly contain ice. Science significance is that they are potential or likely sources for terrestrial planet volatiles, including the Earth's oceans. An interesting multi-object mission would be to visit a set of Active Asteroids. Science aim would be to characterize their surfaces and identify the source of activity. Cameras would provide high res mapping in optical and IR. Value of a multi-mission is to study them as a group, instead of one-by-one, as so to more quickly gain a proper view of them. Another, smaller, set of asteroids show spectroscopic evidence for surface ice (Themis and Cybele are best examples, Themis is the archetype of a 2 Gyr old family). Another interesting class of asteroids are ice-coated ones. There are many unanswered questions: Is it really ice? Where is it (poles vs equator vs crater floors etc). What kind of ice is it? Where's it from? In-situ analysis of multiple objects by a hitchhiker will enable to answer these fundamental questions.

3.6.2 Trajectory Analysis

The previous mission concepts of Comet Hitchhiker involve a rendezvous with a single object, such as an asteroid. The next logical step of analysis would be to visit multiple main belt asteroids by repeating tether hitchhikes. In fact, a main belt asteroid tour requires extremely high velocity change over the mission lifetime, which would pose major propellant mass challenges for conventional propulsion systems. For instance, the Dawn mission will only visit two main belt asteroids, Vesta and Ceres, despite using highly efficient electric propulsion engines. On the other hand, Comet Hitchhiker is propellant-less, so the limit to mission duration and the number of asteroids studied is only determined by the reliability of the spacecraft and the tether. In particular, particular attention should be given to the amount of micrometeoroids in specific regions of the asteroid belt that could damage or cut the tether.

As described in Section 3.6.1, a scientifically attractive multi-asteroid tour scenario would be to visit numerous members of a main belt asteroid family. In this report, we consider the Themis family as the reference target because it is one of the major dynamical families of asteroids: it contains more than 500 member s with relatively low orbital plane inclinations (which facilitates the transfers between them), and is of significant scientific interest [6]. Within the Themis family, a subset of 8 asteroids (corresponding to the largest and earliest-discovered members) is selected to

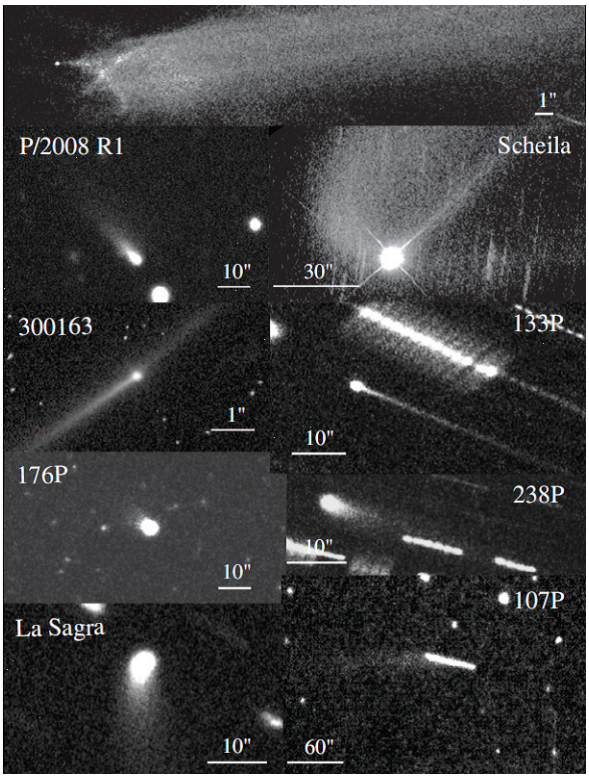

Figure 17: Active asteroids [15]

generate a tour. This early pruning makes the tour design the more tractable with the limited resources of a NIAC Phase 1 study. In addition, to further simplify the problem, only the inter-asteroid segments of the trajectory are considered. We assume that another propulsion system is used from launch to the first asteroid rendezvous.

Table 3 gives the orbital characteristics of the Themis asteroids selected for the mission. As expected, they have very similar semi-major axes, eccentricities, and inclinations.

The mission design goal is to select an asteroid itinerary such that all the asteroids of Table 3 can be visited given ΔV and mission duration constraints. This problem bears similarity to the famous traveling salesman problem (TSP), in which the goal is to find the shortest possible route that visits completely a set of N cities. In the case of our asteroid tour problem, the list of asteroids to visit must be ordered such that the flight time of the mission is minimized. However, finding such a good asteroid itinerary is an extremely challenging combinatorial problem. Exhaustively sampling all possible asteroid ordered sets yields 40320 permutations, which is a large number to sample. This huge search space must also include all the possible time variations within a given sequence.

The solution methodology to generate feasible asteroid itineraries is described herein. The general approach is to consider all asteroid-asteroid segments independently. First, for each asteroid-asteroid pair, a grid of times is formed by varying, at a scan resolution of 30 days, the initial time at the first asteroid between 2035 and 2070 and the flight time between asteroids between 1 and 5 years. The corresponding grid of transfer points is shown in Figure 18.

Each grid point is associated with a unique combination of initial time and flight time, therefore the grid offers all possible transfer trajectories for a given asteroid-asteroid pair. The impulsive transfers for each point on the grid are computed using a simple Lambert targeting algorithm. The mass of the asteroids are assumed negligible. The Lambert fits provide the incoming and outgoing velocities at the asteroids, which can be converted into DVs from the asteroid velocities. Only feasible transfers are stored based on a given maximum tether ΔV capability, which can result in a dramatic filtering of the search space. To focus on near-term applications, an upper bound ΔV of 1.6 km/s is chosen (within the capability of Kevlar materials, see Section 2.2).

A tree search is then performed based on the database of acceptable transfers to combine impulsive arcs and form a feasible end-to-end trajectory (see Figure 19). To allow enough time for performing science activities, a 55-day minimum stay time constraint is enforced at each visited asteroid.

Table 3: Themis family members considered for the multi-hitchhike tour

Asteroid	Semi-major axis (AU)	Eccentricity	Inclination (deg)
24 Themis	3.135	0.126	0.752
62 Erato	3.128	0.171	2.230
90 Antiope	3.151	0.165	2.207
104 Klymene	3.149	0.156	2.789
171 Ophelia	3.129	0.132	2.547
468 Lina	3.132	0.198	0.437
526 Jena	3.120	0.135	2.173
846 Lipperta	3.127	0.183	0.264

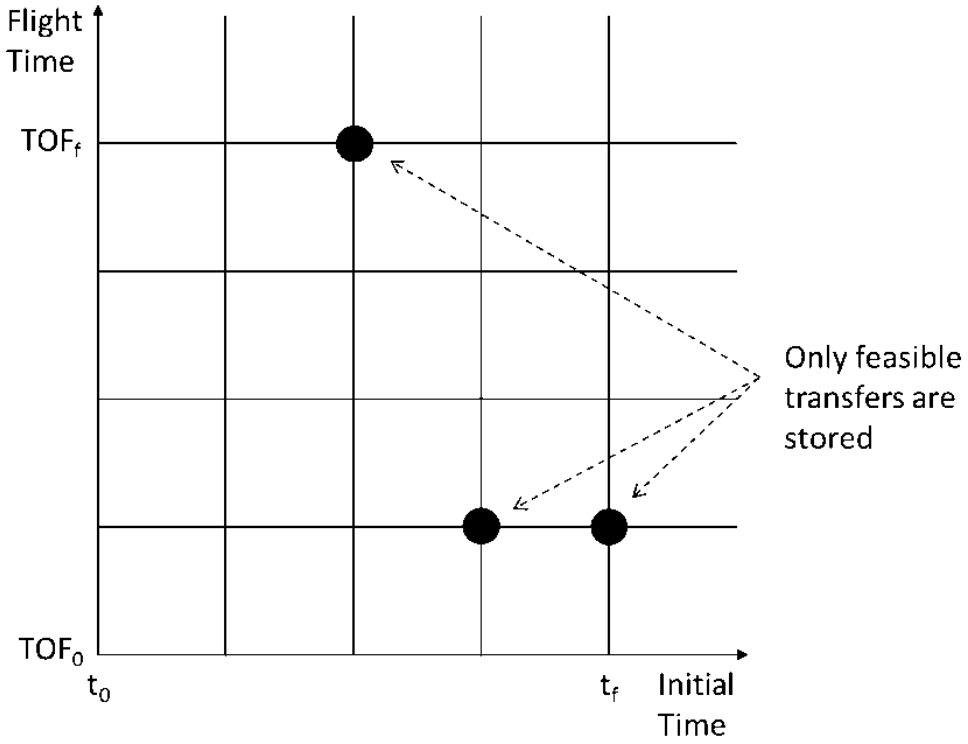

Figure 18: Asteroid-asteroid transfer grid points

This algorithm produced a feasible solution visiting all 8 major members of the Themis, with a total flight time of approximately 34 years and a total required ΔV of 20 km/s. Note that solutions with shorter flight times are expected if flybys of smaller members of the family are exploited, since these extra flybys could also produce significant ΔV maneuvers using the same Comet Hitchhiker technique. Table 4 presents the main characteristics of the feasible multi-hitchhike Themis tour, including departure dates, flight times, stay times, and maneuver magnitudes for each segment of the mission. The corresponding trajectory is shown in Figure 20.

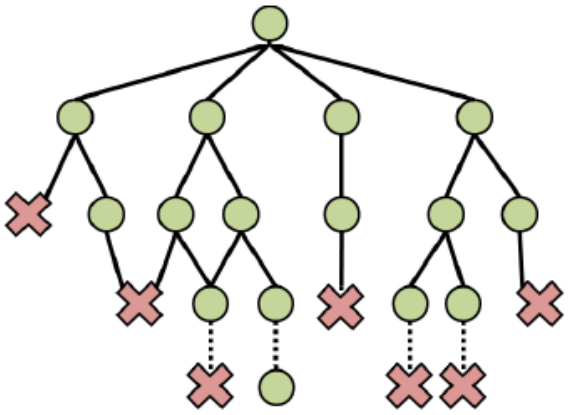

Figure 19: Tree search example: green circles are target asteroids, and red crosses mean no more feasible transfer arcs can be found.

Table 4: Characteristics of the multi-hitchhike Themis tour

Segment	Dep. Date	TOF (years)	Stay time (days)	ΔV_{dep} (km/s)	ΔV_{arr} (km/s)
Ophelia to Klymene	06/03/2036	3.45	456.25	1.56	1.57
Klymene to Erato	02/13/2041	4.40	54.75	1.56	1.60
Erato to Lipperta	08/31/2045	4.90	430.70	0.87	1.60
Lipperta to Lina	09/28/2051	4.95	65.70	1.16	1.60
Lina to Jena	11/13/2056	4.30	87.6	1.48	1.49
Jena to Themis	05/28/2061	2.00	846.80	1.53	1.06
Themis to Antiope	09/21/2065	4.64	N/A	1.53	1.60

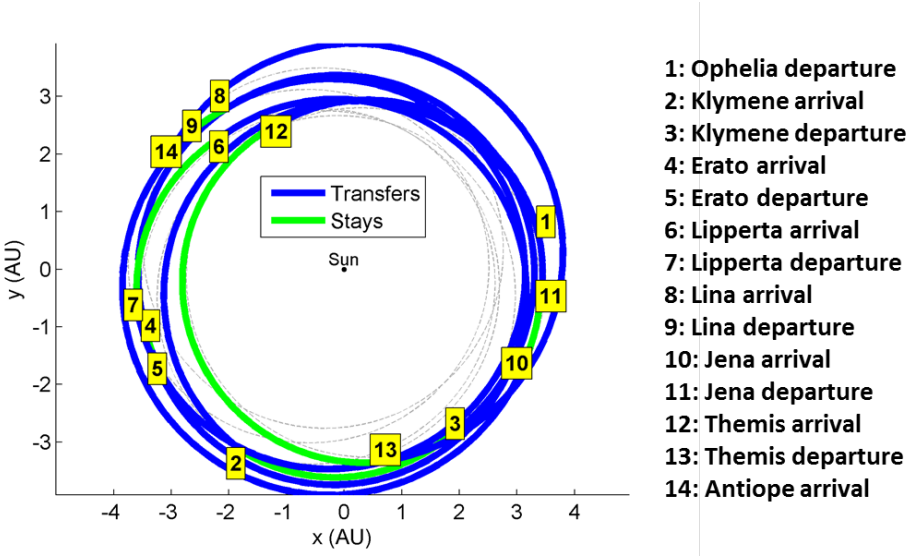

Figure 20: Trajectory and events of the multi-hitchhike Themis tour.

4 Tether Dynamics

The idea of using tether is, of course, not new. In fact, there have been over 17 flights of tether experiments in space, as summarized in Figure 21, which demonstrated the benefit and feasibility of the space tether concept. For example, the YES-2 experiment performed in 2007 successfully deployed 31.7 km of tether in space [17]. However, the usage of tether by the Comet Hitchhiker concept is very different from these missions in that it is highly dynamic. A tether needs to be deployed in a controlled fashion at the relative velocity between the target and the spacecraft. Such a highly dynamic nature poses unique technical challenges. In particular, the tension required for tether deployment increases quadratically with the deployment speed. The propagation of the jerk produced by the impact of harpoon is another issue. In this section, we assess the feasibility of tether both analytically and numerically in consideration of high-speed tether dynamics.

Year	Mission	Type	Description	What was demonstrated
1966	**Gemini-11**	Dynamics	• 15-m tether between capsules • Tethered capsules set in rotation	+ Successful deployment and stable rotation
1966	**Gemini-12**	Dynamics	• 30-m tether between capsules • Tethered capsules set in rotation	+ Successful deployment and stable rotation
1989	**OEDIPUS-A**	ED/Plasma Physics	• Sounding rocket experiment • 958-m conducting tether, spinning	+ Successfully demonstrated strong EM coupling between the ends of conducting tether through tether-guided wave modes + Obtained data on behavior of tethered system as large double electrostatic probe
1992	**TSS-1**	ED/Plasma Physics	• 20-km insulated conducting tether to study plasma-electrodynamic processes and tether orbital dynamics	– Too-long bolt added without proper review caused jam in tether deployer + Demonstrated stable dynamics of short tethered system + Demonstrated controlled retrieval of tether
1993	**SEDS-1**	Momentum Exchange	• Deployed payload on 20-km nonconducting tether and released it into suborbital trajectory	+ Demonstrated successful, stable deployment of tether + Demonstrated deorbit of payload
1993	**PMG**	ED	• 500-m insulated conducting tether • Hollow cathode contactors at both ends	+ Demonstrated ED boost and generator mode operation • Did **not** measure thrust
1994	**SEDS-2**	Dynamics	• Deployed 20-km tether to study dynamics and survivability	+ Demonstrated successful, controlled deployment of tether with minimal swing
1995	**OEDIPUS-C**	ED/Plasma Physics	• Sounding rocket experiment • 1174-m conducting tether, spinning	+ Successfully obtained data on plane and sheath waves in ionospheric plasma
1996	**TSS-1R**	ED/Plasma Physics	• 20-km insulated conducting tether to study plasma-electrodynamic processes and tether orbital dynamics	+ Demonstrated electrodynamic efficiency exceeding existing theories + Demonstrated ampere-level current – Flaw in insulation allowed high-voltage arc to cut tether • Tether was not tested prior to flight
1996	**TiPS**	Dynamics	• Deployed 4-km nonconducting tether to study dynamics and survivability	+ Successful deployment + Tether survived over 10 years on orbit
1999	**ATEx**	Dynamics	• Tape tether deployed with pinch rollers	– "Pushing on a rope" deployment method resulted in unexpected dynamics, experiment terminated early
2000	**Picosats 21/23**	Formation	• 2 picosats connected by 30-m tether	+ Demonstrated tethered formation flight
2001	**Picosats 7/8**	Formation	• 2 picosats connected by 30-m tether	+ Demonstrated tethered formation flight
2002	**MEPSI-1**	Formation	• 2 picosats connected by 50-ft tether • Deployed from Shuttle	+ Tethered formation flight
2006	**MEPSI-2**	Formation	• 2 picosats connected by 15-m tether • Deployed from Shuttle	+ Tethered formation flight of nanosats with propulsion and control wheels
2009	**AeroCube-3**	Formation	• 2 picosats connected by 61-m tether • Deployed from Minotaur on TacSat-3 launch	+ Tethered formation flight with tether reel and tether cutter
2007	**MAST**	Dynamics	• 3 tethered picosats to study tether survivability in orbital debris environment	– Problem with release mechanism resulted in minimal tether deployment; + Obtained data on tethered satellite dynamics
2007	**YES-2**	Momentum Exchange	• Deployed payload on 30-km nonconducting tether and released it into suborbital trajectory	+ Tether did deploy, but: – Controlling computer experienced resets during tether deployment, preventing proper control of tether deployment
2010	**T-REX**	ED/Plasma Physics	• Sounding rocket experiment • 300-m bare tape tether	+ Successfully deployment of tape and fast ignition of hollow cathode

Figure 21: Past tether flights.

4.1 Space Hitchhike Equation (SHE)

4.1.1 Overview

The tension of the tether plays two roles: accelerating S/C, and accelerating the tether itself. Hence,

(Total tension) = (Tension to accelerate S/C) + (Tension to deploy tether).

As for the left hand side, the maximum total tension that a tether can tolerate is constant. As for the second term of the right hand side, the tension required to deploy the tether is given by $\frac{dm}{dt}v$, where $m(t)$ is the mass of tether that has been deployed at t and v is the velocity of tether deployment. Intuitively, $\frac{dm}{dt}$ represents the mass of the tether that needs to be accelerated for a unit time period, and v represents the magnitude of the velocity change of the tether. In our case, the tension that is used to accelerate the tether decrease over time, since both $\frac{dm}{dt}$ and v decreases over time. Therefore, the tension that can be used for accelerating the spacecraft increases over time. As a result, **in order to maximize the ΔV with a given tensile strength of a tether, a hitchhiker should increase the acceleration over time.** Thus, to achieve the maximum, the S/C must be equipped with a tether control device (i.e., brake) that can control the tension. Existing brake mechanisms, such as linear Eddie current brake, can control the brake force.

In the following subsections, we first analytically derive SHE with explicitly considering the tension required for tether acceleration into account. We then use the equation to estimate the required mechanical property of the tether to achieve the level of delta-V required for the missions described in Section 3. We also use SHE to obtain the optimal acceleration profile.

4.1.2 Derivation of the Space Hitchhike Equation

As shown in Figure 22, we assume a hitchhike maneuver where the spacecraft travels at a relative velocity V at the beginning, and completely kills the relative velocity at the end of the maneuver. Let v and m be the relative velocity and the mass of spacecraft. The latter include the mass of undeployed tether. Hence, both v and m decreases over time since the S/C decelerates as deploying the tether. Let σ, ρ, and A be the tensile strength, density, and the section area of the tether, which are assumed to be uniform. The tethers tension is maximum at the attachment to the target body. We denote this tension by T.

As we discussed, the tension of the tether is the sum of the tension required to accelerate the S/C and the tension required to accelerate the tether. Therefore,

$$-\frac{dv}{dt}m-\frac{dm}{dt}v=T. \tag{1}$$

The spacecraft deploys the tether at the speed of v. Therefore, the rate of change of the S/Cs mass is given by:

$$\frac{dm}{dt}=-A\rho v. \tag{2}$$

The upper bound of the tolerable tension is given by the tensile strength of the material of the tether:

$$T=A\sigma. \tag{3}$$

By substituting (2) and (3) to (1), we get

$$\frac{dv}{dt}=-\frac{A}{m}(\sigma-\rho v^2). \tag{4}$$

Eliminate t by dividing (4) by (2):

$$\frac{dv}{dm}=\frac{1}{\rho mv}(\sigma-\rho v^2) \tag{5}$$

This ordinary differential equation is separable as follows:

$$\frac{2v}{(\sigma/\rho)-v^2}dv=2\frac{dm}{m}. \tag{6}$$

This can be solved as follows:

$$-\log\left(\frac{\sigma}{\rho}-v^2\right)=\log m^2+C, \tag{7}$$

where C is a constant. By substituting the terminal conditions, $v_0=0$ and $m=m_0$, we obtain:

$$C=-\log m_0^2-\log\left(\frac{\sigma}{\rho}\right). \tag{8}$$

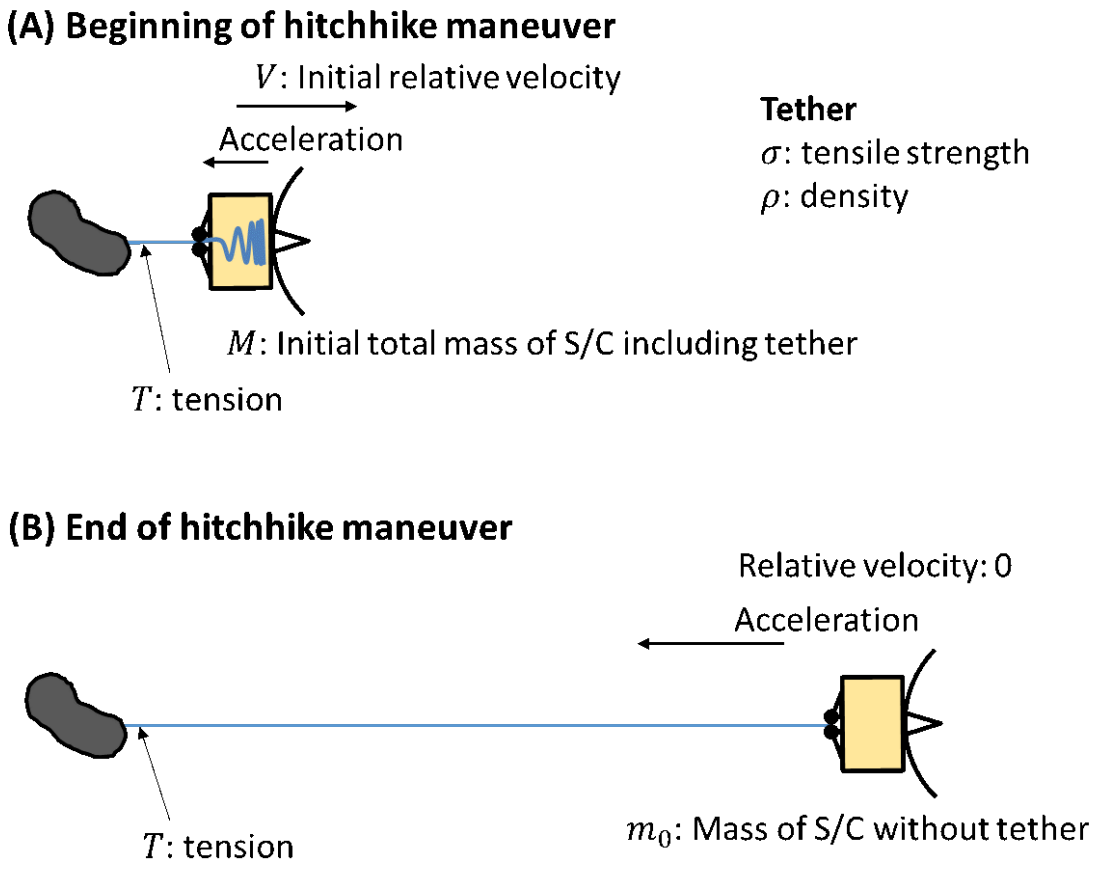

Figure 22: The hitchhike maneuver assumed to derive the Space Hitchhike Equation

Finally, by eliminating C in the general solution (7) by (8), we obtain the following:

$$1 - \frac{\rho}{\sigma} v^2 = \left(\frac{m_0}{m}\right)^2. \tag{9}$$

By solving (9) for v and replace m with M, the initial total mass of spacecraft, we obtain the following Space Hitchhike Equation that gives the upper bound on the ΔV:

Space Hitchhike Equation (SHE)

$$\Delta V = \sqrt{\frac{\sigma}{\rho}\left\{1 - \left(\frac{m_0}{M}\right)^2\right\}} \tag{10}$$

In the above equation, σ/ρ (tensile strength divided by density) is called the *specific strength* of a material. m_0/M is the ratio between the spacecraft mass before and after the hitchhike maneuver, which is simply called the *mass ratio*. SHE relates specific strength, mass ratio, and ΔV, just like the Tsiolkovsky rocket equation relates specific impulse, mass ratio, and ΔV.

4.1.3 Interpretation of the Space Hitchhike Equation

While hitchhike maneuver does not require propellant, it requires tether, which occupies a certain portion of the total mass of the S/C. The more tether the S/C has, the more ΔV it can achieve. Therefore, the tether of a hitchhiker is

analogous to the propellant of a chemical rocket, except that it can be used multiple times.

Figure 23 plots the mass ratio, M/m_0, against ΔV for hitchhikers with different tether materials as well as for a conventional propulsion with 300 sec ISP. Intuitively, M/m_0 is the "wet mass" of the spacecraft (i.e., mass including tether or propellant) that is required to provide a given ΔV to a unit mass of payload.

The shape of the curve is very different between hitchhike and conventional propulsion. As is well known, for conventional propulsion, the mass ratio grows exponentially with ΔV. In theory, it can achieve any ΔV. However, in practice, the exponential growth in the mass ratio makes it impractical to perform a large ΔV maneuver. On the other hand, the curve of a hitchhiker has a mirrored "L shape. There is an absolute upper bound on ΔV, meaning that no matter how large the mass ratio is, there is an upper limit on ΔV that cannot be exceeded. The limit is shown in the vertical dashed lines in Figure 23. However, the growth of the mass ratio is slow except for the proximity of the upper bound.

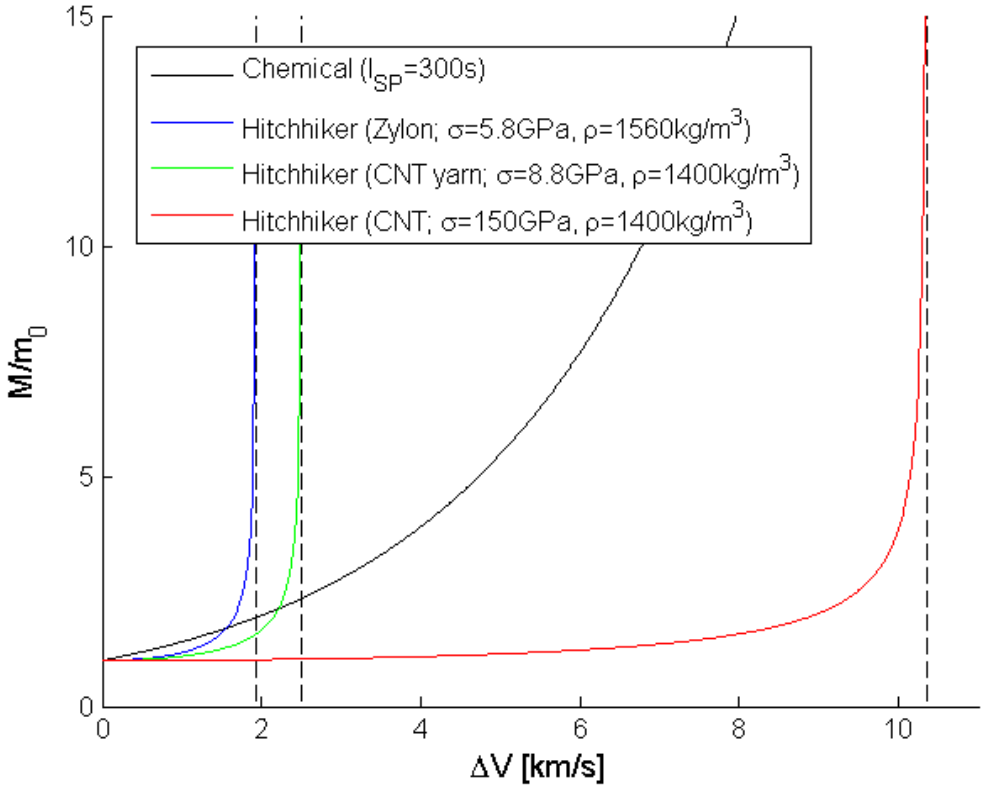

Figure 23: Required mass ratio to achieve a given ΔV.

4.2 Tether Deployment

Two concerns when deploying a tether at a high velocity are tension and stability. It turns out that **SHE is a sufficient condition for deployment speed in terms of both tension and stability,** as discussed below.

Tension The required tension to pull out a tether at velocity v is $\rho A v^2$, where A is the section area of tether. This tension is included in the derivation of SHE. Therefore, when the initial relative velocity is within the bound given by SHE, the tension does not exceed the tensile strength of tether.

Stability It is known that if a tether is deployed at a speed greater than the speed of sound on the tether (i.e., the transverse wave velocity) the tether dynamics is unstabilized, meaning that the deflection is amplified as tether is

deployed [20]. The speed of sound on tether is $\sqrt{T/A\rho}$, where T is the tension. Since the tension is bounded by σA, the speed of tether deployment must be less than $\sqrt{\sigma/\rho}$. Note that this bound is always greater than the bound given by SHE. Therefore, SHE is a sufficient condition for tether deployment stability.

4.3 Tether Materials

SHE tells that, in order to achieve greater ΔV, we need a tether material that has higher specific strength. Intuitively, a tether should be stronger and lighter.

4.3.1 Flight-Proven Materials: Zylon and Kevlar

Figure 24: Zylon

Among flight proven materials, Zylon (Figure 28) has the strongest specific strength. For example, in the Mars Exploration Rovers mission, a nearly 20-meter-long (65-foot-long) braided Zylon was used as a bridle connecting a parachute and the lander. The blue curve in Figure 23 shows the SHE curve of Zylon. Its upper bound on ΔV is 1.93 km/s. Although it outperforms chemical propulsion when ΔV is less than 1.56 km/s, the advantage is marginal. However, the advantage would become nontrivial when it is used for a multi-hitchhike mission.

Kevlar is also a flight proven material with a very high specific strength, but slightly lower than Zylon.

4.3.2 Carbon Nanotubes

Carbon nanotubes (CNTs) have the largest specific strength among known materials; it was reported that $\sim$150 GPa tensile strength has achieved [7]. This level of tensile strength enables a radical hitchhike maneuver. The red line in Figure 23 is the SHE curve of a CNT fiber. The upper bound on ΔV is 10.4 km/s. It significantly outperforms chemical propulsion for most of the domain belo the bound. Importantly, this domain covers the orbit insertion ΔV for the rendezvous missions to KBOs, ($\sim$10 km/s), Centaurs (7.3 km/s), and Jovian Trojans (7 km/s), as discussed in Section 3. For example, in order to give 7.3 km/s ΔV, the mass ratio required for a hitchhiker is only 1.41, while chemical propulsion requires 12.0.

A present issue of CNTs is that only short fibers are available. Although manufacturing a long CNT fiber is an active area of research, the longest fiber to date is $\sim$50 cm [38], which is insufficient for hitchhikers.

4.3.3 Carbon Nanotube Yarns

Production technology of CNT yarn, a tether made of multitudes of short CNT fibers, is also a very active topic of research. It was reported that up to 1km long CNT yarn has been available [25]. To date, the best tensile strength that

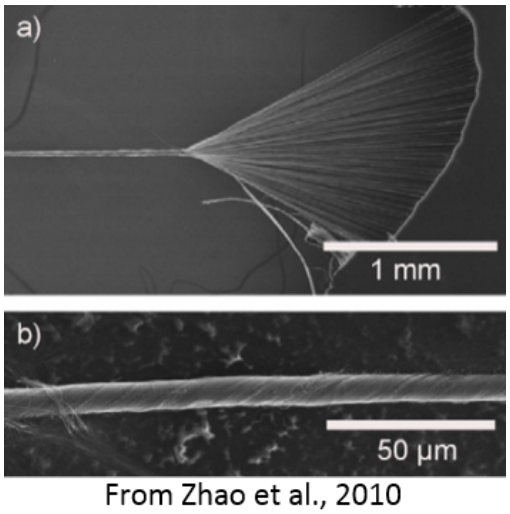

Figure 25: Carbon Nanotube Yarn. Image taken from [39]

has been achieved is 8.8 GPa [4], which has already exceeded Kevlar and Zylon but still far from the strength of fibers.

The green line in Figure 23 is the SHE curve for CNT yarn. Up to 2.51 km/s ΔV is achievable with a hitchhiker with a currently available CNT yarn.

In summary, the utility of the Comet Hitchhiker concept rests upon future development in material. Realizing 100 GPa-level tensile strength would open the door for various exciting science missions by using hitchhikers. Alternatively, by repeating 1-2 km/s hitchhike maneuvers with existing material like Zylon could also give hitchhiker a significant advantage over existing propulsion methods.

4.4 Finite-element Simulation

4.4.1 Modeling Approach

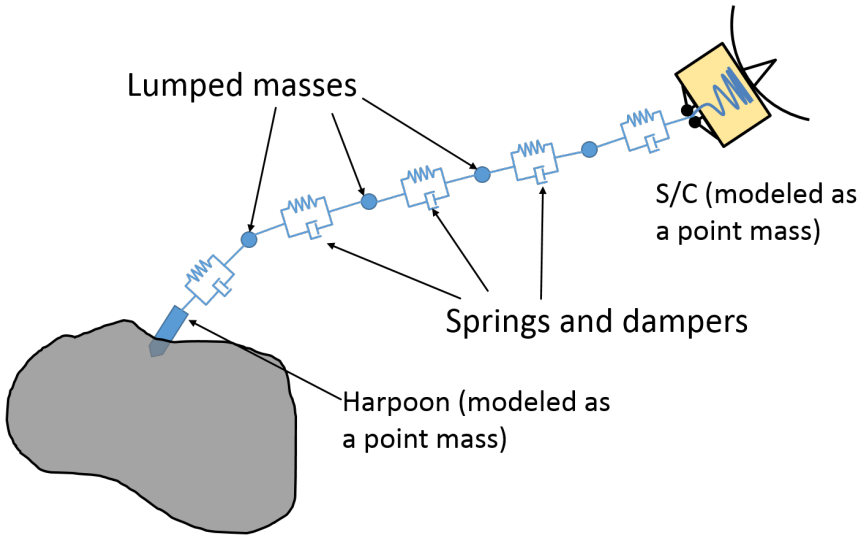

Figure 26: Finite-element model of tether used for simulations

We modeled a tether by a finite number of lumped mass, connected by a chain of springs and dampers, as shown

in Figure 26. The entire system is modeled in 2D by representing the spacecraft and harpoon as two point masses with the following nominal equations of motion:

$$\dot{p}_s = v_s, \tag{11a}$$
$$m_s \dot{v}_s = F_s, \tag{11b}$$
$$\dot{p}_h = v_h, \tag{11c}$$
$$m_h \dot{v}_h = F_h, \tag{11d}$$

where p_s and p_h are the respective positions of the spacecraft and harpoon; v_s and v_h are the respective velocities; m_s and m_h are the respective masses (with any undeployed tether included in m_s); and F_s and F_h are the respective forces acting on the bodies. The comet is assumed to be massive compared to the spacecraft and the harpoon, and it is therefore modeled as a stationary ellipsoidal body.

At the start of each simulation, the spacecraft is initialized some distance away from the comet with a non-zero relative velocity. The harpoon is initially co-located with the spacecraft, but diverges at a rate corresponding to the harpoon ejection velocity. Once contact is made between the harpoon and the comet, the harpoon remains fixed (anchored) for the remainder of the simulation, and the equations of motion are simply

$$\dot{p}_h = 0, \tag{12a}$$
$$m_h \dot{v}_h = 0. \tag{12b}$$

Tether Modeling The forces F_s and F_h in (11) arise solely due to tether interaction between the spacecraft and the harpoon. We model the tether itself by a sequence of n point masses connected to each other, as well as to the spacecraft and the harpoon, by linear spring-dampers. For each tether point mass $i \in 1,\ldots,n$, ordered in the direction from the spacecraft to the harpoon, we denote by p_i and v_i the position and velocity of the tether point mass. For notational convenience, we also define $p_0 := p_s$, $v_0 := v_s$, $p_{n+1} := p_h$, and $v_{n+1} := v_h$. We label each tether segment with the index of the inboard body to which it connects; for example, segment 0 is the segment connected to the spacecraft.

Each tether point mass $i \in 1,\ldots,n$, is governed by the following equation of motion:

$$\dot{p}_i = v_i, \tag{13a}$$
$$m_p \dot{v}_i = F_i - F_{i-1}, \tag{13b}$$

where m_p is the mass and F_i is the force excerted on tether point mass i by tether segment i. Accordingly, we can write $F_s = F_0$ and $F_h = -F_n$.

Tether Segments Each tether segment represents a certain length of deployed tether, characterized by a *nominal* or *unsprung* length ℓ_{0i}. The forces produced by the segment are a function of the *strain* and *strain rate* associated with the segment. The strain of segment i is defined as

$$s_i := \frac{\ell_i - \ell_{0i}}{\ell_{0i}}, \tag{14}$$

where $\ell_i = \|p_{i+1} - p_i\|$ is the current length of the tether segment. The strain rate $\dot{s}_i$ is the rate of change in s_i.

The nominal lengths of all tether segments should add up to the total amount of currently deployed tether, which we denote by d_0. In the course of the hitchhiking maneuver, d_0 will increase (as described in detail later on), and to account for this, we also increase the number of tether mass points. In particular, tether segments $1,\ldots,n$ have a fixed nominal length denoted by $\bar{\ell}_0$, whereas segment 0 has a nominal length of $\ell_{00} = d_0 - n\bar{\ell}_0 \geq 0$, so that the sum of all nominal lengths is equal to d_0. Once $\ell_{00} > \bar{\ell}_0$, a new tether point mass is added by splitting segment 0. The position of the new point mass is chosen so that the strain in each new spring segment is equal to that of the original segment, which for practical purposes places it very close to the spacecraft. The velocity of the new point mass is equal to that of the spacecraft.

The mass of each tether point mass corresponds to the mass of a segment of length $\bar{\ell}_0$; that is $m_i = \rho A \bar{\ell}_0$, where ρ is the tether material density and A is the section area.

Tether Forces and Deployment For each tether segment $i \in 1, \ldots, n$, the force F_i is generated by a linear spring-damper model:

$$F_i = e_i T_i, \tag{15a}$$
$$T_i = K s_i + C \dot{s}_i, \tag{15b}$$

where K is a spring constant; C is a damping constant; and $e_i = (p_{i+1} - p_i)/\|p_{i+1} - p_i\|$ is the unit vector pointing from p_i to p_{i+1}.

Tether segment 0 is treated separately because it is connected to the spacecraft, where tension is actively controlled by deploying tether throughout the hitchhiking maneuver. We assume that the tension is controlled in a manner analogous to a fishing reel, which saturates at a certain level of tension. In particular, the amount of deployed tether is held constant as long as the tension felt by the spacecraft is below a certain target tension; above this level, tether is deployed in order to maintain the target level of tension. Accordingly, we model the force and rate of deployment as follows

$$F_0 = e_0 T_0, \tag{16a}$$
$$T_0 = \begin{cases} K s_0 + C \dot{s}_0, & |K s_0 + C \dot{s}_0| \le T_t, \\ T_t, & \text{otherwise}, \end{cases} \tag{16b}$$
$$\dot{d}_0 = \begin{cases} 0, & |K s_0 + C \dot{s}_0| \le T_t, \\ e_0^{\mathsf{T}}(v_1 - v_0), & \text{otherwise}. \end{cases} \tag{16c}$$

where $e_0 = (p_1 - p_0)/\|p_1 - p_0\|$. In words, the segment acts as a fixed-length spring-damper until the tension reaches a certain target level, at which point the tension is maintained at the target level and the rate of tether deployment is equal to the rate at which tether mass point 1 is moving away from the spacecraft.

Target Tension The target tension T_t depends on the phase of the hitchhiking maneuver. During the pre-anchoring phase, before the harpoon has made contact with the comet, $T_t = 0$; that is, the tether is reeled out with no resistance.

During the post-anchoring phase, the aim is to maximize the tension felt by the spacecraft without the total tension anywhere along the line exceeding some limit $T_{\max}$ less than the tensile strength of the material. As discussed in Section 4.1.1, the total tension in the tether material is a combination of the tension felt by the spacecraft and the tension needed to accelerate the tether. Only the former can be directly measured and controlled; hence an estimate of the latter must be formed in order to synthesize an appropriate target tension T_t.

Assuming for the moment that the motion is one-dimensional, we obtain the following requirement from the derivation of SHE:

$$-m_s \dot{v}_s - \dot{m}_s v_s \le T_{\max}. \tag{17}$$

When tension is at the target level, $-m_s \dot{v}_s = T_t$, and hence we obtain the bound $T_t \le T_{\max} + \dot{m}_s v_s$. Also from the derivation of SHE, the rate of change in mass is bounded by $\dot{m}_s \ge -\rho A v_s$, which results in the bound $T_t \le T_{\max} - \rho A v_s^2$.

We extend this bound to the two-dimensional case in a way that is conservative but reduces to the one-dimensional bound for any one-dimensional motion:

$$T_t \le T_{\max} - \rho A \|v_s\|^2. \tag{18}$$

Spring and Damping Constants For a given tether material, the spring constant K, which represents the tether tension due to unit strain, can be computed as $K = A\sigma_y$, where A is the sectional area and σ_y is Young's modulus. The damping constant C is less readily available; in the simulations to be presented below, we have chosen the damping arbitrarily, but we have investigated the sensitivity of the results to changes in damping.

With respect to the spacecraft velocity profile and the amount of deployed tether, the sensitivity to tether damping appears minimal even when varied by several orders of magnitude. The main observable sensitivity is in the tether dynamics, with ripples settling out slower with decreased damping. This, in turn, results in larger peak tensions along the tether line.

Simulation parameters, straight-line maneuver		
	Value	**Unit**
Target		
Center	[0; -30]	km
Semi-axes	[60; 30.1]	km
Spacecraft		
Dry mass	1,000	kg
Initial position	[-100; 0]	km
Initial velocity	[7.32; 0]	km/s
Harpoon		
Mass	10	kg
Ejection velocity	[0; 0]	km/s
Tether		
Young's modulus	500	GPa
Density	1400	kg/m^3
Section area	$7.14 \cdot 10^{-7}$	m^2
Available length	1000	km
Damping constant	0	kNs
Maximum tension ($T_{\max}$)	71.40	kN
Simulation		
Step size	0.01	s

Table 5

4.4.2 Comparison with SHE

The model described above can be exercised for idealized one-dimensional maneuvers and compared to SHE. As an example, consider the case outlined in Table 5, where the spacecraft moves along a straight line and intersects the target body at a relative speed corresponding to the maximum ΔV predicted by SHE. The simulation is run with a maximum tension $T_{\max}$ corresponding to a tensile strength of 100 GPa. The distance $\bar{l}_0$ between tether point masses is set to a large number in order to avoid line dynamics (i.e., the tether consists only of a single segment).

At first glance, we expect this idealized scenario to produce a deceleration to zero relative velocity while using precisely the 1000 km of available tether. In the simulation, however, only 864 km of tether is deployed; in other words, a greater ΔV could have been achieved by using the entire tether. A comparison between SHE and the simulation results, in terms of relative velocity and deployed tether, can be seen in Figure 27.

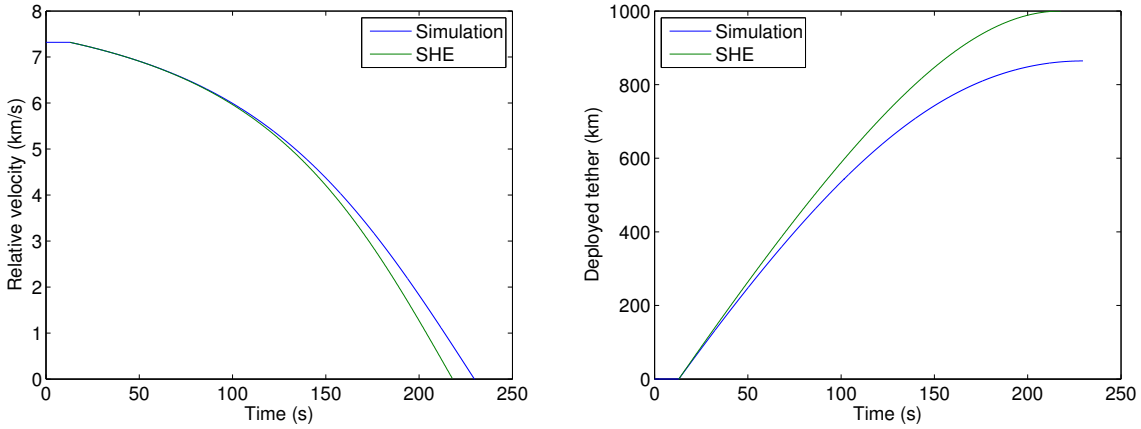

(a) Relative velocity profile

(b) Deployed tether

Figure 27: The plots compare the results of a simulated straight-line maneuver witht those arising from the assumptions made in the derivation of SHE. The left figure shows the relative velocity profile and the right figure shows the amount of deployed tether as a function of time. Owing to the extensibility of the simulated tether, less tether is needed to halt the relative velocity than what is predicted by SHE.

The explanation for this discrepancy lies in the assumption, used in the derivation of SHE, that the rate of tether deployment is equal to the relative velocity of the spacecraft with respect to the comet (reflected in expression for the

rate of mass loss). However, this is only true for a tether that is perfectly stiff; an extensible tether must be deployed at the lower rate needed to maintain approximately constant strain.[6] Consequently, SHE can only be considered an upper bound on ΔV in the limiting case of an inextensible tether. Indeed, as the tether stiffness is increased in the simulation, the result converges to that predicted by SHE.

To appreciate the benefit of tether extensibility, it is informative to consider another limiting case, namely, when the tether is infinitely extensible (i.e., an ideal spring). Assuming for the sake of simplicity that the nominal length is zero, the system can be viewed as a double integrator controlled by a linear control law specifying the tension through the spring and damping constants. It is known that any linear system with no poles in the open right-half complex plane is stabilizable by an arbitrarily bounded input; moreover, for any arbitrarily large region of attraction and any arbitrary limit on the input, a stabilizing linear control law can be designed so as not to exceed the limit on the input [21]. The cost of such a *low-gain* design is a large transient excursion called *slow peaking*. It follows from this consideration that, if the tether is arbitrarily extensible, then by decreasing the Young's modulus, one can achieve an arbitrarily large ΔV irrespective of the tether's tensile strength.

4.4.3 Simulation Results

Simulations were run for a number of different scenarios. In all cases, following harpoon touchdown, ripples can be seen developing along the tether line, the magnitude and settling dynamics depending on the damping parameter. As predicted by the theory, the rate of deceleration is initially slow, while the rate of tether deployment is high; toward the end of the maneuver, this relationship is inverted.

Compared to the one-dimensional case, a penalty is incurred because tether is deployed prior to harpoon touchdown, and because the tether force initially acts almost perpendicular to the relative velocity, only weakly opposing the relative motion. The perpendicular component of the tether force gives rise to a velocity in the same direction, resulting in a curved trajectory and a non-zero terminal velocity.

Two parameterizations are shown in Tables 6 and 7, one in which a 120 km long Zylon tether is used, and another in which a $1,000$ km long CNT tether is used. Results from the Zylon case can be seen in Figure 28. In Figures 28a and 28b, the relative velocity and the amount of deployed tether is compared to SHE. It is seen that, due to the 2D penalty discussed above, more tether than the available 120 km is used; hence, in this case one would have to aim for a smaller ΔV. In Figure 28c the trajectory of the spacecraft is shown, which clearly curves in the direction of the comet (not shown).

Figure 28d indicates the maximum tension at any element along the tether, which should never exceed $T_{\max} = 30.97$ kN. In the simulation, the maximum tension immediately following the release of a new point mass spikes to a very large level; since this is an artifact of the discretization of the tether mass, Figure 28d is generated by measuring the tension only directly prior to the release of a new point mass. According to the figure, the maximum tension is never exceeded; it is prudent, however to treat this result with some caution, due to the artifacts resulting from the mass discretization. It should also be noted that this result is sensitive to the tether damping parameter; for example, with the damping reduced by a factor 10, the maximum tension spikes significantly above the maximum limit.

Results from the CNT case can be seen in Figure 29. In this case, the 2D penalty is small relative to the total tether length. Due to the benefits of tether extensibility, less tether is consumed in this case than what is predicted by SHE. The trajectory exhibits only a shallow curvature, as seen in Figure 29c. Figure 29d shows the maximum tension along the line, which never exceeds the limit of $T_{\max} = 107.1$ kN. The maximum tension is measured in the same way as for the Zylon case and is subject to the same caveats.

[6] According to (16c), the rate of deployment in the simulation is equal to the rate at which the spacecraft is moving away from tether point mass number 1; when the line consists of a single segment, this is equivalent to deploying at a rate equal to the relative velocity of the spacecraft with respect to the comet. However, as soon as the tether becomes too long to produce a tension larger than T_t, the deployment stops and the tension builds back up. As a result, the tension chatters in a very narrow band around T_t and produces the correct rate of deployment over time.

Simulation parameters, Zylon case

	Value	Unit
Target		
Center	[0; -30]	km
Semi-axes	[60; 30.1]	km
Spacecraft		
Dry mass	1,000	kg
Initial position	[-100; 10]	km
Initial velocity	[1.67; 0]	km/s
Harpoon		
Mass	10	kg
Ejection velocity	[0; -2.17]	km/s
Tether		
Young's modulus	270	GPa
Density	1560	kg/m^3
Section area	$5.34 \cdot 10^{-6}$	m^2
Available length	120	km
Damping constant	1,000	kNs
Maximum tension (T_{max})	30.97	kN
Simulation		
Step size	0.01	s
Distance between tether point masses	2	km

Table 6

Simulation parameters, CNT case

	Value	Unit
Target		
Center	[0; -30]	km
Semi-axes	[60; 30.1]	km
Spacecraft		
Dry mass	1,000	kg
Initial position	[-100; 10]	km
Initial velocity	[8.96; 0]	km/s
Harpoon		
Mass	10	kg
Ejection velocity	[0; -1.40]	km/s
Tether		
Young's modulus	500	GPa
Density	1400	kg/m^3
Section area	$7.14 \cdot 10^{-7}$	m^2
Available length	1000	km
Damping constant	100	kNs
Maximum tension (T_{max})	107.1	kN
Simulation		
Step size	0.01	s
Distance between tether point masses	2	km

Table 7

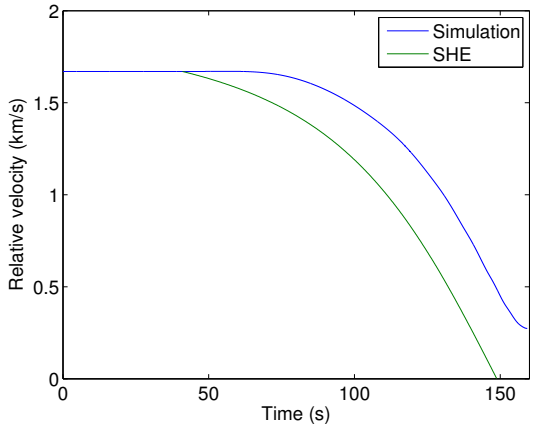

(a) Relative velocity profile

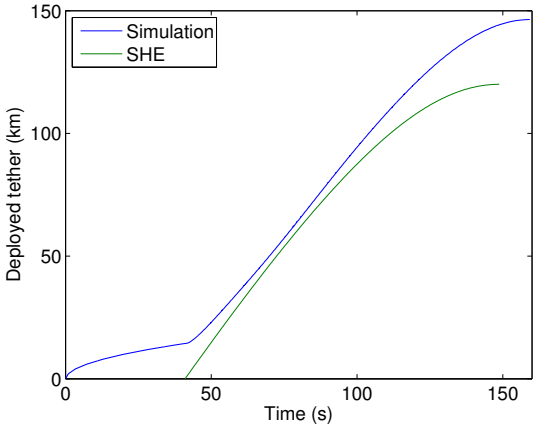

(b) Deployed tether

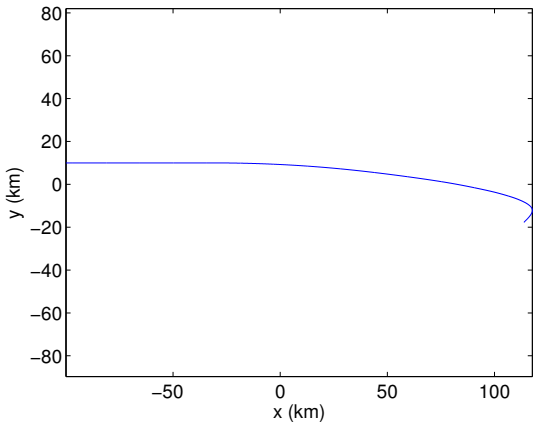

(c) Spacecraft trajectory

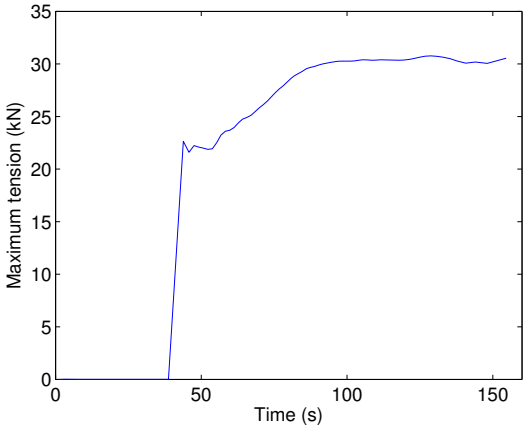

(d) Maximum tension (measured prior to each discrete mass deployment)

Figure 28: The figures show the results from a simulation using a Zylon tether, and compares these to the results predicted by the assumptions made in the derivation of SHE. Owing to the 2D penalty, more than the available tether is needed; hence, one would need to aim for a lower ΔV in this case.

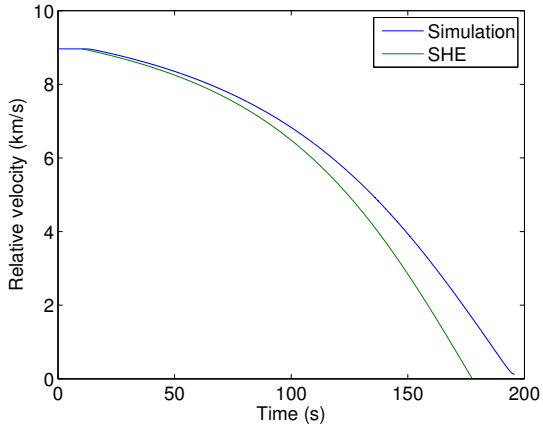

(a) Relative velocity profile

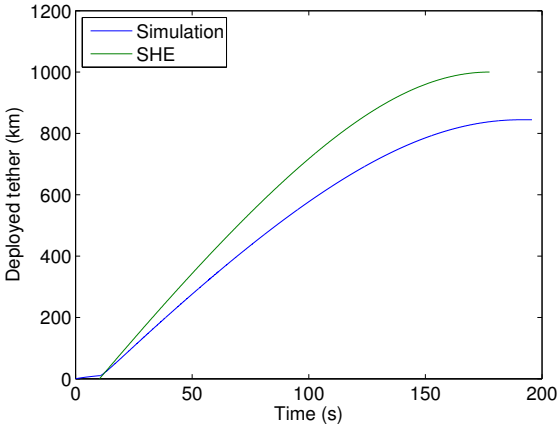

(b) Deployed tether

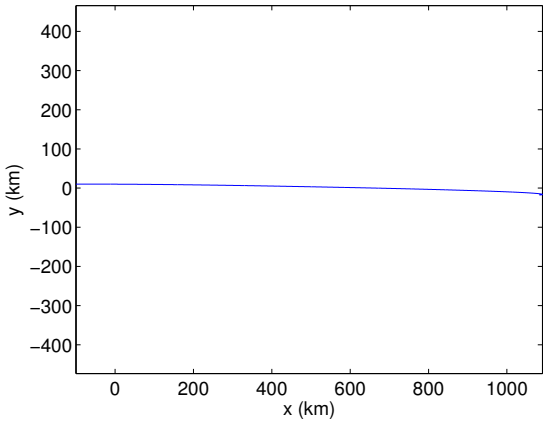

(c) Spacecraft trajectory

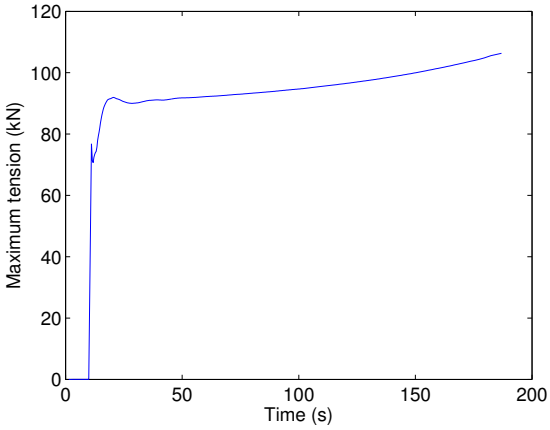

(d) Maximum tension (measured prior to each discrete mass deployment)

Figure 29: The figures show the results from a simulation using a CNT tether, and compares these to the results predicted by the assumptions made in the derivation of SHE. Owing to the benefit of tether extensibiliity and the limited 2D penalty, less tether is needed than what is predicted by SHE.

5 Tether Braking

As discussed in Section 2, the space hitchhiker maneuver requires braking on tether in order to control tension and accelerate/decelerate the spacecraft. However, due to the very high speed of tether (1-10km/s), conventional brake mechanisms would not likely work. In addition, in order to perform the inverse hitchhike maneuver, a hitchhiker must have a capability to accelerate the tether. Therefore, availability of tether braking/acceleration mechanism that can support the speed required to perform hitchhike maneuvers is a key to the feasibility of the Comet Hitchhiker concept.

In this section, we first investigate contactless linear brake/motor mechanisms that can be potentially used for hitchhikers. Then we perform preliminary feasibility analysis in terms of heat dissipation.

5.1 Contactless Brake/Motor Mechanisms

Among various brake/motor mechanisms, linear electromagnetic brakes are the most prospective because it does not require physical contact with tether. There are few variants, which are similar but different in energy dissipation methods.

5.1.1 Linear induction brake/motor

Linear induction motor is an alternating current, asynchronous linear motor, which is widely used in train systems such as John F. Kennedy Airport's AirTrain and Tokyo's Toei Oedo subway line. The motor can also be used as a regenerative brake. In the train application, the secondary is a sheet of metal placed between two rails, in which eddy current is induced.

As shown in Figure 30, in the application for hitchhikers, the motor's secondary is the tether itself that goes through a series of coils. The tether much be conductive. We can use either a conductive material, such as carbon nanotube, or conductive textile, such as Zylon fibers plated with metal.

When used as a brake, the induced eddy current produces magnetic field that counteracts the tether motion, as in Figure 30-(a). The eddy current also produces heat in tether due to the resistance. As a result, the kinetic energy of the spacecraft is turned to heat and electric energy, which can be stored in the spacecraft to be used for the next inverse hitchhike maneuver. When used a a motor, the magnetic field produced by the eddy current accelerates the tether by consuming the stored electric energy.

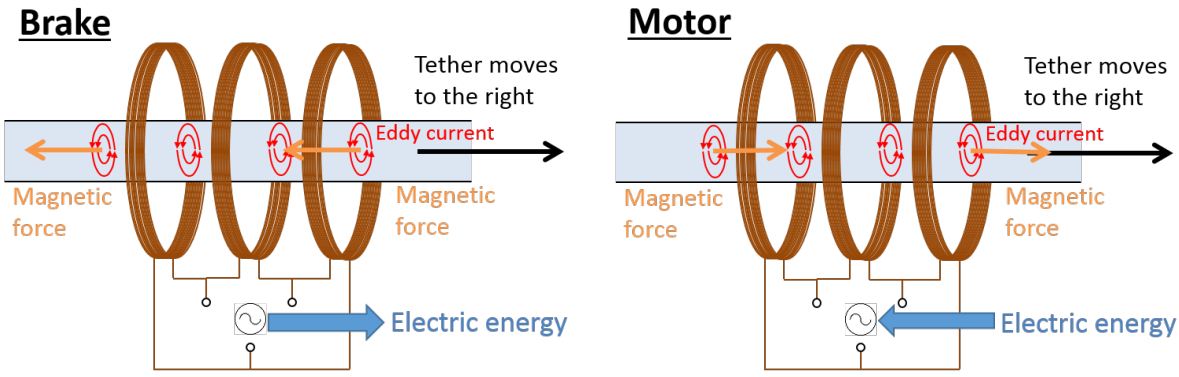

Figure 30: Linear induction brake/motor for Comet Hitchhiker used as (a) brake and (b) motor.

5.1.2 Linear eddy current brake

Linear eddy current brake is similar to linear induction motor/brake but has a simpler mechanism, as shown in Figure 31. A conductive tether goes through DC coils. The coils can be replaced with donut-shaped permanent magnets, but in such a case tether tension cannot be actively controlled. The magnetic field produced by the DC coils induces eddy current in the tether, which counteracts with the ose magnetic field. No electricity is produced in this brake mechanism, hence all the kinetic energy is eventually dissipated as heat in the tether. Importantly, this mechanism cannot be used

as a motor. Hence, it cannot be used for a multi-hitchhike mission which requires inverse hitchhike maneuvers. It's major advantage is the simplicity.

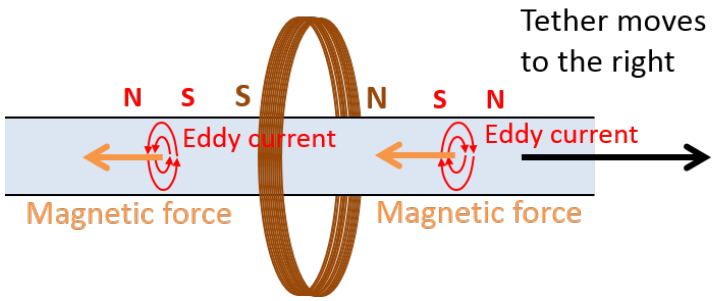

Figure 31: Linear eddy current brake for Comet Hitchhiker

5.1.3 Linear regenerative brake/motor

A slightly more complex mechanism is the linear regenerative brake/motor shown in Figure 32. Non-conducting tether with permanent magnets goes through coils, in which induced electromotive force is produced. An advantage of this mechanism is that no heat is produced in the tether. Furthermore, the same mechanism can be used as a linear motor by injecting electric energy to the coil. A concern is the increase mass of the tether due to the permanent magnets.

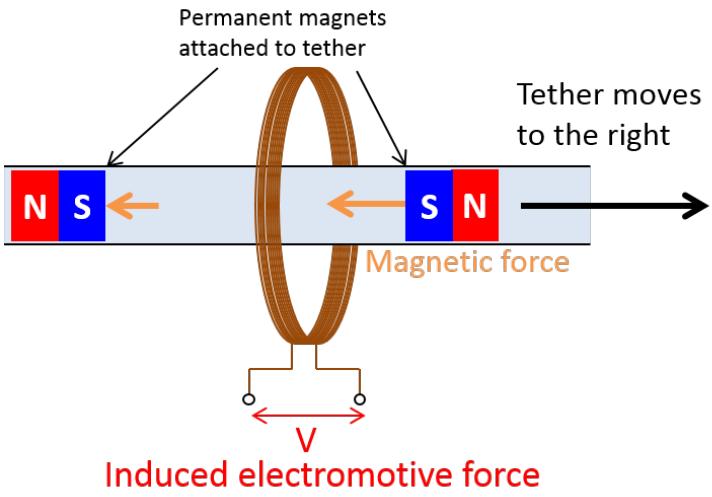

Figure 32: Linear regenerative brake/motor for Comet Hitchhiker

5.2 Heat Dissipation

Heat dissipation is a major technical challenge. We performed preliminary analysis on the temperature increase of tether with following assumptions:

- **Assumption 1**: all the kinetic energy of spacecraft is dissipated as heat only in the tether.
- **Assumption 2**: heat is distributed uniformly through the tether

Assumption 1 is conservative in two aspects. First, in reality, not all the heat goes to the tether; heat in the spacecraft can be dissipated efficiently by radiators, for example. Second, using regenerative brake will significantly reduce

Table 8: Temperature increase of tether due to braking, with assumption that 1) all the kinetic energy of spacecraft is dissipated as heat only in the tether and 2) heat is distributed uniformly. Using regenerative brake will significantly relax the temperature increase.

ΔV [km/s]	Temperature increase [K]	
	CNT	Zylon
1.0	120	420
2.0	470	1700
4.0	1900	6700

the amount of heat produced by braking. On the other hand, Assumption 2 is pessimistic because heat distribution cannot be perfectly uniform. However, this assumption gives a good approximation for materials with a high thermal conductivity such as carbon nanotube.

Let ΔT be the temperature increase of tether, c be the specific heat capacity of tether, m is the mass of the tether, M is the mass of the spacecraft including the tether, and ΔV be the velocity change of the spacecraft. With the above assumptions, ΔT is obtained from the following equation:

$$cm\Delta T = \frac{1}{2}M\Delta V^2.$$

We assume that the mass ratio is 5 i.e., $(M-m)/M = 5$. The specific heat capacity is 5.4 KJ/kgK for CNT [10] and 1.5 KJ/kgK for Zylon [32].

Table 8 summarizes the results. Note that the sublimation temperature is 2900K for CNT[36] and 600K for Zylon [32]. The result suggests that no active heat dissipation is necessary for both materials for a 1 km/s hitchhike, though the initial temperature of Zylon must be relatively low (¡150K), hence it should be thermally isolated from the heat produced by spacecraft bus before deployment. A CNT tether can withstand up to 4 km/s without active heat dissipation. We note that the strength of material often reduces at a high temperature and we do not consider that effect in this analysis.

In order to perform hitchhike above these limits, regenerative braking, active heat dissipation, or both are required. In particular regenerative brake is beneficial because it can reduce the total amount of heat produced and generate electric energy. The electric energy can be stored in a superconducting coil, for example, to be used for the next inverse hitchhike maneuver. Alternatively, it can be used instantly to drive high-power ion thrusters to provide additional acceleration and hence relax tension on tether.

6 Harpoon Impact

We performed an assessment of harpoon survivability using a combination of analytical and numerical techniques. A hydrodynamic 0-D analytical model was first employed to determine the feasibility of the concept. The main findings of this analysis include:

- A projectile made of extremely hard ceramics, such as boron carbide and Y2O3-doped zirconia, or diamond, may be able to tolerate an impact with a planetary body at 10 km/s
- The dominating factor to the survivability is impact velocity and the strength of the projectile, which can be characterized by measurements of the compression state when plastic shocks appear solids, such as the Hugoniot Elastic Limit (HEL). In this analysis, the rigidity of the target surface (e.g., rock, ice, or snow) has marginal influence when the projectile has much larger strength.

The results of the 0-D model were validated via 1-D numerical simulations that included other material parameters of the projectile, such as the shear and elastic moduli. To conclude our investigation, we developed and run 2-D numerical simulations of the projectile-target system on a supercomputer cluster, which allowed us to draw additional conclusions that were beyond the scope of the analytical model:

- Crater diameter, critical for the projectile to work as a harpoon, is dependent on target strength and impact velocity and direction. Oblique impacts (even at small angles) produce devastating craters at high velocities.
- The depth of penetration is not as large as the 0-D model predicts. Factors contributing to it are the elastic properties of the target (for instance, compressibility) and effects that can only captured in a 2-D simulation, such as the radial expansion of the material, which increases the contact area and the total arresting force.

6.1 Problem description

Under certain conditions of impact velocity and material parameters, the distribution of stresses in solid media (both projectile and target) can exceed a threshold value, commonly denominated yield stress. This quantity can be dependent on temperature, loading condition, and rate of loading and determines the inception of a new regime of motion within the material. This new regime is dependent on the crystalline structure of the materials in such a way that some materials, denominated brittle, will fail, while others, the ductile materials, will undergo irreversible plastic deformations that stay in the solid even when the stresses are removed. Experimental evidence suggests that this plastic state is independent of the hydrostatic stress condition in the solid, enabling a “fluid-like” motion. A classical simplified model of this phenomena is the Monroe jet [5], a fluid jet striking a fluid half space. If a projectile is perfectly liquid, it steadily flows away from the leading tip until it becomes entirely absent, leaving a crater on the surface of the target body, as in Figure 33 [12].

However, if the stress condition in some region of the projectile remains below the yield stress, the material here cannot flow and will be continuously decelerated by the pressure exerted by the target in opposition to the projectile motion. In such a situation, the projectile comes to rest before it is all used up [30].

The projectile of a harpoon must survive a hypervelocity impact, meaning that a significant portion of it needs to remain in the elastic regime in order to function as planned. There exist other parameters critical to concept feasibility, such as the crater diameter not being excessively large so the harpoon can attach to the target and the sensitivity to the angle of incidence of the projectile.

To investigate the feasibility of our concept, we first use a 0-D analytical model developed independently by Alekseevskii [1] and Tate [30, 31]. This model is able to predict depth of impact, length of the projectile that is eroded, and the time evolution of the velocity of both tips of the projectile, using simplistic approximations to the material parameters and equations of state (i.e., incompressibility, pure fluid motion in the plastic region) of both projectile and target. A 1-D numerical code was specifically developed to validate the results of the 0-D model and ease the transition to running simulations with a 2-D code. These two numerical algorithms include a more complex description of the material, with equations of state that not only take into account the hydrostatic behavior but also the existence of shear, and additional geometrical parameters such as the aspect ratio of the projectile. In the next paragraphs, we briefly describe the fundamental equations for each model and present the results of our analysis.

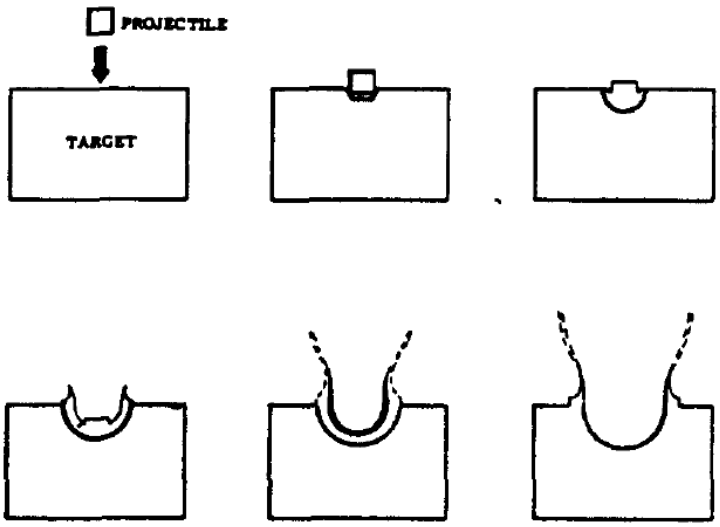

Figure 33: Cratering process of hyper-velocity impact. Image excerpted from [12].

6.2 0-D hydrostatic model for hypervelocity impact

6.2.1 Derivation of the 0-D model

We consider a situation where a projectile, whose original length is L, penetrates into a semi-infinite target with initial velocity V_0, as in Figure 34. We assume that the projectile acts as rigid body until a certain pressure, Y_p, is reached, which is approximated by the Hugoniot Elastic Limit (HEL) of the material. The Hugoniot Elastic Limit is defined as the minimum stress required behind a shock in order to produce permanent deformations in a material. Its relation with the classical static yield stress of the material (i.e., the minimum stress that produces plastic deformations in a classical tension test) depends on the material, with the HEL being typically a few times higher than the static yield stress as materials commonly withstand compression better than tension. In Figure 34, the front part (A-B) of the projectile behaves hydrostatically (i.e., the stress condition can be assimilated to a hydrostatic pressure situation) while the rear part (B-C) remains solid and is modeled as a rigid body since elastic deformations here are much smaller than the plastic deformations in section (A-B). Likewise, the target material behaves as a rigid body below the threshold pressure, R_t. The interface of two materials (A) proceeds through the target material at velocity U, which is slower than V. Taking moving axes through the interface, the two materials can be modeled as colliding flows of incompressible liquid.

The pressure at B is Y_p; as the flow goes from B to A, the velocity falls off as the pressure increases according to Bernoulli's equation until the material comes to rest at the stagnation point. Imposing a boundary condition where pressure and velocity are constant across the material interface, we obtain at A:

$$\frac{1}{2}\rho_t U^2 + R_t = \frac{1}{2}\rho_p (V-U)^2 + Y_p. \tag{19}$$

The remaining length of projectile is from A to C, denoted by l. Thus, the rate of erosion is given by:

$$\frac{dl}{dt} = -(V-U). \tag{20}$$

These two equations already give an important insight about how the projectile of Comet Hitchhiker must be designed. By solving the first equation, a greater Y_p results in greater U relative to V, which means slower rate of erosion. Therefore, we should choose a hard material for the projectile in order to maximize the survivability.

Another important conclusion obtained from these equations is that, since Y_p and R_t are both additive, only their difference, $Y_p - R_t$, matters. Therefore, in a condition where $Y_p \gg R_t$, the rigidness of the target body (i.e., R_t) has only marginal impact on the phenomenon.

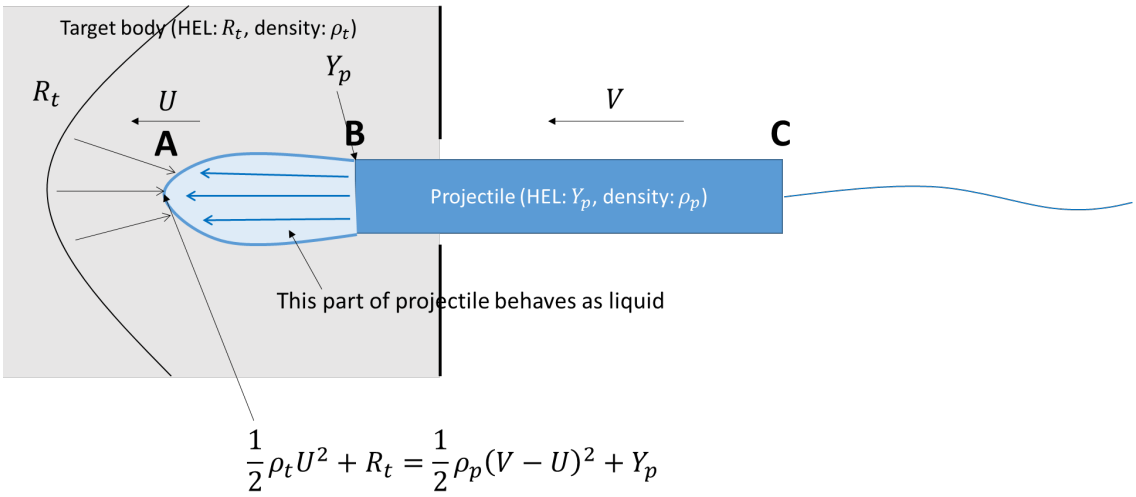

Figure 34: Hydrodynamic model of hypervelocity impact.

The remaining part of the projectile is decelerated by action of the pressure Y_p. Hence, the equation of motion is:

$$Y_p = -\rho_p l \frac{dV}{dt}. \tag{21}$$

If $Y_p > R_t$ (i.e., projectile is harder than the target), the projectile is eventually slowed down to the point where the rate of erosion is zero i.e., $V = U$. The velocity at which erosion stops is given by substituting $V = U$ into 19:

$$V_c = \sqrt{2(Y_p - R_t)/\rho_t} \tag{22}$$

If the initial velocity, V_0, of projectile is less than this critical velocity, V_c, then the entire projectile remains in elastic state after the impact. Let l_s be the length of remaining part of projectile after the impact. According to [30], by solving (19), (20), (21) for l, we get the following relationship:

$$\frac{l_S}{L} = \left[\sqrt{\frac{\frac{A(\mu+1)}{\mu-1}}{V_0 + \sqrt{V_0^2 + A}}}\right]^{\left(\frac{R_t - Y_p}{\mu Y_p}\right)} \exp\left[\frac{\mu\rho_p}{2(1-\mu^2)Y_p} \cdot \left\{V_0\sqrt{V_0^2 + A} - \mu V_0^2\right\}\right], \tag{23}$$

where

$$\mu = \sqrt{\rho_t/\rho_p},\ A = 2\frac{(R_t - Y_p)(1-\mu^2)}{\rho_t}. \tag{24}$$

If $l_s > 0$, the motion after the point in which further plastic deformations disappear can be assimilated to a rigid body of length ls being slowed down from the velocity V_c to a stop by the interfacial pressure $Rt + \rho_t U^2/2$:

$$\rho_p l_s \frac{dU}{dt} = -R_t - \frac{1}{2}\rho_t U^2. \tag{25}$$

The total penetration depth is then given by the evolution of the interfacial velocity U in time:

$$d_p = \int_{t=0}^{t_f} U(t)dt, \tag{26}$$

with t_f such that $U(t_f) = 0$.

6.2.2 0-D model results: uneroded length of projectile

We use the analytical solution above to evaluate the remaining length of projectile at a given velocity. The elastic limit and density of candidate target and projectile materials are given in Table 9 for diamond, zirconia, and tungsten, and in the legend of Figure 35 for other materials.

Figure 35 shows the uneroded length of projectile after impact with very soft soil and very strong rock. Note that, although the compressive strength of very soft soil and very strong rock are ∼10,000 times different, there is no order-of-magnitude difference in the uneroded length. This result is consistent with the discussion in the previous section. In fact, the difference in the two results are mainly due to the difference in the density between soil and rock, not the rigidity.

In both cases, metal materials (steel and tungsten) are completely eroded at 10 km/s impact speed. On the other hand, by using boron carbide and Y2O3-doped zirconia, 16%-27% and 30%-52% of the projectiles remains uneroded, respectively, which would be sufficient to work as a harpoon.

Finally, we can set a best case scenario using the strongest known material, diamond. According to Figure 35, 83%-92% of the strongest, the most beautiful, and possibly the most expensive projectile in the world will survive after a 10 km/s impact. However, such a use of diamond must be made very carefully in order not to bankrupt bridegrooms.

Table 9: Mechanical properties for the materials evaluated with the 0-D, 1-D, and 2-D models

	Projectile			Target	
	Tungsten	Zirconia	Diamond	Hard rock	Soft soil
Density (g/cm3)	19.25	6.05	3.5	2.7	1.8
Bulk modulus (GPa)	310	170	443	31.7	0.066
Shear modulus (GPa)	161	78.84	478	23.85	0.03076
Heat capacity (J/kg/K)	134	280	516	795	835
Elastic limit (GPa)	3.8	39	68	0.1	0.00025

6.3 Numerical Simulations

2-D numerical simulations of hypervelocity impact of rod projectiles were performed using the Adaptive Mesh Refinement Objected-oriented C++ (AMROC) algorithm. This computer code, which has been used at Caltech for over a decade in the simulation of compressible and turbulent fluid flow, has been extended in the last five years with the implementation of solid mechanics capabilities specifically suited for the study of metal-metal ductile impacts at high velocities. The approach followed in this algorithm makes use of a CFD-like fixed Eulerian grid for discretizing the computational domain. The motion of continuous media in this computational domain is captured by the time evolution of tracking functions, denominated level sets, which describe the location of the material boundaries at each time within the fixed computational grid. The Eulerian approach to solid mechanics have advantages with respect to more classical Lagrangian approaches, in which the computational grid moves attached to material particles, in situations where large deformations in the solid materials exist. The grid in the latter approach is progressively being distorted following the motion of particles and in extreme cases can lead to very small time-steps or even the failure of the method due to element inversion. The Eulerian numerical approach followed here does not suffer from mesh entanglement and allows for a straightforward implementation of the Finite Volume Method (FVM). FVM is especially suitable for problems in which discontinuities in the media, such as shocks, exist as its formulation based on the volume integration of the equation of motion in conservative form leads naturally to the Rankine-Hugoniot shock relations. The use of Adaptive Mesh Refinement (AMR), a technique that automatically produces smaller cell sizes in regions of the computational domain where shocks or material interfaces exist, allows for computational savings and high resolution at the time of capturing the sharpness of shocks and the precise motion of the material interfaces. The aforementioned advantages come at the cost of the requirement for special functions for tracking material boundaries and the need to solve an extended system of equations for solids, which accounts for conservation of mass, momentum, energy, and the time evolution of the deformations in the solid, respectively,

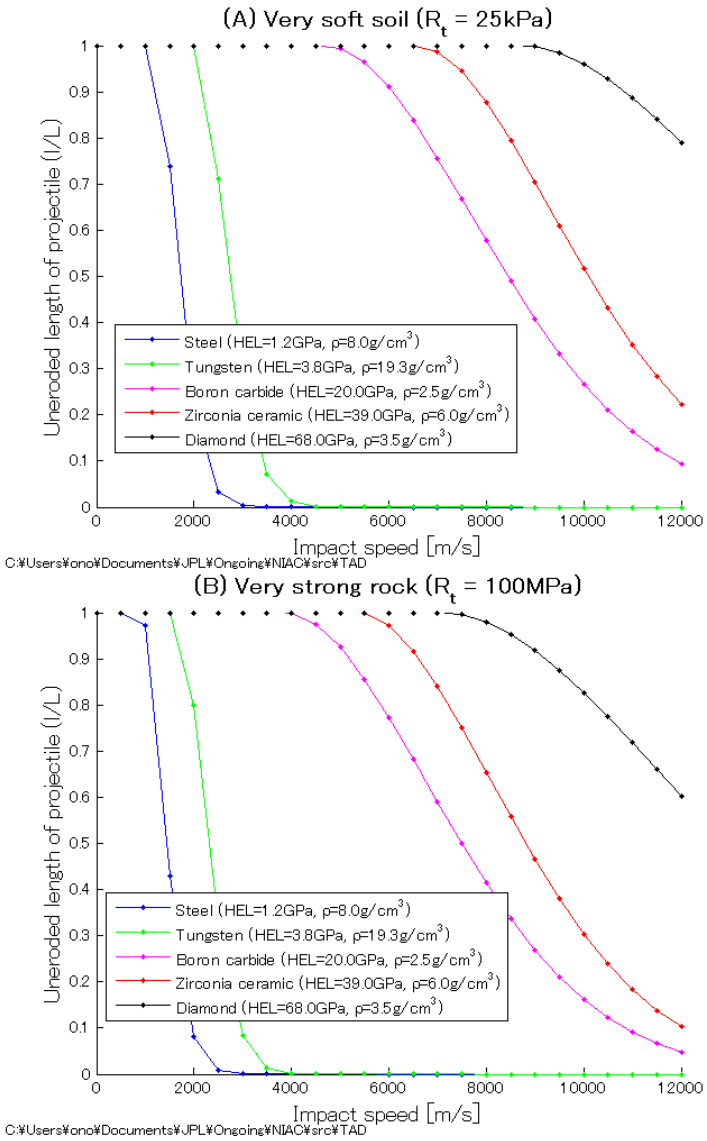

Figure 35: Uneroded length of projectile (l) in relative to the original length (L) after an impact with very soft soil (A) and very strong rock (B). Results are obtained using the 0-D model.

$$
\begin{aligned}
\frac{\partial \rho}{\partial t} + \frac{\partial \rho u_i}{\partial x_i} &= 0 \\
\frac{\partial \rho u_i}{\partial t} + \frac{\partial (\rho u_i u_j - \sigma_{ij})}{\partial x_j} &= 0 \\
\frac{\partial \rho E}{\partial t} + \frac{\partial (\rho E - \sigma_{ij} u_j)}{\partial x_i} &= 0 \\
\frac{\partial g^e_{ij}}{\partial t} + \frac{\partial g^e_{ik} u_k}{\partial x_j} &= u_j \frac{\partial g^e_{ik}}{\partial x_j} - u_k \frac{\partial g^e_{ij}}{\partial x_k} + L^P_{ij},
\end{aligned}
\tag{27}
$$

where t is time, x is coordinate system in the fixed Eulerian frame of reference, ρ is the density, u the velocity field, E the specific total energy taken as the sum of the internal energy, e, and the kinetic energy, $u^2/2$, σ is the Cauchy stress tensor, and g^e is a second order tensor that tracks the deformations in the solid. These deformations are modified

by the plastic update tensor L^p, whose mission is to make the stress state conform to the yield surface determined by the elastic limit. These generalized three-dimensional equations can be simplified for a 2-D case with axial symmetry along one axis. The closure to this system of equations is given by an equation of state, which relates the deformations and entropy with the internal energy:

$$e = e(g^e, s, \lambda), \tag{28}$$

where s in the entropy and λ the parameters that define the mechanical behavior of the material, such as the shear modulus, bulk modulus, and heat capacity. Since a precise characterization of each of the materials tested is not readily available (the code was developed initially for ductile metal materials), we made use of reasonable values for the material properties at nominal conditions of density and temperature (Table 9) and assumed a power-law decrease in the shear and bulk modulus with decreasing density. This assumption is motivated by the fact that the materials lose their resistance to deformations as they become fluid-like and are allowed to flow from the leading tip to the sides of the crater, reducing their density. It can be shown that under the assumption of "hypereleasticity" [22], the Cauchy stresses can be derived from the internal energy using the expression:

$$\sigma_{ij} = -\rho g^e_{ki} \frac{\partial e}{\partial g^e_{ij}}.$$

The above system of equations is hyperbolic in nature and can be solved using the typical upwinding techniques commonly applied in finite volume formulations. It is also necessary to define a plasticity law for modelling inelastic deformations through L^p. For the sake of simplicity and ease of direct comparisons with the 0-D model results, we have employed here a perfect plasticity law in which the yield stress is equal to the Hugoniot Elastic Limit (HEL). Other formulations, which include strain hardening, strain-rate dependency and melting of the material, are available in the code but require characterization of the inelastic deformations in the material (i.e., tests at different strain rates). Even when the material properties used in our simulations are approximate, they represent a large leap forward in the complexity of our model in comparison with the 0-D model, where the materials were characterized solely by their unstressed density and plastic limit.

Boundary conditions at material interfaces are applied using the "ghost solid method". In this approach, a narrow band of computational cells that lie adjacent to the material boundary are flagged as "ghost cells". In each of these cells, a "ghost state" (i.e., fictional values of the properties of the media such as density, velocity, energy, and deformations) is imposed based on the type of boundary (i.e., stress-free boundary vs. contact boundary between two materials) such that when the "real cells" are solved in combination with this band of "ghost cells", the former cells sense the effect of the interface. This technique allows for evolving each material in the computational domain independently within each time-step, as information from the other media is only necessary at the time of setting values to the "ghost cells" before time integration is performed. A more extended description of this method can be found in [24].

6.3.1 1-D simulations

The 1-D algorithm employed in this study is a stripped-down version of the 2-D code described above. This numerical code has been implemented in Matlab for ease of use and debugging. The formulation employed solves the equations of motion described in the above paragraph averaged over the r coordinate, making assumptions on the behavior of stresses and deformations along each section of the projectile. Using this approach, the expressions in (27) are reduced to a system of equations with derivatives in the axial direction of the projectile only (here denoted as z)

$$
\begin{aligned}
\frac{\partial \rho}{\partial t} + \frac{\partial \rho u_z}{\partial z} &= -8\frac{\rho u_r}{D} \\
\frac{\partial \rho u_z}{\partial t} + \frac{\partial (\rho u_z^2 - \sigma_{zz})}{\partial z} &= -8\frac{\rho u_z u_r}{D} \\
\frac{\partial \rho u_r}{\partial t} + \frac{\partial (\rho u_r u_z - \sigma_{zr})}{\partial z} &= -16\frac{\rho u_r^2}{D} - 2\frac{\sigma_{rr}}{D} \\
\frac{\partial \rho E}{\partial t} + \frac{\partial (\rho E - \sigma_{zz} u_z - \sigma_{zr} u_r)}{\partial x_i} &= -8\frac{\rho E u_r}{D} \\
\frac{\partial g^e_{zz}}{\partial t} + \frac{\partial (g^e_{zz} u_z + g^e_{zr} u_r)}{\partial z} &= u_r \frac{\partial g^e_{zr}}{\partial z} + L^P_{zz} \\
\frac{\partial g^e_{zr}}{\partial t} &= -u_z \frac{\partial g^e_{zr}}{\partial z} - 8\frac{g^e_{zr} u_r}{D} + L^P_{zr} \\
\frac{\partial g^e_{rz}}{\partial t} + \frac{\partial (g^e_{rz} u_z + g^e_{rr} u_r)}{\partial z} &= u_r \frac{\partial g^e_{rr}}{\partial z} + L^P_{rz} \\
\frac{\partial g^e_{rr}}{\partial t} &= -u_z \frac{\partial g^e_{rr}}{\partial z} - 8\frac{g^e_{rr} u_r}{D} + L^P_{rr}
\end{aligned} \tag{29}
$$

The influence of the motion in the radial direction, r, is included in the equations through terms that depend on $1/D$, with D the diameter of the projectile. For the simulation of long rods, the terms in $1/D$ are extremely important as they represent the condition that the radial boundary of the rod must be stress-free, which requires the projectile material to expand in the radial direction as it is compressed in the axial direction by the impact.

For simplicity, the target material is not simulated and its presence is accounted for using the stress condition at the material interface used in the 0-D model at the leading tip of the impactor (i.e., $\sigma_{zz} = -R_t - \rho_t U^2/2$). Zero-stress boundary conditions are imposed at the trailing tip. These simulations allow for direct comparison with the 0-D model results of important feasibility constraints, such as depth of impact and length of uneroded projectile.

6.3.2 2-D Simulations

Two-dimensional simulations were run using the Zodiac cluster at JPL. A typical simulation takes 12 to 24 hours to complete when using 48 computational cores, distributed in 4 nodes. The minimum cell size was chosen to be 0.16% of the initial length of the projectile. The use of 2-D simulations enables the analysis of crater depth and effect of the incidence angle and aspect ratio of the projectile. For perpendicular impacts, we use the set of equations (27) with the assumption of cylindrical symmetry along the projectile centerline so only equations with derivative in the axial and radial direction are to be solved. As for oblique impacts, we run simplified cases in which the target and projectile are considered infinite in the third dimension since no axes of symmetry can be found in this configuration. A consistent simulation would require the use of the full set of three-dimensional equations (27). Due to the high computational cost (even at low resolutions) of full 3-D simulations, we decided to run the simplified cases, from where qualitative conclusions can be extracted. 3-D simulations can be considered in future, more detailed, studies.

6.3.3 Simulation campaign

Due to restrictions in the time available and computational resources, a full parametric study, such as the one performed for assessing the length of uneroded projectile with the 0-D model (Figure 35), was not possible. Instead, we chose to simulate a subset of cases that provide useful insight into key parameters: material properties and strength of the projectile and target, velocity of impact, angle of incidence, and aspect ratio of the projectile. We considered tungsten, zirconia, and diamond as possible candidates for the rod projectile, and hard rock and soft soil for the target. Mechanical properties for these materials can be found in Table 9. A summary of the simulation cases and the method employed (0-D,1-D,2-D) is shown in Tables 10-12.

Table 10: Summary of test cases - multiple method comparison and validation ($\alpha = 0$, $L/D = 10$)

		Impact velocity (km/s)	
Projectile	Target	1.5	10
Tungsten	Hard rock	0-D,1-D,2-D	0-D,1-D,2-D
Soft soil	0-D,1-D	0-D,1-D	
Zirconia	Hard rock	0-D,1-D,2-D	0-D,1-D,2-D
Soft soil	0-D,1-D	0-D,1-D	
Diamond	Hard rock	0-D,1-D,2-D	0-D,1-D,2-D
Soft soil	0-D,1-D,2-D	0-D,1-D,2-D	

Table 11: Summary of test cases - 2D-specific simulations (only for Diamond + Hard rock)

		α (deg)		
Impact velocity (km/s)	L/D	0	1	10
1.5	10	x		x
1.5	5	x		
1.5	2.5	x		
10	10	x	x	x

Table 12: Summary of test cases - parametric study of impact velocity

Materials		Impact velocity (km/s)			
Projectile	Target	1.5	5	8	10
Tungsten	Hard rock	2-D	2-D	2-D	2-D
Zirconia	Hard rock	2-D	2-D	2-D	2-D
Diamond	Hard rock	2-D	2-D	2-D	2-D

6.4 Validation and comparison between methods

6.4.1 1.5 km/s impacts

At this relatively low velocity, the stresses generated by the impact are not enough to produce plastic deformations in any of the projectiles. In the 0-D model, the projectile behaves as a rigid body with no erosion. The motion of the impactor is continuously reduced by the opposition exerted by the target, quantified by $R_t + \rho_t U^2/2$. The deceleration is then fast at the beginning, when the interfacial velocity U is high, as decreases with time (see Figure 36). At low enough velocities, R_t will dominate the deceleration of the projectile. Thus, it is expected that the penetration depth in soft soil to be much higher than in hard rock. Table 13 summarizes the results for maximum penetration depth df and time until projectile motion is stopped t_f for the three models. Results with * indicate that the simulation reached its maximum time (10 ms) or the projectile exited the computational domain before the motion was completely stopped. For validation purposes, Figure 36 depicts the evolution in time of the tip velocities V and U, and the penetration depth for each of the cases. It can be observed that since the projectile is in the elastic state, the tip velocities are equal from the beginning of the motion. In the 1-D and 2-D models, small amplitude oscillations of the velocity are due to elastic waves propagating back and forth along the length of the projectile. It is noticed that the time evolution for the 0-D and 1-D models is essentially the same in all the cases shown in Figure 36. 2-D simulations exhibit certain differences that are worth investigating. For hard rock targets, the deceleration of the projectile occurs more sharply once the velocities are relatively low (the simulation for tungsten reached is maximum simulation time before this effect can be noticed). This can be attributed to the target recovering some of its strength (returning to an elastic state) as the stresses decrease at lower interfacial velocities. In this situation of absence of additional plastic deformations in the target, the simplified model $R_t + \rho_t U^2/2$ for the pressure exerted is no longer valid. For instance, the diamond is completely stopped in the 2-D simulation in 4.63ms, while in the 0-D and 1-D models, the motion continues for more than 10 ms. For soft soils with very low strength, this phenomenon can only happen at extremely low interfacial velocities, not captured in the

simulation time. It can be concluded though that the final penetration depth will be somewhat smaller than what is predicted by the 0-D model.

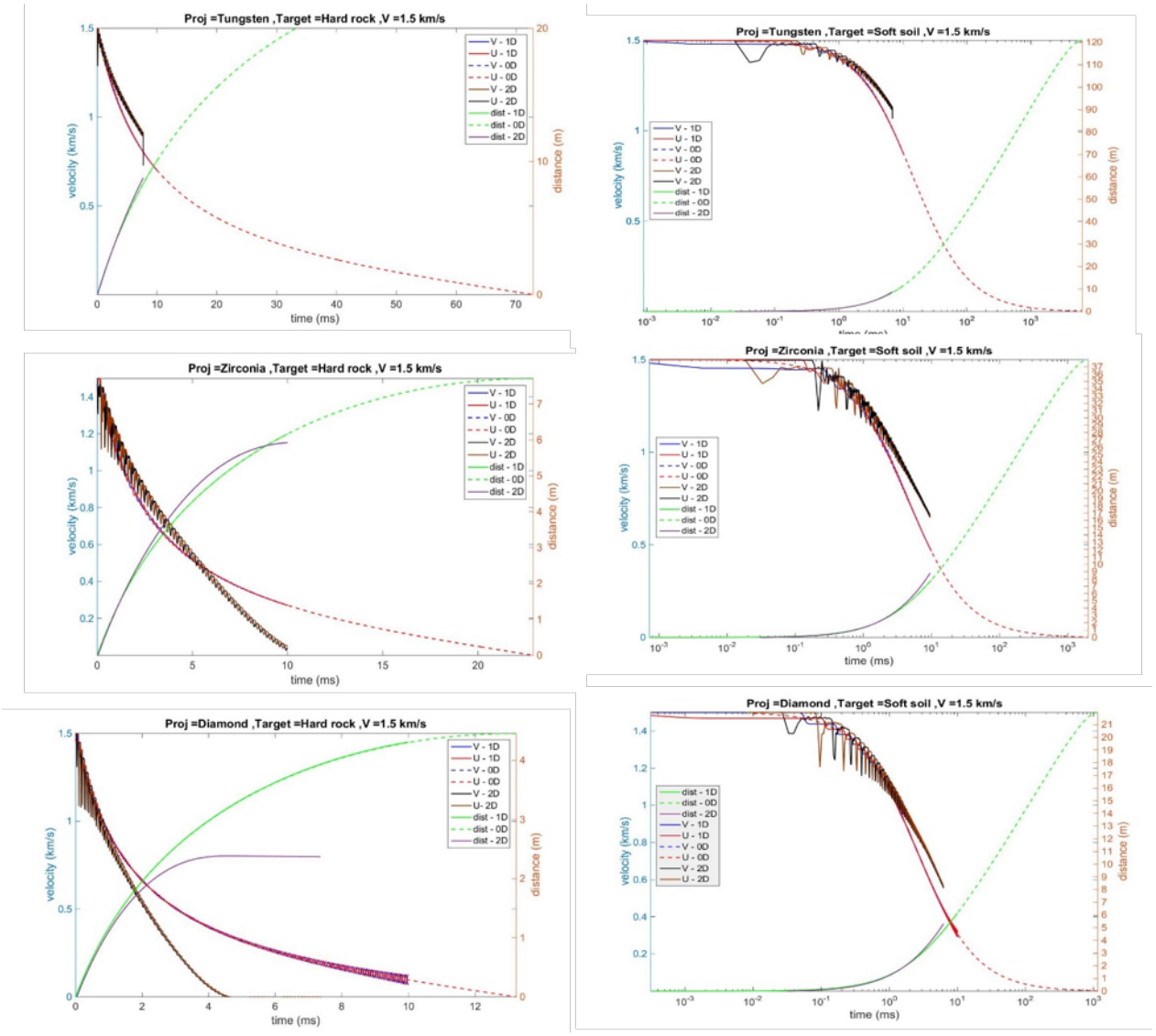

Figure 36: Time evolution of leading tip velocity (U), trailing tip velocity (V), and penetration depth as a function of time for different projectiles and targets.

Several conclusions can be extracted from the analysis of the data at the relatively low impact velocity of 1.5 km/s. In this configuration, a tungsten projectile will produce a deeper impact. This is due to the density of tungsten being much higher than that of zirconia or diamond. At equal length, the projectile will be heavier and, forces exerted by the target in opposition of the motion being the same, it will take more time to decelerate it. The depth of impact will be also larger in soft soil materials due to its lower density with respect to hard rock, which translates into less pressure upon the projectile tip. When the interface velocity becomes much less than $\sqrt{2R_t/\rho_t}$, the stopping force is dominated by the R_t term. In soft soils, this term is extremely small, which leads to very large stopping times (in the order of seconds instead of miliseconds). However, as seen in Figure 36, the additional depth of impact obtained in the last period of the motion is small and, as presented in the previous paragraph, these results are questioned by the fact that target pressure model ceases to be valid at very small velocities.

Table 13: Penetration depth and time for cases in which the projectile is made of tungsten (W), zirconia (ZrO2) and diamond (C), with target hard rock (HR) and soft soil (SS). Impact velocity is 1.5 km/s.

	Model	W+HR	ZrO2+HR	C+HR	W+SS	ZrO2+SS	C+SS
	0-D	24.55	7.71	4.48	120.85	37.97	21.96
d_f/L	1-D	10.08*	6.17*	4.5*	11.36*	7.88*	6.25*
	2-D	8.799*	5.92*	2.38	8.799*	8.782*	5.287**
	0-D	72.88	22.9	13.24	6.36e3	2.00e3	1.15e3
t_f (ms)	1-D	10.00*	10.00*	10.00*	10.00*	10.00*	10.00*
	2-D	7.702*	10.00*	4.63	6.91*	9.537*	6.238**

6.4.2 10 km/s impacts

At high velocities, at least some regions of the projectile will undergo plastic deformations. In the case of tungsten, the projectile will be completely destroyed after the impact while for zirconia and diamond, part of the material will withstand the impact. For these cases, we can not only compare the depth of impact between models but also validate our results by comparing the velocity V_p at which the two tips of the projectile start moving at the same velocity (i.e., the end of the plastic regime in the projectile). Table 14 summarizes these results. As in the previous subsection, simulations were constrained to a running time of 10ms. For the 0-D model, the penetration depth cannot be determined if the remaining length of the projectile is 0 (for tungsten). Only one 2-D simulation for soft soil was run, with diamond as projectile material. In Figure 37, we show the time evolution of the projectile tips and the penetration depth for cases in which hard rock has been used as target.

Important differences arise between the three models in this high velocity configuration. The 1-D and 2-D models are able to track the motion of shocks in the solid. This can be observed in the fact that the velocity at the trailing tip, V, remains constant until the first shock arrives and then the deceleration happens instantaneously. Even when the 0-D model does not capture shocks, the agreement between this model and the 1-D model is very good. Again, the 2-D model introduces important differences that are related to the more complex behavior of the target captured in full 2-D simulations. Under 10km/s impact conditions, the target material can be significantly compressed, as observed in the contour plots of Figures 38 and 39. This phenomenon increases the effective pressure that the target exerts to the motion of the projectile, increasing the deceleration and reducing the penetration depth. This is observed in all the cases run with the 2-D model. The remaining length of the material is also reduced in the 2-D model due to expansion of the projectile in the radial direction that is not captured in the simpler models. For the zirconia 2-D simulation, the deceleration is very abrupt compared to the other models. An explanation for this can be found in Figure 38, where it can be observed how the contact area between the projectile and the target has increased as the projectile material has flowed radially. Assuming that the pressure conditions are similar, a greater contact area results in a larger net force attempting to stop the projectile.

If the results for the 10km/s case are compared to those at 1.5km/s, we observe that the depth of impact is not excessively increased. This can be explained by the energy of the impact being largely lost in plastic work in the projectile and target (we will show in the next subsection how the plastic deformations in target and projectile are much greater than in the 1.5km/s). We must conclude that a 10km/s impact is less efficient than a 1.5km/s impact. For example, diamond on hard rock at 10km/s produces a depth of 3.36m in comparison to 2.38m at 1.5km/s. In the case of zirconia, the depth predicted by the 2-D simulations at 10 km/s is less than the depth at 1.5km/s due to the large radial deformations that increase the contact area between impactor and target.

Figure 39 shows the effect of a diamond projectile on soft soil at 10 km/s. These plots can be compared to those shown for diamond on hard rock in Figure 38. In the soft soil scenario, the projectile undergoes less plastic deformations (due to the lower density of the soil) and in consequence the impact is deeper. Due to the low strength of soft soil, it can be observed that a large portion of the material has been obliterated upon impact.

6.5 2D-specific results

We investigate in this section two variables that are key to concept feasibility: crater size and sensitivity to incidence angle of the projectile. The former will determine whether the projectile can function as a harpoon, attaching to the target material. For this to happen, the diameter of the crater cannot be too large and the projectile has to remain

Table 14: Penetration depth and time for cases in which the projectile is made of tungsten (W), zirconia (ZrO2) and diamond (C), with target hard rock (HR) and soft soil (SS). Impact velocity is 10 km/s.

	Model	W+HR	ZrO2+HR	C+HR	W+SS	ZrO2+SS	C+SS
	0-D	0	0.30	0.83	0	0.52	0.96
l_s/L	1-D	0	0.28	0.85	0	0.48	0.94
	2-D	0	0.27	0.7	Not run	Not run	0.83
	0-D	1.65	5.36	7.09	2.05	6.58	8.69
V_p (km/s)	1-D	1.66	4.66	7.09	2.00	6.41	8.75
	2-D	2.60	3.53	5.31	Not run	Not run	6.52
	0-D	N/A	15.5	9.35	N/A	51.0	29.3
d_f/L	1-D	5.25	11.56*	8.65*	0.65	16.3	13.05
	2-D	2.93	3.38	3.36	Not run	Not run	7.291
	0-D	N/A	25.36	14.63	N/A	1.93e3	1.15e3
$t_f(ms)$	1-D	0.55	10.00*	10.00*	7.59	10.00*	10.00*
	2-D	0.50	3.26	2.92	Not run	Not run	5.28*

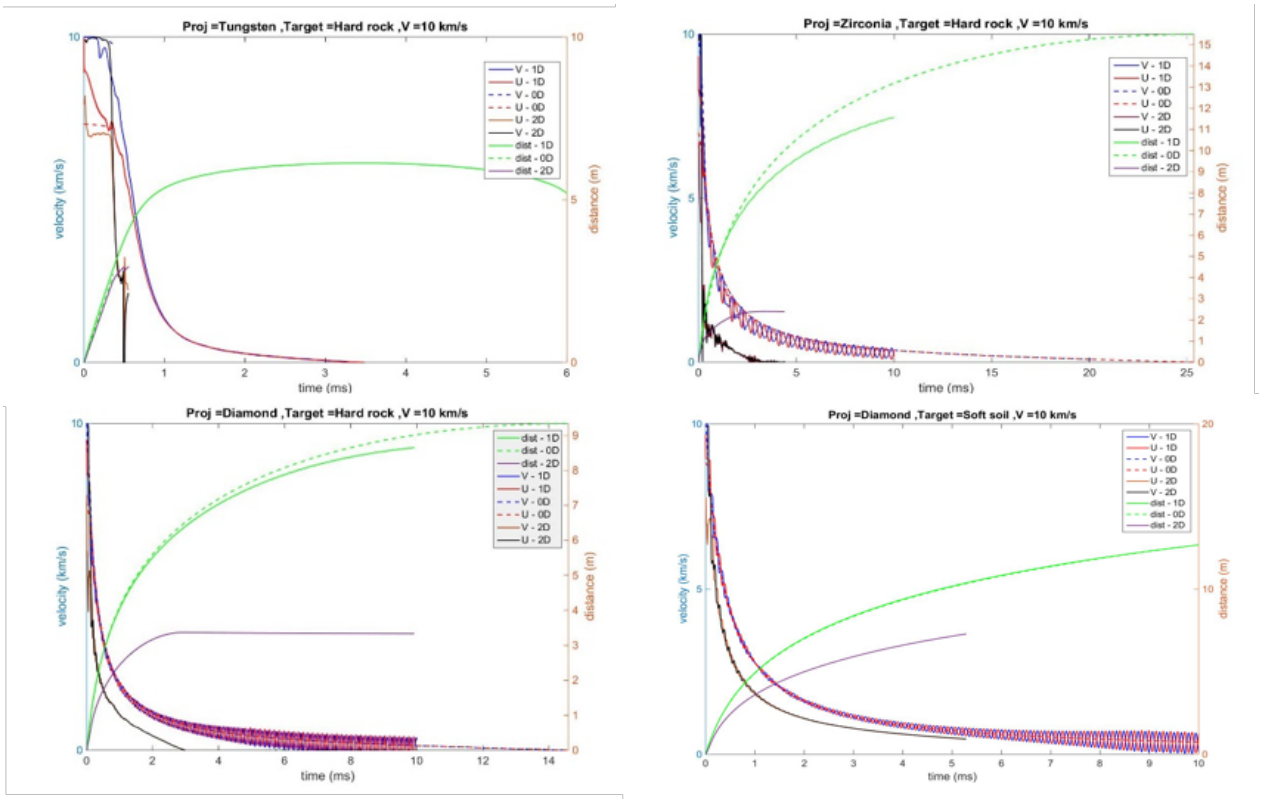

Figure 37: Time evolution of leading tip velocity (U), trailing tip velocity (V), and penetration depth as a function of time for different projectiles and hard rock target at 10 km/s. We have also included the results for diamond impact on soft soil at 10 km/s.

embedded in the target. We have already shown in the previous section (Figure 38) that the craters produced by the impact of tungsten and zirconia at 10km/s are not conductive to the projectile behaving as a harpoon. We will also investigate here the effect of the aspect ratio of the projectile. With respect to the angle of incidence, the prime interest here is to determine how sophisticated the control of the projectile needs to be. If even small angles of incidence produce an unstable behavior of the projectile resulting in large craters, the feasibility of the concept may require a

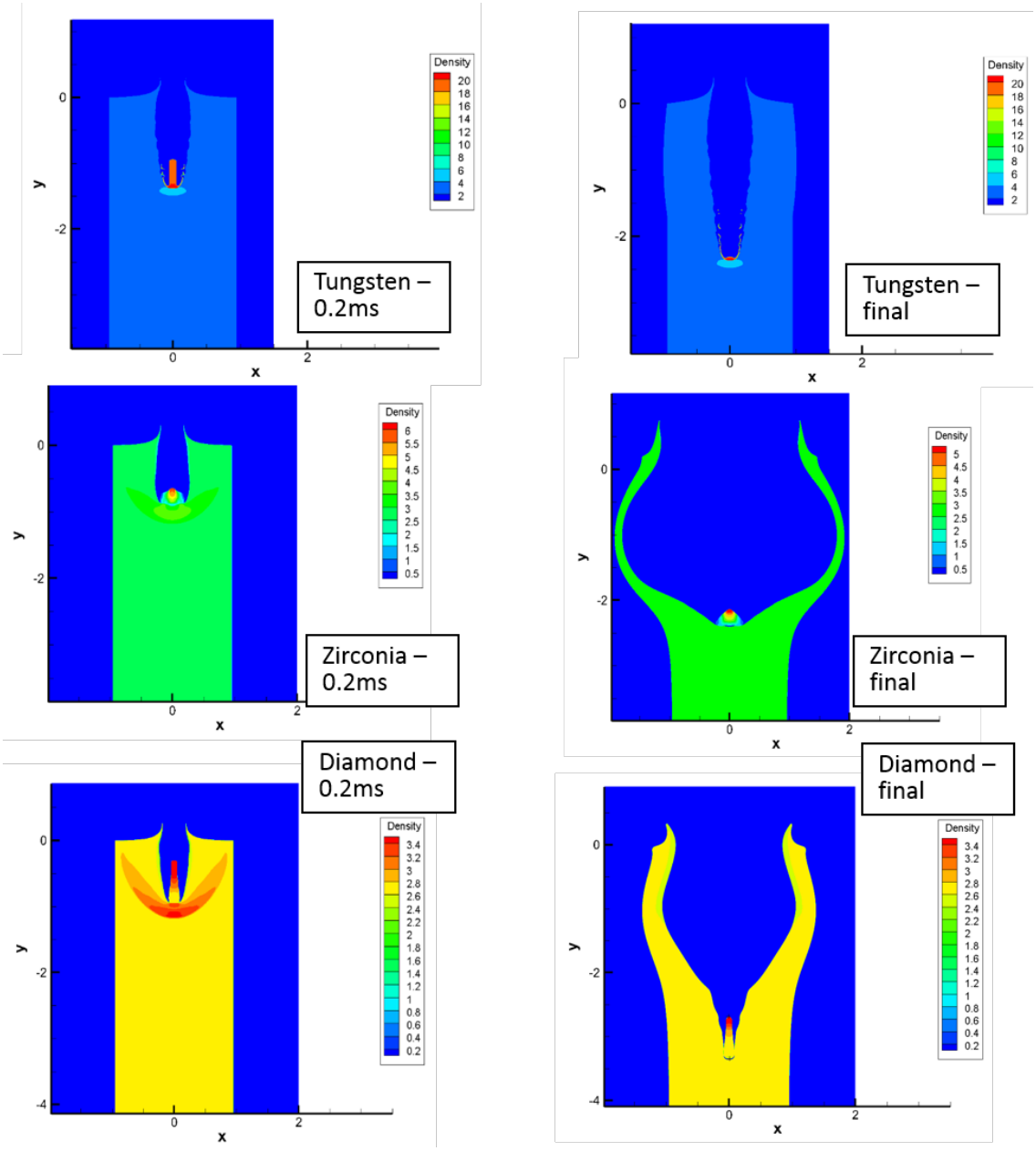

Figure 38: Contour plots of the density in the 2-D model for tungsten, zirconia, and diamond against hard rock at 10 km/s. The first column shows conditions just after impact (depicting compressibility in the target not captured by the 0-D or 1-D models). The second column shows conditions at the end of motion.

very precise control system.

6.5.1 Crater size in perpendicular impact

Table 15 presents the crater diameter with respect to the projectile diameter for multiple 2-D simulations. For the carbon impact on hard rock at 1.5 km/s, we consider multiple values of the projectile aspect ratio. The ideal condition is for the diameter of the crater to be equal to the diameter of the projectile at the location where the projectile rests at the end of the motion. However, it may occur that the projectile is partially embedded (as seen in Figure 38 for diamond). In order to provide a description as accurate as possible, we report four different diameters. d_1 is the

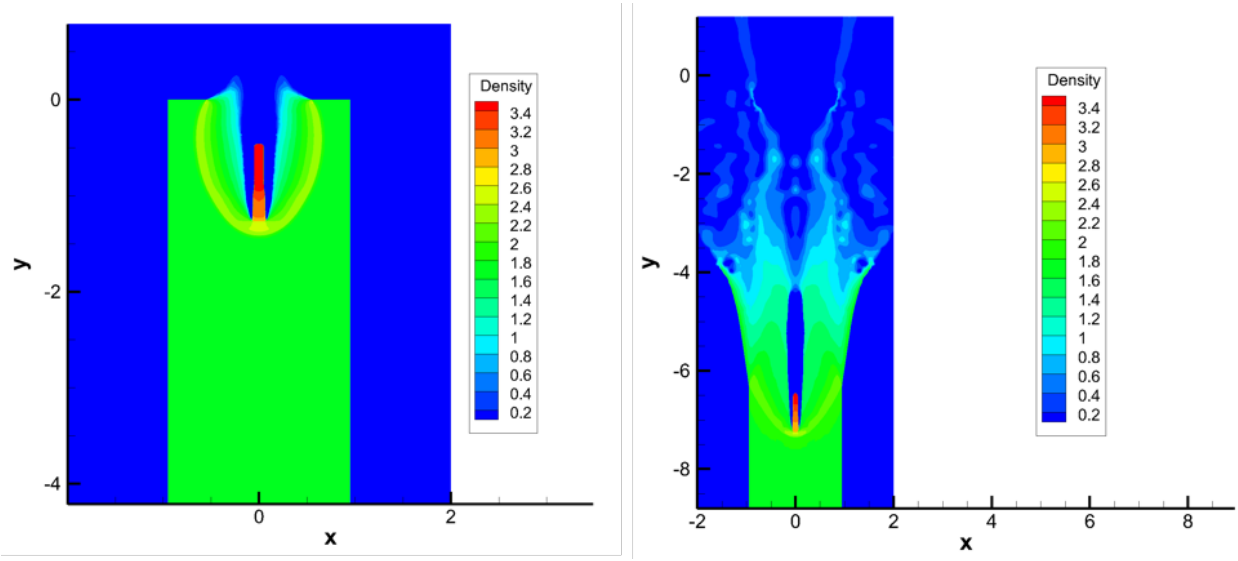

Figure 39: Contour plots of the density in the 2-D model for diamond against soft soil at 10 km/s. The first plot shows conditions just after impact (depicting compressibility in the target not captured by the 0-D or 1-D models). The second plot shows conditions at the end of motion.

diameter at $1/4$ of the projectile length from the leading tip, d_2 is the maximum diameter along the axial location of the projectile, d_3 is the maximum diameter in the radial locations above the projectile within one length of the trailing tip of the projectile, and d_4 is the absolute maximum diameter. Figure 40 shows graphically these diameter definitions.

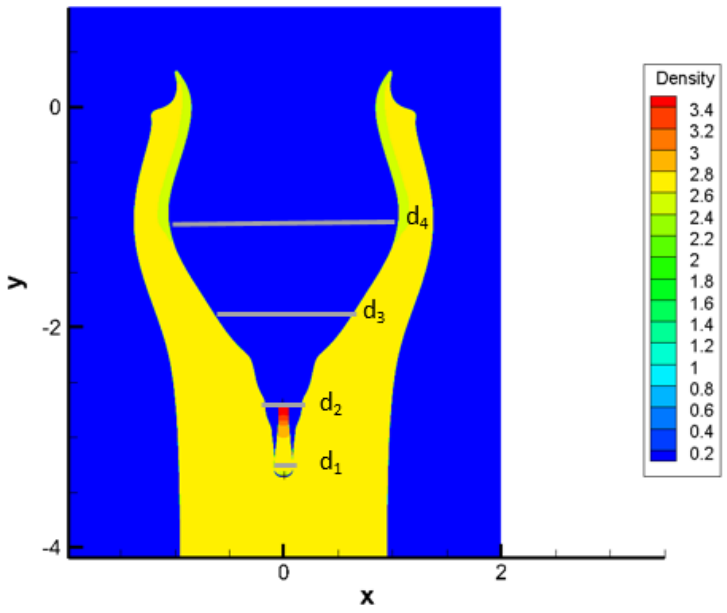

Figure 40: Definition of crater diameters used in Table 15.

Results suggest that at the low velocity condition, the crater diameter mostly depends on the target material, as the diameters for multiple projectile materials are very similar. It is only in d_3 where significant changes are observed. This is because this value depends on the impact depth. For a deeper impact, such as with tungsten, the crater has a

funnel shape while in the case of diamond, its shape is more conical. With respect to the target material, the soft soil deforms more under impact than the hard rock, resulting in larger crater diameters. Intuitively, it should be easier to attach a harpoon to a rigid material than to a soft one. The summarized results also show that, at least at low velocities, the aspect ratio of the projectile has almost no influence on the diameter of the crater when scaled with the diameter of the impactor. It would be however advisable to perform a similar investigation at the high velocity case, as the physics at work when plasticity appears in the projectile may reveal a different trend. At high velocities, the only projectile that can survive and have good chance of working as a harpoon is the diamond one. Even when part of the zirconia impactor resists the impact, its shape is so deformed that the probability of such a projectile to work as a harpoon is extremely low. In Figure 41, we complete this discussion showing the crater and projectile shapes for multiple cases.

Table 15: Crater diameters (definitions according to Figure 40) with respect to maximum deformed diameter of projectile D' for projectiles (C=diamond, Zr=zirconia,W=tungsten), targets (HR= hard rock, SS =soft soil), impact velocities and aspect ratios, L/D.

		C+HR, 1.5km/s		C+SS, 1.5km/s	C+HR, 10km/s	C+SS, 10km/s	Zr+HR, 1.5km/s	Zr+SS, 1.5km/s	Zr+HR, 10km/s	W+HR, 1.5km/s	W+SS, 1.5km/s	W+HR, 10km/s
L/D'	10	5	2.5	10	10	10	10	10	10	10	10	10
d_1/D'	1	1	1	1.56	1	1.41	1	1.54	1.54	1	1.70	N/A
d_2/D'	1.33	1.08	1.24	2.15	1.57	2.00	1.22	2.14	2.74	1.2	2.2	N/A
d_3/D'	1.56	1.67	2.17	8.21	3.58	2.35	1.24	4.5	4.27	1.5	2.5	N/A
d_4/D'	3.33	3.45	3.1	12.3	12.41	13.1	3.26	12.28	8.20	3.4	9.62	9.78

6.5.2 Oblique impacts

The aim of this subsection is two determine whether the incidence angle of the projectile is a key parameter for this proof of concept. Three additional simulations were run with a carbon projectile and a hard rock target. At 10 km/s, incidence angles of 1 and 10 degrees were tested, while at 1.5 km/s, only the 10 degree case was attempted. It is important to note that these simulations were run in a two-dimensional computational domain, assuming that the materials are infinitely long in the third dimension, while the perpendicular impact cases were run in the same 2-D computational domain including terms that account for cylindrical symmetry around the axial centerline of the projectile. The initial configuration of the problem with an angle of incidence of 10 degrees is shown in Figure 42. The width of the target was increased to account for the oblique motion of the projectile inside the target.

Figure 43 shows a comparison of the final state of the system for a 1.5km/s impact. The first feature of the result of the oblique impact simulation is that the projectile has reversed its orientation. This phenomenon can be attributed to the angular momentum that is exerted after the initial contact between the projectile and the target. At first instance, the angular momentum tries to expell the projectile (which may happen at higher incidence angles) but as soon as a crater is formed and penetration begins, the projectile is deflected in the opposite direction by the pressure exerted in the radial direction by the target. This phenomenon is exarcebated by the slender shape of the projectile, which produces a long arm for the moments computed around the center of mass of the projectile. It is also noticeable that the crater is much wider and the projectile is not as well embedded as it is in the normal impact case. The ability of the impactor to work as a harpoon is therefore compromised by small deviations in the incidence angle.

In Figure 44, we present the same comparison for the 10km/s impact, including the case with incidence angle of 1 degree. For this initial condition, the effect of even a very small deviation in the incidence of the projectile is devastating. As in the previous case, the projectile changes its orientation, producing a larger crater. In addition, the projectile is not embedded in the target material. This analysis suggests that the probability of the harpoon attaching to the target in the case of oblique impact at high velocities is extremely remote.

These simplified simulations show that the incidence angle is a determinant factor for the feasibility of the Comet Hitchhiker concept. In a future study, the real 3-D case (instead of the 2-D simplification presented here) must be considered and possible mitigation techniques, such as modifying the shape of the leading tip of the projectile explored and tested.

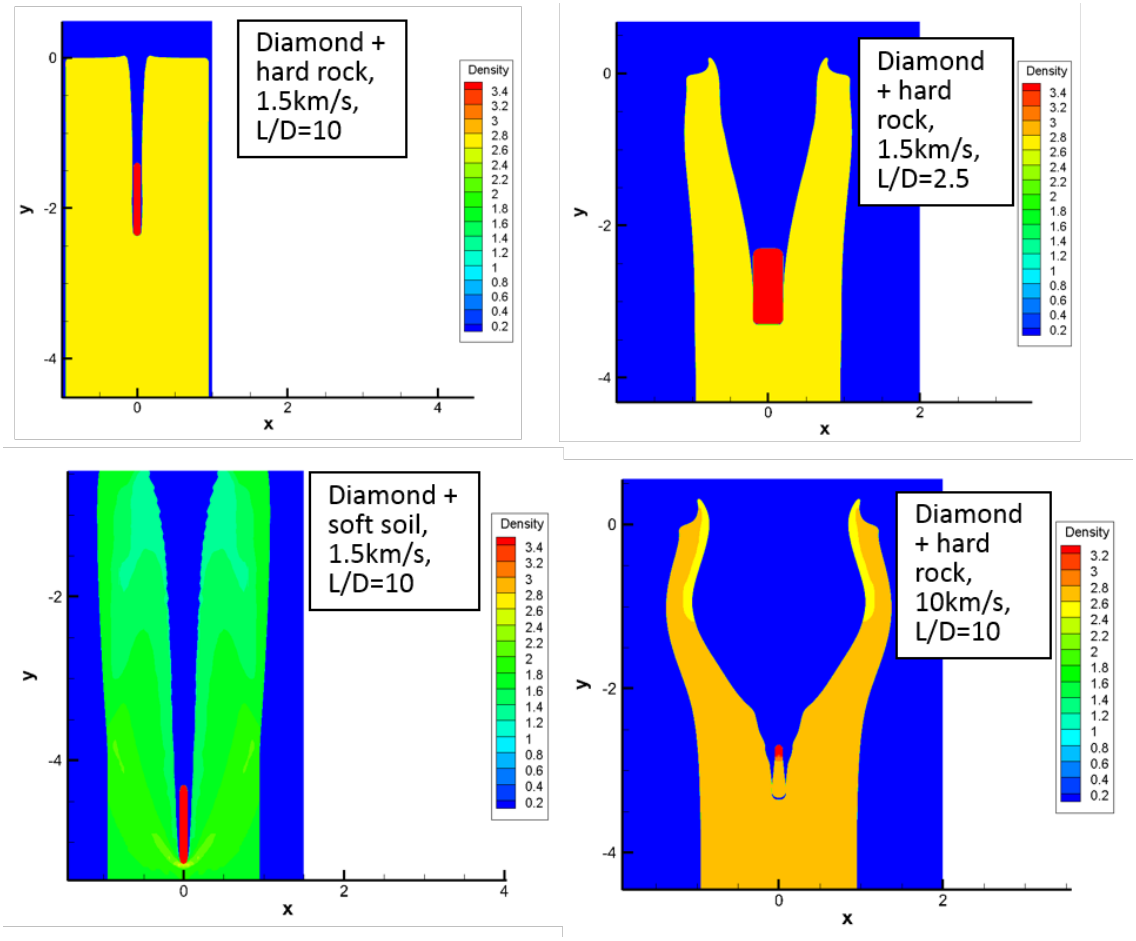

Figure 41: Crater and projectile shapes at the final configuration as a function of target material, impact velocity, and aspect ratio of the projectile.

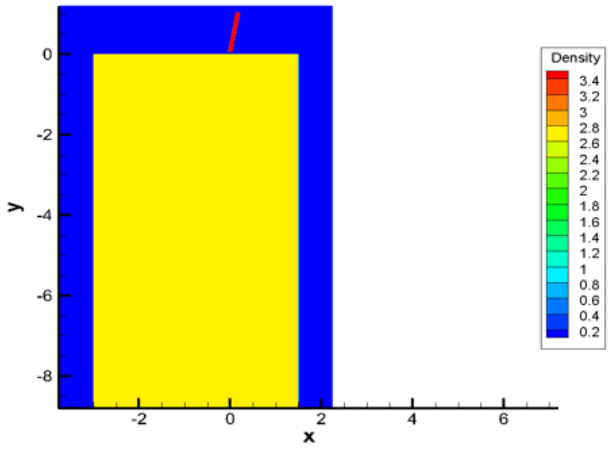

Figure 42: Initial configuration for oblique impact with incidence angle of 10 degrees.

6.6 Parametric study of impact velocity

In this section, we complement the results already shown for 2-D simulations at impact velocities of 1.5 km/s and 10km/s with two new data points at 5km/s and 8km/s. Only normal impacts are considered and all simulations are run

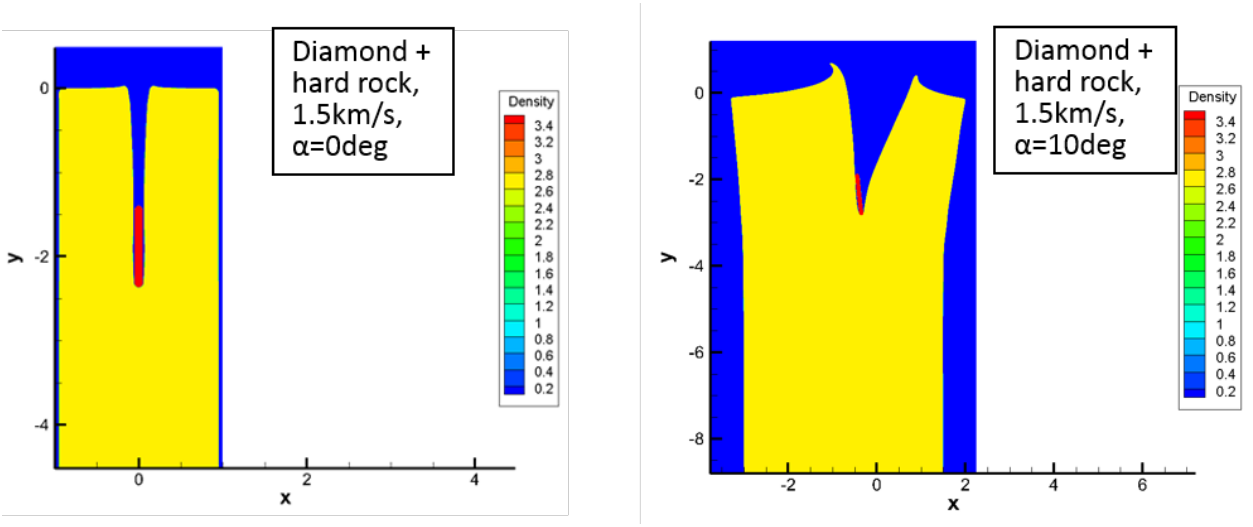

Figure 43: Comparison of crater diameter and final position of the projectile for normal and oblique impacts at 1.5 km/s.

with an L/D ratio of 10. We show results for depth of impact df, crater diameter (using the d_1, d_2, and d_3 definitions presented in the previous section), and remaining length l_s of the projectile.

A combined analysis of the results in Tables 16-20 reveals that tungsten is the most appropriate material to be used in low velocity impacts. Due to its larger density, which translates into a higher initial kinetic energy in the system if the projectile dimensions do not change, a tungsten projectile is capable of producing a deeper impact with low crater diameters as long as the material remains in the elastic regime. However, as the velocity of the impact is increased, the option of using a tungsten impactor becomes less optimal. At 5 km/s, only a tiny fraction of the projectile is capable of surviving the impact.

At the velocities of 5km/s, zirconia and diamond are the likely choices as these materials do not undergo plastic deformations in this conditions. It can observed that the penetration depth is maximum (as the kinetic energy of the impact is not lost in plastic deformations of the projectiles) and crater diameters are conductive to the projectile becoming embedded into the target.

As the velocity is increased to 8km/s, the impact depth is reduced due to the presence of plastic deformations. This is also translated into larger crater diameters than before. At the same time, radial deformations in the projectiles increase. For this reason, we present the diameter non-dimensionalized with the maximum diameter of the deformed projectile. Results show that there exists compensation between larger crater diameters and radial deformations of the projectile, and the likelihood of a zirconia or diamond remaining attached to the target is large.

In the final case of a 10km/s impact, the only suitable option is diamond. Even when approximately 1/3 of the zirconia projectile survives, the created crater is too wide for any attachment to occur. Even in the case of the diamond projectile, attachment can be compromised in this case.

6.7 Summary, conclusions and future work

Three models have been used to assess key questions on the behavior of a rod projectile under hypervelocity impact conditions in rock and soil. The key findings are:

1. At low velocity conditions (1.5km/s), the metal and ceramic materials tested do not undergo plastic deformations and the projectile is intact when it stops inside the material. Crater depths are a typically few times the length of the projectile and increase with the mass of the impactor. In this condition, the tungsten projectile would represent the best option due to its higher density. The crater diameters at low velocities are small, which increases the probability of the harpoon attaching to the geological material of the celestial body. Crater diameters decrease with the strength of the target material so attaching to a strong rock is easier than into soil.

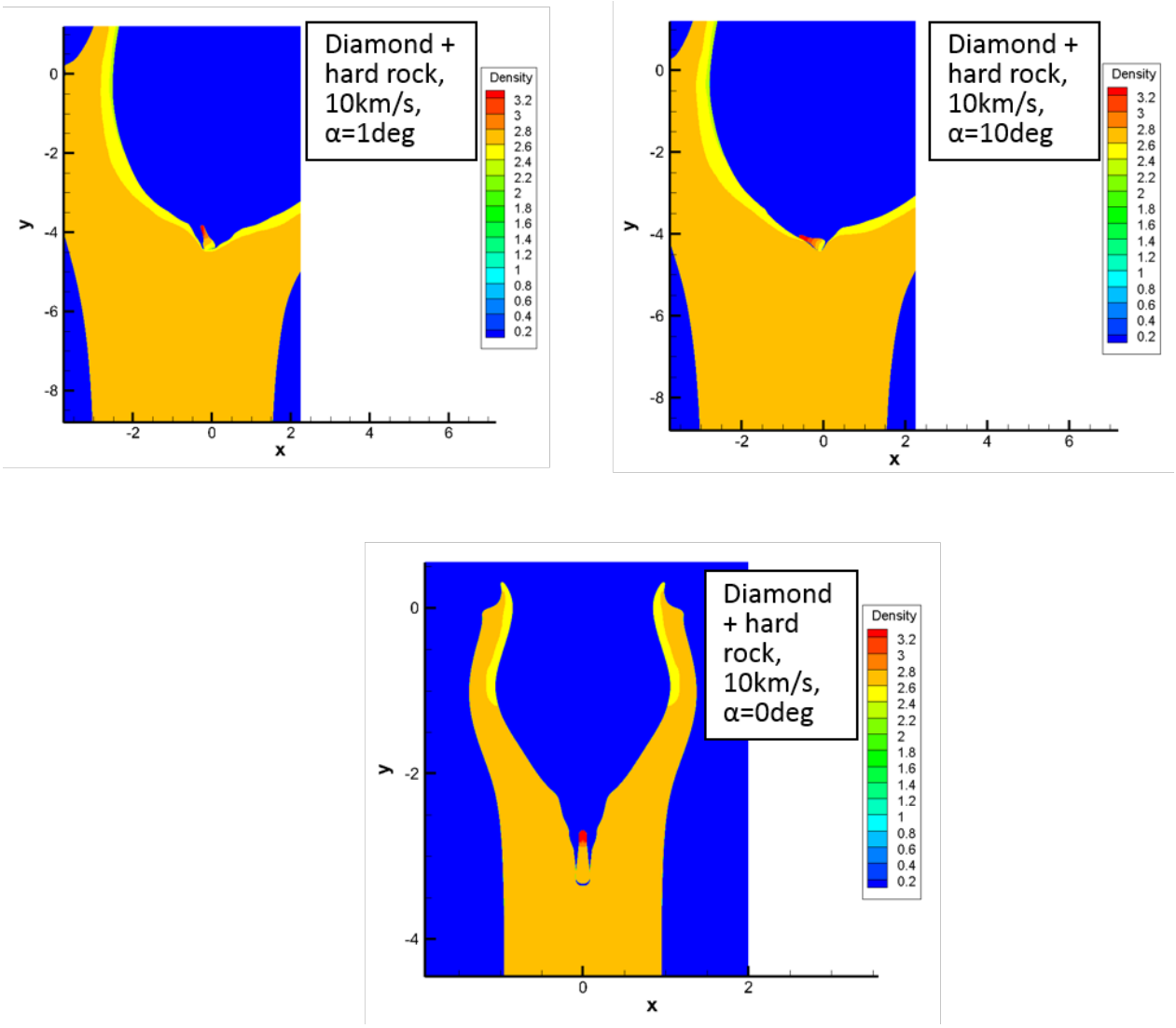

Figure 44: Comparison of crater diameter and final position of the projectile for normal and oblique impacts at 10 km/s.

2. At intermediate velocity conditions (5km/s and 8 km/s), tungsten is no longer an option and ceramic materials are required. As the velocity increases, diamond becomes progressively better suited for this application than zirconia.

3. At high velocity conditions (10km/s), only the strongest material tested (diamond) can effectively function as a harpoon. The crater diameters are higher as more initial kinetic energy of the projectile is spent in plastic deformations in both target and projectile. This is translated into penetration depths not significantly larger than in the 1.5km/s. Even when part of zirconia projectile survives the impact, this material undergoes large radial deformations increasing the diameter of the crater and reducing the depth of impact. A tungsten projectile would be completely destroyed in these conditions.

4. The obliquity of the impact has a profound effect in the crater width and poses a challenge for the Comet Hitchhiker concept. This is due to the shape of the projectile, conductive to large torques produced by the pressure exerted by the target not being aligned to the projectile axis. Simulations show that the projectile can even change orientation during the impact, reducing the probability of becoming embedded in the target material.

Table 16: Penetration depth with respect to initial length of projectile, d_f/L (* denotes projectile was still in motion at the end of the simulation)

	Impact velocity (km/s)			
Material	1.5	5	8	10
C+HR	2.38	7.22	4.43	3.36
ZrO2+HR	5.92	8.79*	4.11	3.38
W+HR	8.799*	4.84	2.87	2.93

Table 17: Crater diameter at location 1 (see Fig. 40) with respect to deformed maximum diameter of the projectile, d_1/D

	Impact velocity (km/s)			
Material	1.5	5	8	10
C+HR	1	1	1	1.00
ZrO2+HR	1	1	1	1.54
W+HR	1	1	N/A	N/A

Table 18: Crater diameter at location 2 (see Fig. 40) with respect to deformed maximum diameter of the projectile, d_2/D

	Impact velocity (km/s)			
Material	1.5	5	8	10
C+HR	1.33	1	1.56	1.57
ZrO2+HR	1.22	1	1.15	2.74
W+HR	1.2	1	N/A	N/A

Table 19: Crater diameter at location 3 (see Fig. 40) with respect to deformed maximum diameter of the projectile,d_3/D

	Impact velocity (km/s)			
Material	1.5	5	8	10
C+HR	1.56	1.64	3.83	3.58
ZrO2+HR	1.24	1.5	1.68	4.27
W+HR	1.5	1.24	N/A	N/A

Table 20: Remaining length of projectile with respect to initial length, l_s/L

	Impact velocity (km/s)			
Material	1.5	5	8	10
C+HR	1	1	0.87	0.70
ZrO2+HR	1	0.97	0.50	0.27
W+HR	1	0.1	0	0

Future work in the modeling and simulation front has to be focused in understanding whether certain projectile shapes (like arrowhead or blunt) can minimize the negative effects observed in oblique impacts. Full 3-D simulations appear to be necessary to address this concern as the simplifications used in these simulations (2-D with projectile and target infinitely long in the third dimension) may have contributed to the adverse effects that have been described.

Another factor for uncertainty in these simulations is the approximate values used in the simulations of the target material and ductile plasticity model not being the best model to describe the behavior of soils and rock. If the release

of the kinetic energy of the projectile is done through fracture of the material instead of plastic deformations, variables such as crater width may be affected. Unfortunately, combining fracture mechanics with dynamic behavior of materials is not straightforward and may require an effort beyond the scope of the NIAC program that must be funded through other sources.

7 Harpoon Penetration and Anchoring

In this section we investigating harpoon penetration and anchoring by 1) studying past researches and 2) comparing with relevant missions.

7.1 Harpoon penetration physics

Projectiles traveling through the ground do not always travel in a straight path. Under certain conditions, the trajectory will take on a curvilinear shape. This J-Hook phenomenon makes it difficult to determine the trajectory. Additionally, the entire harpoon would not stay in contact with the surrounding soil. This condition is known as Wake Separation. A stress would be exerted on the harpoon only where the soil is in contact with the surface of the harpoon. Finally, there is Trajectory Direction Reversal. At some critical incidence angle a harpoon that would normally execute a J-Hook trajectory no longer travels back toward the surface, but dives away from the surface, driving the harpoon much deeper than expected. All of these issues make accurate prediction of a penetrator's trajectory very challenging.

Large cometary bodies typically spin slowly and may have more strengthless material on the surface than small bodies, which tend to spin faster. For example: a buried circular disk penetrator has a vertical pullout capacity of about 68 times the weight of the soil in a cylinder above the disks surface area, for a soil friction angle $\phi = 40$ deg and a depth of burial 10 times the disk diameter. Therefore, for a 10 km radius asteroid with 2000 kg/m3 regolith, a vertical pull-out capacity of 300N requires the weight of 0.26 m3 of regolith, or a 32 cm diameter disk buried at a depth of 3.2 m.

A cylindrical harpoon (pile) is an alternative choice, but still requires a diameter of 32 cm and a length of 7m for pullout capacities of 300N on 10 km radius asteroids, using the pile skin friction equations. In practice, there may be predominantly lateral loading on the harpoon, which complicates the analysis. It is likely that regolith harpoons would require significant burial depths and surface areas to be effective.

Early studies on penetration for the ST4/Champollion mission selected a 1 kg 1.9cm diameter truncated cone penetrator for penetration onto the surface on materials of strength up to 10 Mpa with a 45 degree impact angle within a reasonable velocity range (100-200 m/s) with a minimum pullout resistance of 450 N in any direction. A penetration deployment issue is that the harpoon may ricochet adversely on surface instead of solidly emplacing on ground.

Harpoons could be easily launched before landing. Spacecraft ACS (reaction wheels, not RCS) would probably need to be on during the penetration Phase to avoid vehicle stability problems. Some harpoon designs would allow them to be pulled out, others would not. Figure 45 and Figure 46 are taken from [8], and depicts the ranges of forces that would be expected in proximity of the surface of a comet. Figure 47, taken from [29], summarizes typical behavior observed in penetration tests on different types of targets, indicating the possibility of ricochet of the projectile depending on the approach speed, direction, and surface material parameters.

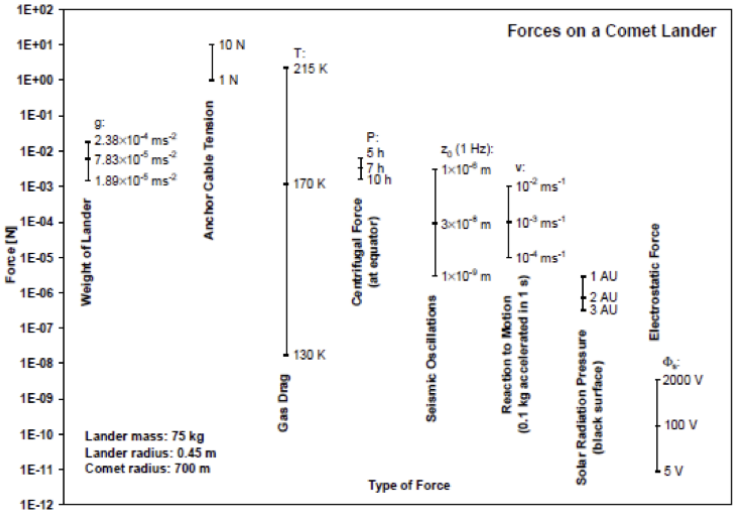

Figure 45: Forces On Comet Lander, taken from [8]

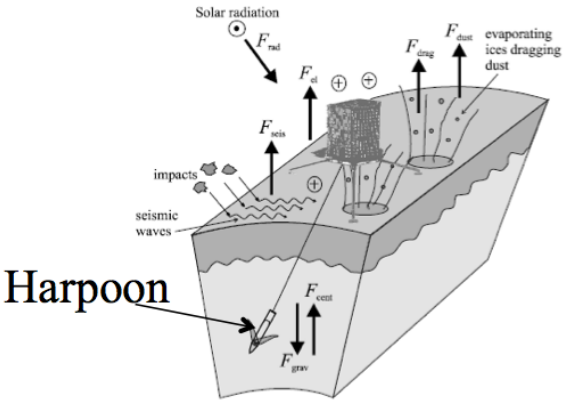

Figure 46: Environment around harpoon on Comet, taken from [8]

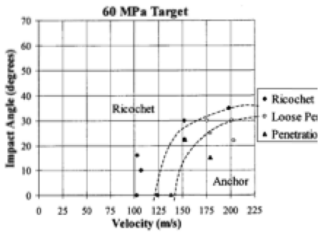

Figure 13. Anchoring Threshold Results for Targets with 60 MPa Compressive Strength

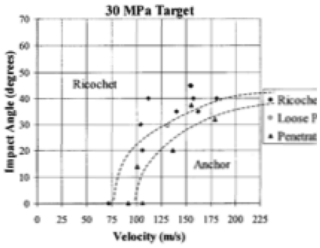

Figure 14. Anchoring Threshold Results for Targets with 30 MPa Compressive Strength

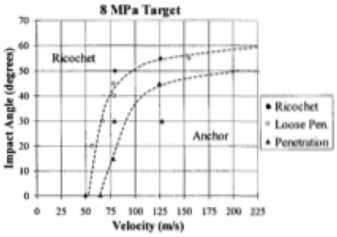

Figure 15. Anchoring Threshold Results for Targets with 8 MPa Compressive Strength

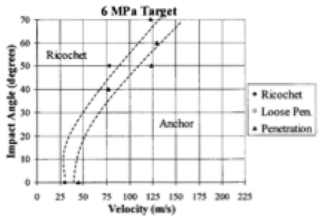

Figure 16. Anchoring Threshold Results for Targets with 6 MPa Compressive Strength

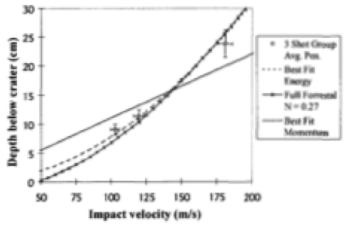

Figure 17. Penetration Depth vs. Impact Velocity

Figure 47: Possibility of Ricochet, taken from [29]

7.2 Regolith Modeling

Behavior of the regolith is likely governed by cohesion and surface adhesion effects that dominate particle interactions at small scales through van der Waals forces. Electrostatic forces are generally negligible except near terminator crossings where it can lead to significant dust transport. The micro-gravity and solar radiation dominate system behavior prior to soil engagement or penetration.

Soil mechanics experiments have known issues when it comes to testing samples of regolith in one-g. First, a reproducible preparation of a homogeneous soil sample is difficult to achieve. Second, a characterization of the soil properties in depth is difficult, since static parameters are typically measured at the surface. Third, under 1-g load, according to soil theory, the compressive strength in depth is significantly influenced by overburden terms, i.e. the effective strength/resistance increase with depth. The soil shear stress can be modeled as

$$\sigma_c = c + p\tan(\phi_f) \tag{30}$$

i.e., the Mohr-Coulomb limit soil bearing capacity theory, where ϕ_f, is known as the friction angle (or internal-angle-of-friction), p is normal pressure, and the zero normal-stress intercept, c, is known as the cohesion (or cohesive strength, i.e. shear stress at p=0) of the soil. For typical regolith simulant, the cohesion is 40 Pa at loosely packed conditions and increases to 10 kPa at 100 relative density. The friction angle also increases monotonically from 25 deg to 60 deg. The Rosetta Lander design takes advantage of this effect of greatly increased cohesion by local compression of the cometary regolith under the landing pods during landing. Previous relevant regolith modeling work [8], and [9] covers both low-velocity (approx. 1 m/s) impact of blunt bodies into dust-rich, fluffy cometary materials (Biele et al [8]), as well as high-velocity (approx. 10 m/s) impact of sharp projectiles on various types of soil. (Allen [2] and Anderson et al [3]). The lower limit of the tensile strength is of the order of 1kPa whereas the probable upper limit can be taken as 100kPa. The lower limit of tensile strength corresponds to a compressive strength of c $\geq$ 7kPa. This wide range of soil properties must be captured in simulation, which poses a significant challenge.

At very low gravity and vacuum conditions the biggest unknown is the material strength of the surface material. Neither the Deep Impact mission nor other comet observations have provided firm data on the strength of cometary material. Theoretical considerations and laboratory measurements for weakly bound aggregates and the few observational constraints available for comets and cometary meteoroids lead to estimates of the quasi-static tensile (or shear) strength of cometary material in the dm to m range as of the order of 1kPa, while the compressive strength is estimated to be of the order of 10kPa. In the following, we summarize the current state of knowledge in asteroidal and cometary regolith behavior.

- *Cohesion, tensile, shear and compressive strength*: While for brittle materials tensile strength is generally less than the shear strength, compressive strength is about one order of magnitude higher than tensile strength. In the case of soft landing compressive strength is the relevant parameter. Shear, tensile and compressive strength are indicated by σ_s, σ_t, σ_c, respectively.

- *Dynamic and quasi-static strength*: During impacts, due to very high strain rates, the dynamic strength is typically higher than the quasi-static strength. It is known that the strength increases with strain- rate resulting in values about an order of magnitude higher (or even more) than the quasi-static strength for the same material. Generally the tensile strength σ_t is proportional to a power b of the strain rate $\dot{\varepsilon}$ with a power law exponent typically around 1/4 to 1/3, depending on the material.

- *Size dependence*: Different theories indicate that the strength decreases with increasing size according to d^{-q} where the exponent q is approximately 0.5 (fractal aggregate with fractal dimension D = 2.5 of ice). Thus, if extrapolated from typical lander (0.1m), or impactor (1m) to typical comet (1 to 10 km) scales, the size effect alone would produce a factor of 100 in the apparent strengths. This is in line with the observation that comets can often be described as essentially strength-less bodies (large cometesimal, rubble pile, swarm models) globally, while locally a significant material strength is to be expected.

- *Breakup of Comets, Topography Observations*: Tidal disruption of comets indicate low global tensile strengths in the order of 100 to 10,000 Pa. For example, the break-up of Shoemaker-Levy 9 during its perijove in 1992 set a rough upper limit of the tensile strength (on global/km scales!) of 100Pa. The tensile strength of sun-grazing comets has been estimated as 10kPa with some uncertainty due to thermal stresses. Images by Stardust from comet 81P/Wild-2 showed that the cometary surface must have a finite strength on short scales ($<$ 100 m) to support the observed topographic features; because of the small gravity, some 10P a might suffice. Otherwise, only lower bounds on the tensile strengths are available in the order of $1 \ldots 100$ Pa.

- *Breakup of Meteoroids*: Another source of information about possible strength values of cometary surfaces on mm to dm scales stems from the analysis of meteoroids associated with certain comets which enter the earth atmosphere at high speeds and finally break-up and create a light flash. Wetherill [37] gives values for tensile strengths of these fireballs ranging from 1 kPa to 1 MPa. More recently, Trigo-Rodrguez and Llorca [33] have studied a broad data base of meteor ablation light curves and arrive at tensile strengths between (400 $\pm$ 100 Pa and 40 kPa, clustering around 10kP a for not too evolved and rather low density $<$ 1g/cm3 (if known) cometary meteoroids.

- *Laboratory Measurements*: The small scale (cm) shear and tensile strength of snow in the relevant density range of 300 to 500 kg/m3 is of the order of 10 to 100 kPa. The tensile strength of snow is nearly independent on temperature, while the compressive strength shows a remarkable increase with decreasing temperatures. Simulating possible cometary analogue material in the scope of the KOSI experiments concluded that the small-scale

compressive strength of porous mixtures of crystalline ice and dust lies in the range between 30kPa and 1MPa with increasing strength for an increasing dust fraction.

- *Limits Derived from Comet Size and Rotation*: Stability against disruption due to rotation yields lower limits for the combination of bulk density and tensile strength. Rotational periods and sizes for many comets are known, but the corresponding bulk densities are not well constrained. For example, a fast rotating big comet such as C/Hale-Bopp (1995 O1) could be a strength-less rubble pile with a bulk density as low as 100 kg/m3.

- *Theoretical Estimates*: There are different approaches to describe the tensile strength of powders on the basis of van der Waals interactions, cf. Greenberg et al.,[11] or Chokshi et al. [**?**]. The latter model includes the elastic deformation of contacting spherical grains. The theoretical tensile strength of fluffy aggregates depends on particle radii, contact areas, packing geometry and typically scales with the bulk density. Greenberg et al. estimate a tensile strength, for interstellar silicate dust/ice material with a density of 280 kg/m3, of 270 Pa. Sirono and Greenberg [13] derive 300 Pa for the tensile and 6000 Pa for the compressive strength for a medium composed of ice grains linked into chains by intermolecular forces. Kuhrt and Keller [18] derive a theoretical strength of 100Pa and 100 kPa for grains of 1mm and $1\mu m$, respectively. Note that 95% of the Deep Impact ejecta dust cross section is represented by particles $r < 1.4\mu m$. From the discussion above the conclusion can be drawn that the cometary surface on meter scales has a reasonable lower limit of the tensile strength of the order of 1kPa whereas the probable upper limit can be taken as 100 kPa.

Now that the foundations of the regolith behavior have been laid out, in the next section we delve into the analysis of the soil interaction process during penetration.

7.3 Modeling of Forces acting on Penetrating Object

A complete and general solution describing the penetration of a projectile into a solid body is not known, though there are several published models available which may be applicable to the harpoon (see, e.g., those listed by Wang [35]). For current modeling efforts we consider the harpoon to be a rigid, conically tipped cylindrical projectile, where θ is the half opening angle of the cone [3]. Several possible forces may contribute to the overall deceleration experienced by the projectile during penetration [2]. These may depend on penetrated depth and velocity as well as target material parameters. Most of the forces can be expressed as the integral of decelerating stresses over the wetted surface S_w of the penetrator in contact with the target material. The main force terms of clear (or plausible) physical origin found in the published literature are as follows:

- A constant term associated with compressive strength, possibly including a contribution from the targets self-weight. The latter should be negligible on the comet, where the surface gravity g is expected to be no more than about 1/2000 of that on Earth. It may be more significant for ground-based experiments where the projectile is fired downwards into a cohesion-less target, though the fact that it is also proportional to the diameter of the projectile means that the term is still quite small for laboratory-scale experiments.

- A term which increases linearly with depth due to the weight per unit volume ρg of the overlying material (overburden pressure). As with the self-weight, this should be negligible on the small body but needs to be considered for ground-based experiments, especially those with cohesion-less targets. This term is also proportional to a factor $N_q(\phi)$. For the limit $\phi = 0$, $N_q = 1$ and the term becomes analogous to buoyancy in a fluid.

- A dynamic drag term proportional to the target density ρ and the square of velocity V, resulting from the transfer of momentum from the projectile to the target material. In many cases the importance of drag is incorporated by adopting a drag coefficient C_D (which may itself have a velocity dependence), analogous to the parameter used in fluid dynamics.

- Sliding friction between the projectile surface and the target material, governed by the coefficient of sliding friction μ_f and the total normal stress from the three terms above.

- A viscosity or damping term, proportional to the component of velocity parallel to the projectiles surface. As with friction, this force acts parallel to the harpoons surface rather than normal to it. The physical validity of this term seems to be a matter for debate.

- The weight of the projectile. This is only important when significant compared to the other (decelerating forces.

Collecting these terms together with the appropriate geometric factors, one obtains the following equation for the overall deceleration:

$$-\frac{dV}{dt} = \frac{1}{m}\int\int_{S_w}[(\frac{1}{2}C_D\rho V^2\sin^2\theta^{'} + \sigma + \rho g N_q z)\times(\sin\theta^{'} + \mu_f\cos\theta^{'}) + k_v V\cos^2\theta^{'}]dA - g \tag{31}$$

In this equation, $\theta^{'} = \theta$ along the conical tip, but $\theta^{'} = 0$ along the cylindrical shaht of the penetrating object. Also, from Komle [9], $N_q(\phi) = \exp(\pi\tan\phi)\tan^2(\frac{\pi}{4}+\frac{\phi}{2})$, and k_v is a constact with units of $[Nsm^{-3}]$, i.e., those of viscosity divided by the thickness of a representative boundary layer around the projectile where viscous flow occurs..

From [9], a parameter analogous to a drag coefficient can be defined in terms of the material parameters as

$$C_D = \frac{2}{(1-\eta)\cos^2\theta}\times[\frac{(1-\eta)+1/\alpha+\eta/(2-\alpha)}{\eta^{\alpha/2}} - \frac{1}{\alpha} - \frac{1}{2-\alpha}] \tag{32}$$

where $\alpha = 3\lambda/(3+2\lambda)$, $\lambda = \tan(\phi)$, ϕ is the angle of internal friction, $\eta = 1-\frac{\rho_0}{\rho}$ is the volumetric strain, ρ_0 is the bulk density of the target material before penetration. The case $\eta = 0$ implies zero compression.

After [9], the compressive stress and the drag term can be combined together, so that the radial pressure exerted on an area element of the target material in contact with an area element of the penetrators surface can be written as:

$$\sigma = [\eta^{-\alpha/2} - 1]\frac{\tau_0}{\lambda} + [\frac{(1-\eta)+1/\alpha+\eta/(2-\alpha)}{\eta^{\alpha/2}} - \frac{1}{\alpha} - \frac{1}{2-\alpha}]\frac{\rho_0 V^2\tan^2\theta}{(1-\eta)} \tag{33}$$

where τ_0 is the soil cohesion. Note that σ consists of a constant term and a term proportional to the square of velocity, i.e. this model produces neither a term analogous to viscosity nor an overburden pressure term.

The total decelerating force acting on the penetrator consists then of two components. One is the vertical component of the normal stress on the penetrators conical surface, the second being the vertical component of the sliding friction acting tangentially to the projectiles surface. Combining these two components and integrating over the whole wetted surface S_w of the penetrator gives the following expression for the deceleration of the harpoon:

$$-\frac{dV}{dt} = \frac{1}{m}\int\int_{S_w}[(\frac{1}{2}C_D\rho V^2\sin^2\theta^{'} + \sigma + \rho g N_q z)\times(\sin\theta^{'} + \mu_f\cos\theta^{'}) + k_v V\cos^2\theta^{'}]dA - g \tag{34}$$

To get insight into the sensitivity of the system to the various parameters involved, we derived a simple one-dimensional model of the system behavior during penetration. Assumptions used in the derivation of this reduced model are the following. The harpoon is modeled as a point-like body with variable mass and area. The mass of body increases because of soil compaction. The soil properties are constant. The gravity level is constant. The soil penetration is modeled following the previous section. The system equations are integrated with a 4-th order constant step Runge-Kutta integrator. Under these assumptions, the final equations of motion of the penetrating harpoon become:

$$v = \dot{h} \tag{35}$$

$$\dot{v} = g - \frac{A\sigma_c}{M} - \frac{\rho A C_D v^2}{2M} \tag{36}$$

$$\dot{m} = \rho A v \tag{37}$$

$$M = m_0 + m(t) \tag{38}$$

$$\sigma_c = s_c c N_c + \rho g(\frac{1}{2}s_g A N_g + s_q N_q h) \tag{39}$$

where ρ is the soil density, g is the local gravity level, m_0 is the initial mass of the harpoon, σ_c is the maximum soil compressive stress, N_c, N_g, N_q are soil bearing capacity factors, s_c, s_g, s_q are shape factors which depend on the penetrator cross-section shape, and c is the cohesion coefficient.

Figure 48(a), taken from [27], depicts the soil bearing stress factors used in the soil constitutive equation, and figure 48(b) shows the soil bearing stress vs. depth as a function of the soil friction coefficient. As expected, the penetration is less when the friction coefficient is high. Figure 49 depicts the soil bearing stress vs. depth as a function of (a) friction angle, and (b) gravity level. In these cases, the lower cohesion and lower gravity level would be representative of penetration into a powdery soil, while the higher cohesion levels represent the case of a more compact soil. Figure 50 depicts the soil bearing stress vs. depth as a function of (a) penetrator diameter , and (b) soil density. Figure 50 depicts the soil bearing stress vs. depth as a function of (a) penetrator mass , and (b) cone angle. The last two figures confirm the fact that a larger diameter anchor would penetrate less, and that a heavier anchor would penetrate deeper.

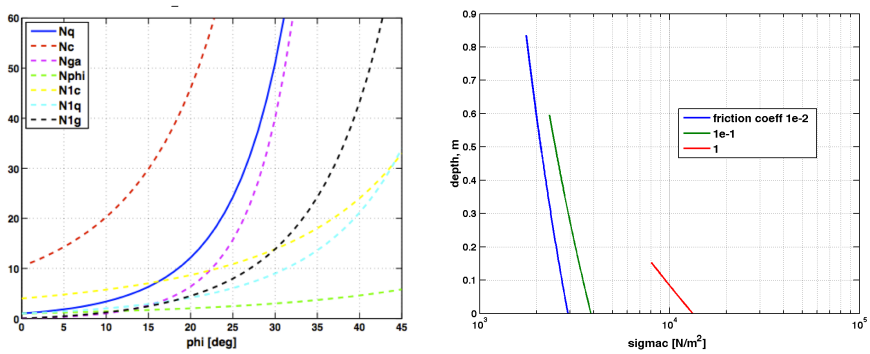

Figure 48: (a) Soil bearing stress factors, (b) Soil bearing stress vs. depth as a function of friction.

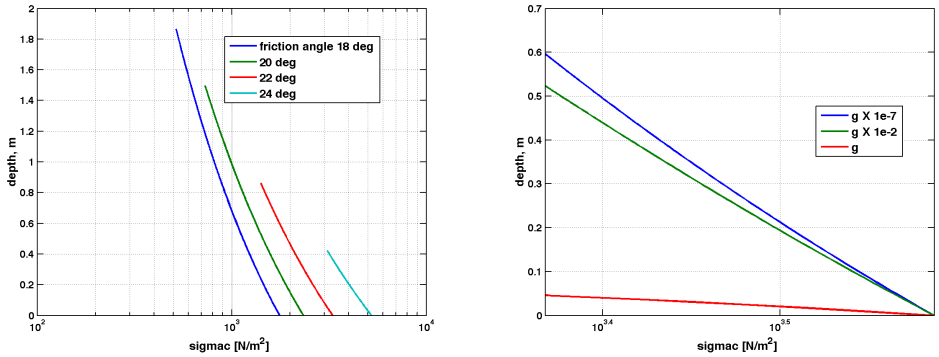

Figure 49: Soil bearing stress vs. depth as a function of (a) cohesion, and (b) gravity level.

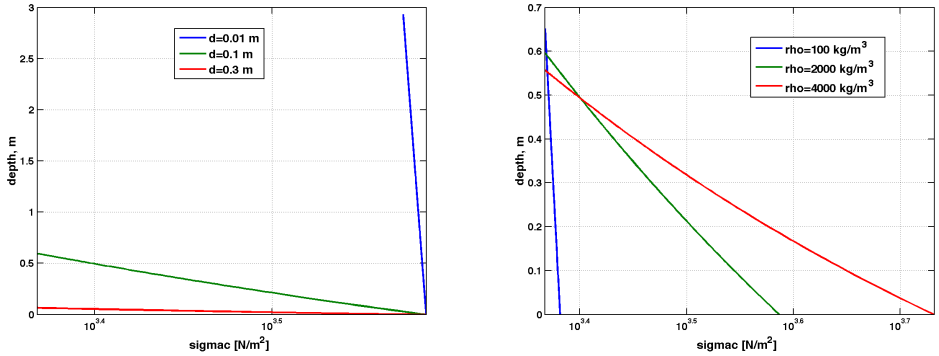

Figure 50: Soil bearing stress vs. depth as a function of (a) penetrator diameter , and (b) soil density.

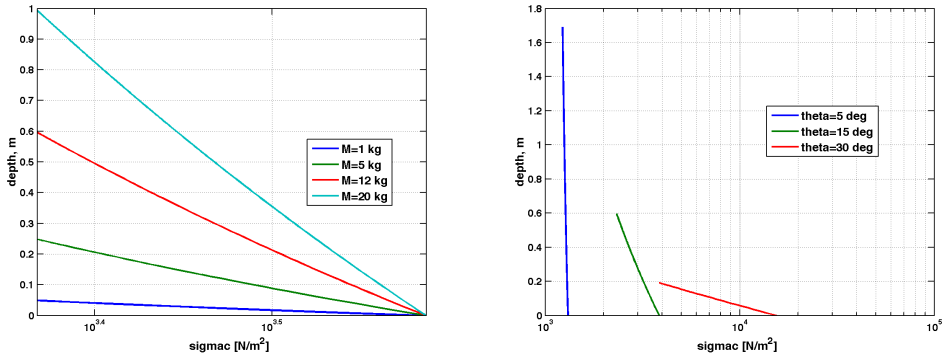

Figure 51: Soil bearing stress vs. depth as a function of (a) penetrator mass , and (b) cone angle.

8 Outreach Activities

8.1 Concept Art

We collaborated with Cornelius Dämmrich, a concept artist of the Museum of Science Fiction (MOSF), to produce concept art, as shown in Figures 52-53. Our work was featured on the MOSF webpage along with the concept arts[7].

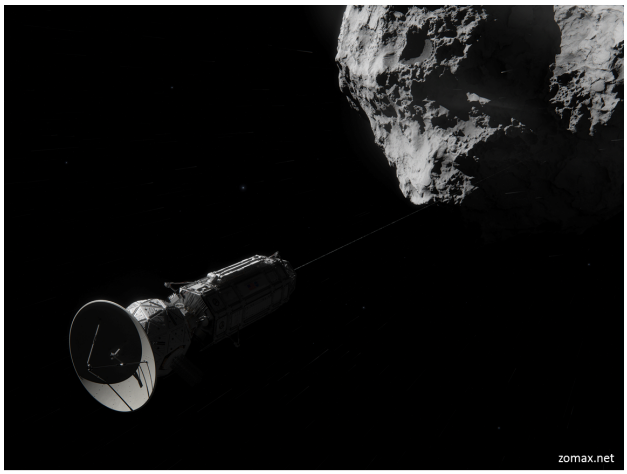

Figure 52: Concept drawing of a Comet Hitchhiker spacecraft, performing a hitchhiker maneuver at a small body in the outer Solar System.

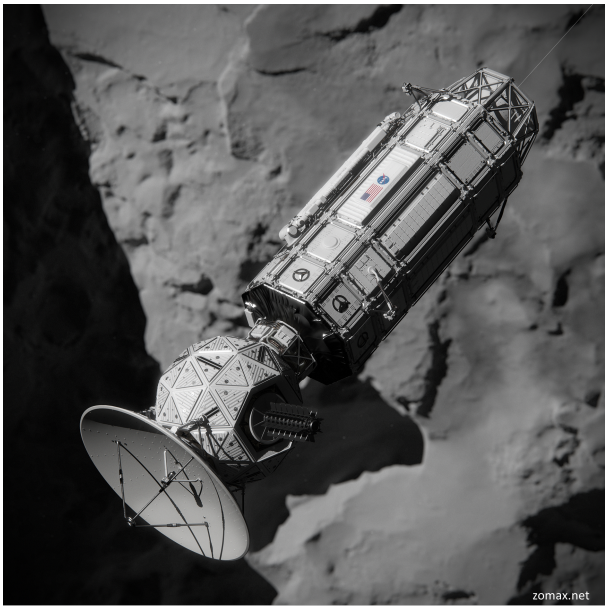

Figure 53: Close-up view of the hitchhiker spacecraft.

[7] http://www.museumofsciencefiction.org/jpl-hitchhiker/

8.2 Presentations to Professional Communities

- PI Ono gave a talk on Comet Hitchhiker in the Systems and Control Seminar Series of the Mechanical and Aerospace Engineering Department at UCLA on October 31, as shown in Figure 54.

Figure 54: PI Ono gave a talk at UCLA on Halloween Day in 2014

- PI Ono introduced the Comet Hitchhiker concept in the Keck Institute Space Studies (KISS) Workshop "Science and Enabling Technologies to Explore the Interstellar Medium," held at California Institute of Technology on September 8 11, 2014.
- The Comet Hitchhiker concept was covered by the Year in Review of the *AIAA Aerospace America* magazine (December 2014, pp75).
- We submitted an abstract to the 2015 AIAA SPACE conference.

8.3 Media Coverage

- Astroblogs, "Meeliften met een komeet" (Dutch), Jan 28, 2015.
  `http://www.astroblogs.nl/2015/01/28/meeliften-op-een-komeet/`
- Today's Lifestyle, "Spacecrafts Could One Day 'Hitch' Rides On Comets Into Deep Space."
  `http://m.todayslifestyle.com/videos/?spacecrafts-could-one-day-hitch-rides-on-comets-into-deep-spa`
- Motherboard, "NASA Wants to Tether Spacecraft to Comets to Hitch Free Rides to Deep Space," Jan 27, 2015
  `http://motherboard.vice.com/read/nasa-wants-to-tether-spacecraft-to-comets-to-hitch-free-rides-to-`
- Museum of Science Fiction Press Release, "Comet Hitchhiker Concept Unveiled at NASA Symposium", Jan 26, 2015.
  `http://static1.squarespace.com/static/52615e54e4b051d1915a8890/t/54c618d0e4b0a0456dc284c8/1422268624547/JPL+Hitchhiker+1-13-2015+Final.pdf`
- WebRonza, "Suisei ni Hitchhike" (Japanese), Oct 13, 2014.
  `http://webronza.asahi.com/science/themes/2914101100001.html`
- Recently contacted by a German production company, Pro TV Produktion GmbH, to cover Comet Hitchhiker in a TV show. Details TBD.

References

[1] V. P. Alekseevskii. Penetration of a rod into a target at high velocity. *Combustion, Explosion, and Shock Waves*, 2(2), 1969.

[2] W.A. Allen, E.B. Mayfield, and H.L. Morrison. Dynamics of a projectile penetrating sand. *J. Appl. Phys.*, 28, 1957.

[3] W.W. Anderson, T.J. Ahrens, A. Gibson, R. Scott, and K. Suzuki. Emplacement of penetrators into planetary surfaces. *J. Geophys. Res.*, 1996.

[4] Allison M. Beese, Xiaoding Wei, Sourangsu Sarkar, Rajaprakash Ramachandramoorthy, Michael R. Roenbeck, Alexander Moravsky, Matthew Ford, Fazel Yavari, Denis T. Keane, Raouf O. Loutfy, SonBinh T. Nguyen, and Horacio D. Espinosa. Key factors limiting carbon nanotube yarn strength: Exploring processing-structure-property relationships. *ACS Nano*, 8(11):11454–11466, 2014. PMID: 25353651.

[5] Garrett Birkhoff, Duncan P. MacDougall, Emerson M. Pugh, and Sir Geoffrey Taylor. Explosives with lined cavities. *Journal of Applied Physics*, 19(6), 1948.

[6] J. C. Castillo-Rogez and B. E. Schmidt. Geophysical evolution of the themis family parent body. *Geophysical Research Letters*, 67(10), 2010.

[7] B.G Demczyk, Y.M Wang, J Cumings, M Hetman, W Han, A Zettl, and R.O Ritchie. Direct mechanical measurement of the tensile strength and elastic modulus of multiwalled carbon nanotubes. *Materials Science and Engineering: A*, 334(12):173 – 178, 2002.

[8] Biele et al. The putative mechanical strength of comet surface material applied to landing on a comet. *Acta Astronautica*, 65, 2009.

[9] N.I. Komle et al. Impact penetrometry on a comet nucleus *n* interpretation of laboratory data using penetration models. *Planetary and Space Science*, 49, 2001.

[10] Yuan Gao, Amy M Marconnet, Rong Xiang, Shoichi Maruyama, and Kenneth E Goodson. Heat capacity, thermal conductivity, and interface resistance extraction for single-walled carbon nanotube films using frequency-domain thermoreflectance. *Components, Packaging and Manufacturing Technology, IEEE Transactions on*, 3(9):1524–1532, 2013.

[11] JM Greenberg, H Mizutani, and T Yamamoto. A new derivation of the tensile strength of cometary nuclei: application to comet shoemaker-levy 9. *Astronomy and Astrophysics*, 295:L35–L38, 1995.

[12] Walter Herrmann and James S. Wilbeck. Review of hypervelocity penetration theories. *International Journal of Impact Engineering*, 5(14):307 – 322, 1987. Hypervelocity Impact Proceedings of the 1986 Symposium.

[13] Sin iti Sirono and J.Mayo Greenberg. Do cometesimal collisions lead to bound rubble piles or to aggregates held together by gravity? *Icarus*, 145(1):230 – 238, 2000.

[14] David Jewitt. A first look at the damocloids. *Astronomical Journal*, 2005.

[15] David Jewitt. The active asteroids. *The Astronomical Journal*, 143, 2012.

[16] David Jewitt, Jessica Agarwal, Nuno Peixinho, Harold Weaver, Max Mutchler, Man-To Hui, Jing Li, and Stephen Larson. A new active asteroid 313p/gibbs. *The Astronomical Journal*, 149(2):81, 2015.

[17] Michiel Kruijff, Erik J. Van Der Heide, and Wubbo J. Ockels. Data analysis of a tethered spacemail experiment. 46(6), 2009.

[18] E Kührt and HU Keller. The formation of cometary surface crusts. *Icarus*, 109(1):121–132, 1994.

[19] W. E. Lamie. Case study: Nasa's deep impact employs embedded systems to score bullseye 80 million miles away. Military Embedded Systems, 2006. Retrieved Feb 18, 2014.

[20] Eugene M. Levin. *Dynamic Analysis of Space Tether Missions*. Univelt, 2007.

[21] Z. Lin. *Low gain feedback*. Springer, 1999.

[22] J. Marsden and T. Hughes. *Mathematical foundations of elasticity*. Dover publications, 1993.

[23] Andrea Milani, Alberto Cellino, Zoran Kneevi, Bojan Novakovi, Federica Spoto, and Paolo Paolicchi. Asteroid families classification: Exploiting very large datasets. *Icarus*, 239(0):46 – 73, 2014.

[24] A. López Ortega, M. Lombardini, D.I. Pullin, and D.I. Meiron. Numerical simulation of elastic-plastic solid mechanics using an eulerina stretch tensor approach and hlld riemann solver. *Journal of Computational Physics*, 257:414–441, 2014.

[25] J. Park and K. Lee. Carbon nanotube yarns. *Korean Journal of Chemical Engineering*, 2012.

[26] P. A. Penzo and H. L. Mayer. Tethers and asteroids for artificial gravity assist in the solar system. In*AIAA/AAS Astrodynamics Conference*, 1984.

[27] M. Quadrelli, H. Mazhar, and D. Negrut. Modeling and simulation of harpooning processes for small body exploration. In *Proc. of AIAA SPACE*.

[28] C. G. Sauer. Midas - mission design and analysis software for the optimization of ballistic interplanetary trajectories. *Journal of the Astronautical Sciences*, 1989.

[29] Stelzner and Nasif. Harpooning technology for in-situ exploration of small bodies. *IEEE paper*, 2000.

[30] A. Tate. A theory for the deceleration of long rods after impact. *Journal of the Mechanics and Physics of Solids*, 15(6):387 – 399, 1967.

[31] A. Tate. Further results in the theory of long rod penetration. *Journal of the Mechanics and Physics of Solids*, 17(3):141 – 150, 1969.

[32] Toyobo Co., Ltd. Technical information of pbo fiber zylon, 2001.

[33] Josep M Trigo-Rodríguez and Jordi Llorca. The strength of cometary meteoroids: clues to the structure and evolution of comets. *Monthly Notices of the Royal Astronomical Society*, 372(2):655–660, 2006.

[34] Y. Tsuda, O. Mori, R. Funase, H. Sawada, T. Yamamoto, T. Saiki, T. Endo, and J. Kawaguchi. Flight status of {IKAROS} deep space solar sail demonstrator. *Acta Astronautica*, 69(910):833 – 840, 2011.

[35] Wen L Wang. Low velocity projectile penetration. *Journal of the Soil Mechanics and Foundations Division*, 97(12):1635–1655, 1971.

[36] Xianlong Wei, Ming-Sheng Wang, Yoshio Bando, and Dmitri Golberg. Thermal stability of carbon nanotubes probed by anchored tungsten nanoparticles. *Science and Technology of Advanced Materials*, 12(4):044605, 2011.

[37] G.W. Wetherill and D.O. Revelle. Relationships between comets, large meteors, and meteorites. *Comets*, 1982.

[38] Rufan Zhang, Yingying Zhang, Qiang Zhang, Huanhuan Xie, Weizhong Qian, and Fei Wei. Growth of half-meter long carbon nanotubes based on schulzflory distribution. *ACS Nano*, 7(7):6156–6161, 2013. PMID: 23806050.

[39] Haibo Zhao, Yingying Zhang, Philip D Bradford, Qian Zhou, Quanxi Jia, Fuh-Gwo Yuan, and Yuntian Zhu. Carbon nanotube yarn strain sensors. *Nanotechnology*, 2010.